Site NGHP-01-05

By T. Collett, M. Riedel, J. Cochran, R. Boswell, J. Presley, P. Kumar, A. Sathe, A. Sethi, M. Lall, and the National Gas Hydrate Program Expedition 01 Scientists

Scientific Investigations Report 2012–5054

U.S. Department of the Interior
U.S. Geological Survey

Contents

Figures

Tables

Site NGHP-01-05

By T. Collett, M. Riedel, J. Cochran, R. Boswell, J. Presley, P. Kumar, A. Sathe, A. Sethi, M. Lall, and the National Gas Hydrate Program Expedition 01 Scientists

Background and Objectives

Site NGHP-01-05 (Prospectus Site KGGH02-A) is located at 16° 01.722' N, 82° 02.677' E in the Krishna-Godavari (KG) Basin (fig. 1). The water depth is ~ 945 m (average of all holes).

The objectives of the work carried out at this site follow the general objectives of NGHP Expedition 01:

- Study the occurrence of gas hydrate and establish the background geochemical, geological, geophysical and microbiological baselines for gas-hydrate proxy studies;
- Define the relationship between the sedimentology and structure of the sediments and the occurrence and concentration of gas hydrate;
- Calibrate remote sensing data such as seismic data by acquiring LWD/MWD and wire-line log data as well as VSP data for time-depth matching.

The seismic data (line AD-94-33, oriented NW-SE) show a distinct BSR, which is cutting inclined, parallel beds (figs. 2 and 3). The BSR is estimated at a depth of 125 mbsf (0.158 s TWT) using a constant velocity of 1,580 m/s for the entire sediment column. The BSR first appears near shot point 220 and extends towards shot point 380 to the SE. The seismic line shows a sedimentary section dominated by slope processes. The seafloor is relatively flat and forms a terrace around this site with a slope of less than 0.5º. However, the seismic section about 2.0 to 5.0 km to the northwest shows evidence of past slope failures and possible faulting. The site was approved to a well depth of only 200 mbsf due to the presence of bright reflectivity beneath the BSR indicating the likely presence of free gas below that depth (figs. 2 and 3). The originally proposed well site KGGH02 was moved by ~300 m upslope towards the northwest to avoid reflectors with the highest reflectivity around this site. Beneath Site KGGH02-A the average amplitude of the reflectors is about half of what it is beneath Site KGGH02.

Operations

This operations summary covers the second Chennai port call, transits to Site NGHP-01-05 (KGGH02-A), and drilling/coring operations for Holes NGHP-01-05A through NGHP-01-05E (fig. 4). Schedule details and statistics for this site can be found as Appendixes:

- Appendix 1: NGHP Expedition 01 Operations Schedules
- Appendix 2: NGHP Expedition 01 Operations Statistics

Included in the Glossary is a list of standard or commonly used operations terms and acronyms.

Hole NGHP-01-05A

The first hole of Site NGHP-01-05 was drilled on Leg 2 of NGHP Expedition 01 as the fifth hole in a twelve-hole LWD/MWD transect. The 5 NMI transit from Site NGHP-01-04 (KGGH01-A) was completed in 1.0 hr, the vessel was switched from cruise mode to DP control, and a positioning beacon was deployed at the prospectus coordinates at 1633 hr on May 24, 2006. Prior to deploying the LWD/MWD tools a data upload task was completed and the SonicVISION tool required some troubleshooting. With all tools functional and deck tested, the nuclear source was loaded and the drill string was lowered to a depth of 114.8 mbrf. A second function test was performed at that depth before continuing the pipe trip to the seafloor. The drill string was spaced out for spudding and a tag of the seafloor indicated a mudline depth of 963.0 mbrf. After offsetting the vessel 2 m north of the prospectus coordinates, Hole NGHP-01-05A was spudded at 2205 hr on May 24. LWD/MWD drilling continued at a controlled rate of 18.3 m/h (average net ROP including connection time) to a total depth of 200.0 mbsf. The hole was displaced with 56.6 barrels of weighted 10.5 ppg Sepiolite mud. After recovering the drill string, the BHA was racked back in the derrick, the LWD/MWD source was removed, the data were downloaded, and appropriate tools/batteries were changed out. The vessel was switched from DP to cruise control and got underway for Site NGHP-01-06 (KGGH04-A) at 1715 hr on May 25, 2006.

Hole NGHP-01-05B

Site NGHP-01-05 was reoccupied at the end of the LWD/MWD transect to drill a second LWD/MWD hole, this time using the Schlumberger ProVISION NMR tool, picked up via a rendezvous with the supply boat “Zeenne” on June 1, 2006.

The 3.8 NMI transit from Site NGHP-01-11 (GDGH12-A) was completed in 4.00 hr. The move was made in DP mode with the drill string suspended below the ship and knobby joints

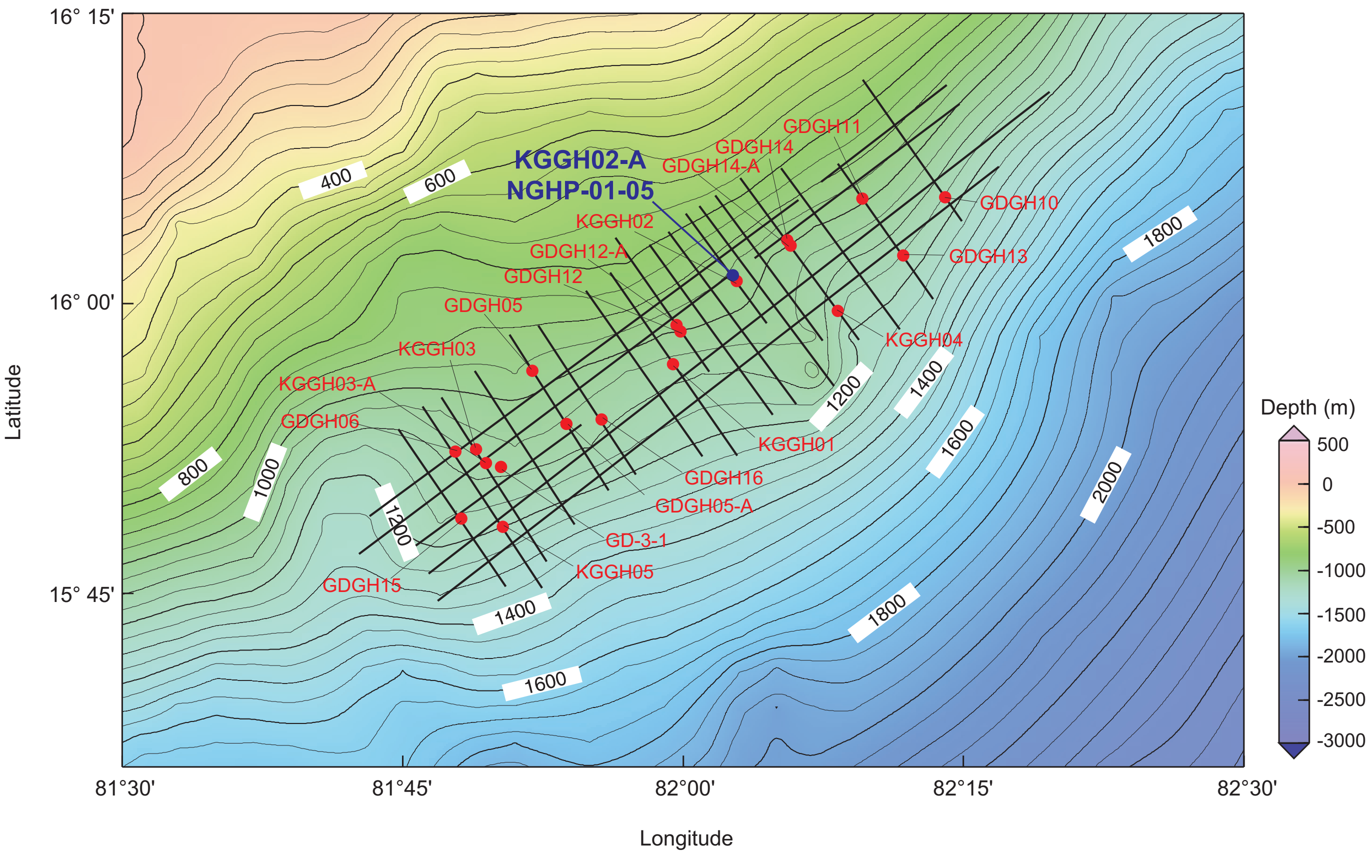

Figure 1. Location of Site NGHP-01-05 (Prospectus Site KGGH02-A) in the Krishna-Godavari (KG) Basin.

installed through the guide horn. Once on location at 1745 hr on June 4, 2006, the knobby joints were laid out, a positioning beacon was deployed, and the drill string with LWD/MWD BHA was deployed. The seafloor was tagged yielding a seafloor depth of 952.0 mbrf. The ship was offset 2 m to the north of Hole NGHP-01-05A and Hole NGHP-01-05B was spudded at 1915 hr on June 4.

LWD/MWD drilling continued for 9.5 hours at a controlled rate of 27.6 m/h (average net ROP including connection time) to a total depth of 200.0 mbsf and the hole was displaced with 56 barrels of weighted 10.5 ppg Sepiolite mud. After recovering the drill string, the BHA was racked back in the derrick, the LWD/MWD source was removed, and the data were downloaded. All tools were cleaned and laid out to the main deck in preparation for offloading. Prior to getting underway, a control length drill collar was laid out and a seal bore drill collar was picked up in its place in preparation for future APC/XCB coring. The vessel was switched from DP to cruise control and got underway for Chennai at 1115 hr on June 5, 2006.

Hole NGHP-01-05C

Leg 3A of the five-leg NGHP Expedition 01 began after completing a 2.8 day port call in Chennai. This was the second Chennai port call and was primarily used for changing out the science compliment, loading special Fugro and GeoTek equipment, and taking on general supplies. The vessel departed Chennai with the last line away from East Quay (coal dock) at 1745 hr on June 9, 2006. The 203 NMI transit was made to Site NGHP-01-05 (KGGH02-A) at an average speed of 9.8 knots.

The vessel was switched from cruise mode to DP control at 1430 hr on June 10, 2006, and a positioning beacon was deployed at the Hole NGHP-01-05A location coordinates. The ice bath was installed in the moon pool and a standard two-stand APC/XCB BHA was made up with a LFV and a typical 11-7/16 in APC/XCB C-3 TCI roller cone bit.

Hole NGHP-01-05C was to focus on continuous APC/XCB coring with a few select pressure cores within the gas-hydrate stability field. Temperature measurements were also to be taken using the APCT–3, APCT, and DVTP systems to define a thermal gradient from seafloor to total depth.

The vessel was offset 10 m to the SW of Hole NGHP-01-05A while the drill string was tripped to bottom. The bit was positioned at a depth of 955.0 mbrf and Hole NGHP-01-05C was spudded at 1915 hr on June 10, establishing a seafloor depth of 957.2 mbrf. The PDR depth for this site, corrected to the rig floor DES, was 962.4 mbrf. APC Core NGHP-01-05C-01H was on-deck at 1930 hr and APC coring continued through Core NGHP-01-05C-09H to a depth of 78.3 mbsf.

Temperature measurements were taken using the APCT–3 shoe on Cores NGHP-01-05C-03H and NGHP-01-05C-06H (21.3 and 49.8 mbsf respectively), and the APCT

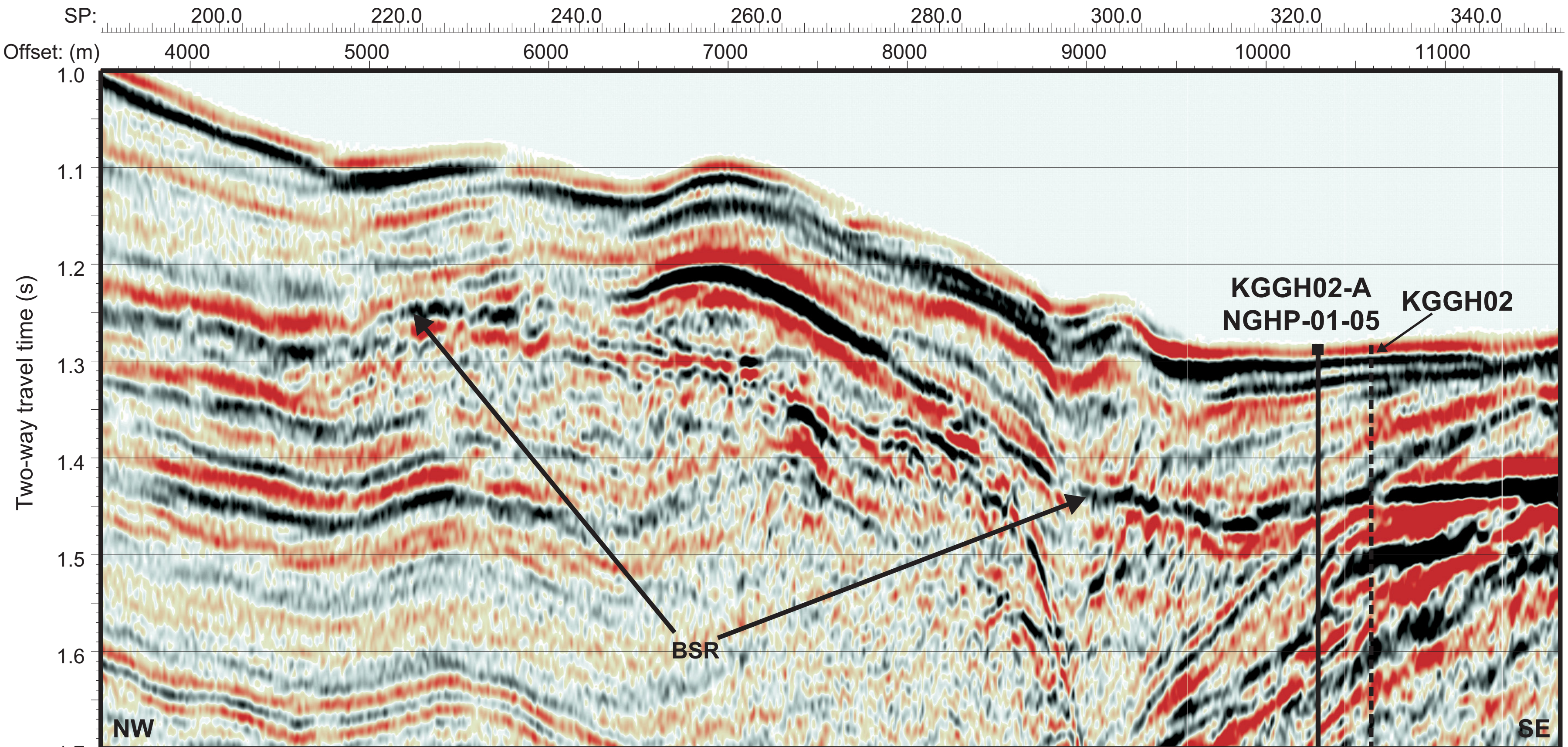

Figure 2. Seismic line AD-94-33 (oriented NW-SE) intersecting with Site NGHP-01-05 (Prospectus Site KGGH02-A).

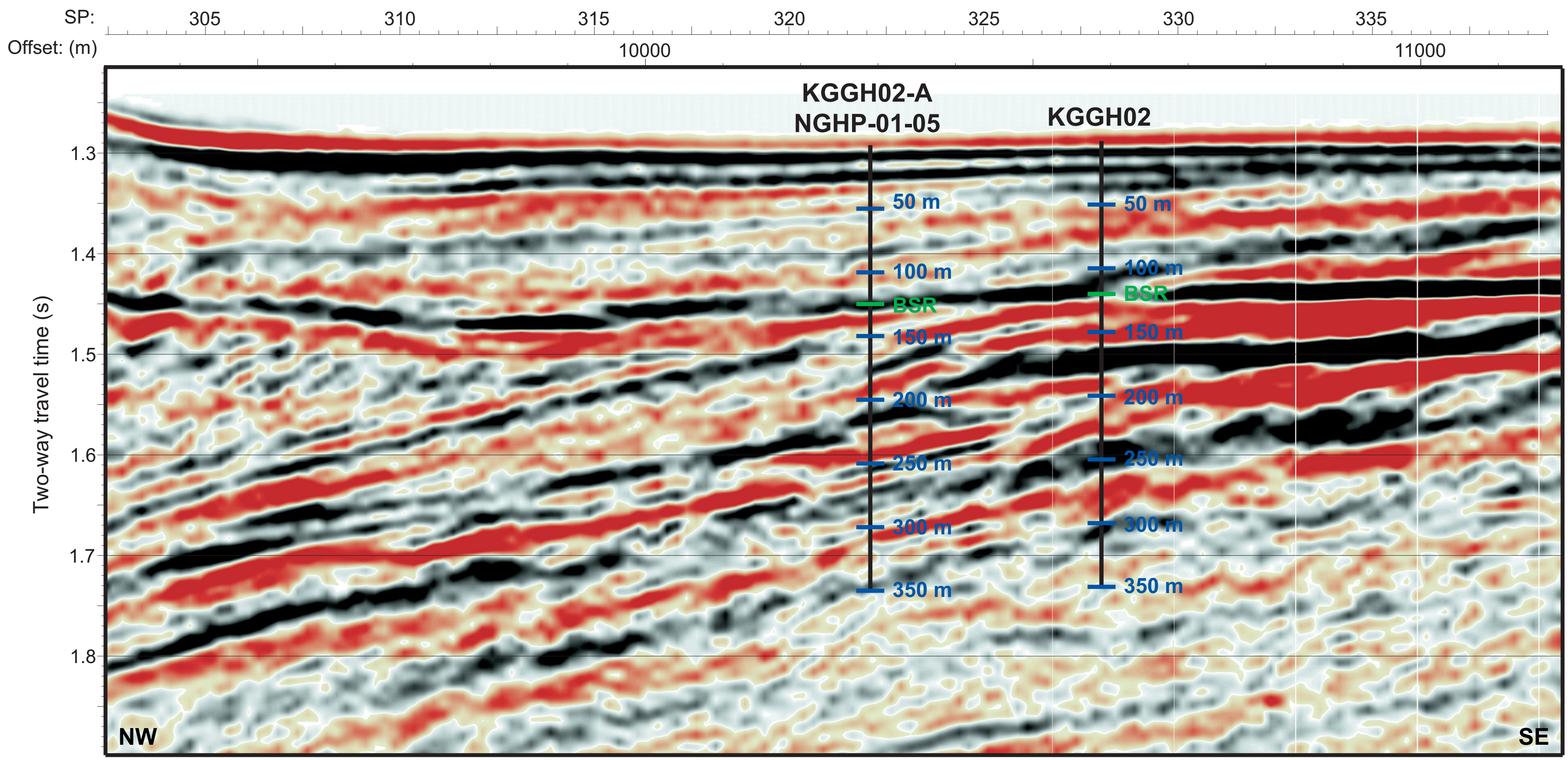

Figure 3. Section of seismic line AD-94-33 around Site NGHP-01-05 (Prospectus Site KGGH02-A) showing estimated depth of formation depth and BSR using a uniform velocity of 1,580 m/s for the entire sediment column.

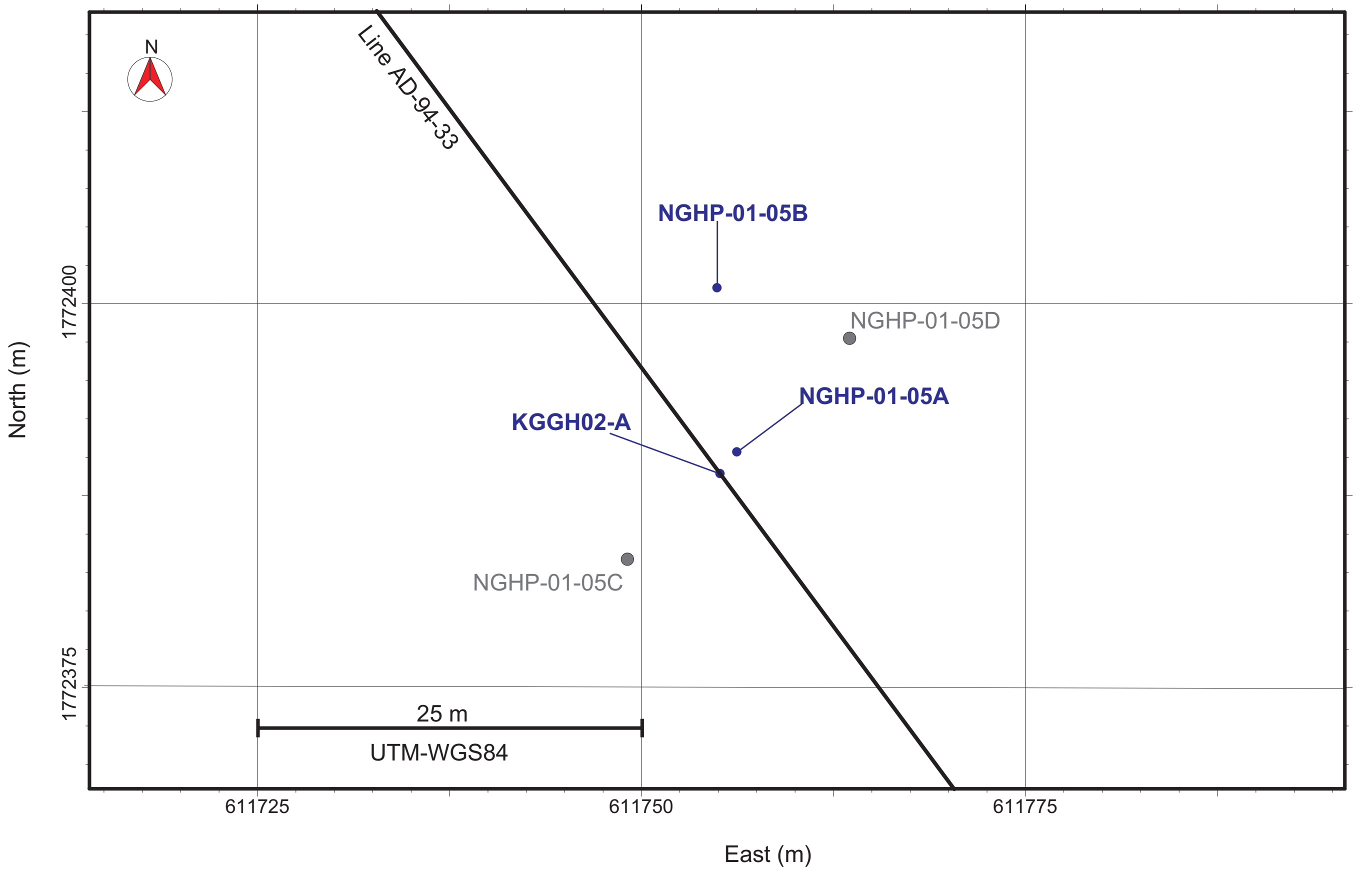

Figure 4. Map showing all holes occupied at Site NGHP-01-05 (KGGH02-A).

shoe on Core NGHP-01-05C-04H (30.8 mbsf). The APC methane tool (APCM) was deployed for Cores NGHP-01-05C-03H through NGHP-01-05C-06H; however, the tool was damaged on Run 6 and all data were lost.

A 10-barrel Sepiolite mud sweep was circulated and the first PCS Core NGHP-01-05C-10P for this hole was recovered from 79.3 mbsf. An XCB Core NGHP-01-05C-11X set up the second PCS Core NGHP-01-05C-12P recovered from 87.0 mbsf. Both PCS deployments included successful recovery of data with the PCS methane tool. Three XCB cores, NGHP-01-05C-13X through NGHP-01-05C-15X, were recovered to 115.8 mbsf and a DVTP temperature measurement was successfully taken at that depth. Nine additional XCB cores, NGHP-01-05C-16X through NGHP-01-05C-24X, were recovered to a depth of 200.0 mbsf where a final DVTP temperature measurement was successfully taken. Rates of penetration with the XCB varied between 8.2 and 19.2 m/h and recovery ranged from 15 percent to 85 percent. The hole was displaced with 79 barrels of 10.5 ppg weighted mud and the drill string was pulled out of the hole with the top drive. Hole NGHP-01-05C officially ended when the bit cleared the seafloor at 0500 hr on 12 June.

Whirlpaks (microbeads) commonly used for microbiological contamination control were not used for coring. Accelerated core barrel handling protocols were used for all core barrels (APC, XCB, and PCS) deployed in this hole. All APC/XCB core barrels were laid down immediately upon arrival at the rig floor before making another drill pipe connection or deploying the next core barrel. Once at the rig floor any PCS core barrel showing signs of proper actuation was placed in the moon pool ice bath.

Hole NGHP-01-05D

Hole NGHP-01-05D was intended primarily for deployment of specialty pressure-coring systems targeted to sample areas of high gas-hydrate interest. Limited APC coring was to be conducted through the SMI. Wire-line logging was scheduled after drilling/coring the hole to TD.

The vessel was offset 10 m to the NE of Hole NGHP-01-05A and the bit was positioned at a depth of 953.0 mbrf. Hole NGHP-01-05D was spudded at 0530 hr on June 12, 2006, establishing a seafloor depth of 955.1 mbrf (943.7 mbsf). APC coring continued through Core NGHP-01-05D-04H to a depth of 35.9 mbsf. Two deployments of the APCT were done on Cores NGHP-01-05D-03H and -04H.

The hole was drilled an additional 7.0 m to a depth of 44.9 mbsf where a sequence of pressure cores commenced.

A total of eight pressure cores (each approximately one-meter advance) were cut using the PCS, FPC, and HRC pressure coring systems. Each pressure core was preceded by a drilled or washed interval and the hole was swept with a 10–15 bbl Sepiolite mud pill prior to each deployment. PCS

Core NGHP-01-05D-05P advanced from 44.9 to 45.9 mbsf followed by a drilled interval of 31.0 m. PCS Core NGHP-01-05D-06P advanced from 76.9 to 77.9 mbsf followed by a drilled interval of 7.0 m. FPC Core NGHP-01-05D-07Y advanced from 84.9 to 85.9 mbsf followed by a drilled interval of 3.0 m. HRC Core NGHP-01-05D-08E advanced from 88.9 to 89.9 mbsf followed by another drilled interval of 3.0 m. PCS Core NGHP-01-05D-09P advanced from 92.9 to 93.9 mbsf followed by a drilled interval of 21.0 m. HRC Core NGHP-01-05D-10E advanced from 114.9 to 115.9 mbsf followed by a drilled interval of 9.0 m. FPC Core NGHP-01-05D-11Y advanced from 124.9 to 125.9 mbsf followed by a drilled interval of 74.1 m. PCS Core NGHP-01-05D-12P advanced from 200.0 mbsf to a total depth for the hole of 201.0 mbsf.

For all HYACINTH pressure-coring systems (FPC and HRC) a 15–20 minute wait period was employed at the mudline on the way in the hole and again during retrieval. This was to cool the core barrels down thus aiding in keeping any entrained gas hydrate within the stability field. At the rig floor all pressure-core barrels (PCS, FPC, and HRC) showing signs of proper actuation were placed in the moon pool ice bath prior to processing.

Two hours were spent conducting a wiper trip to ~60 mbsf and back and another four hours were spent in hole conditioning, reaming, and circulating mud sweeps to prepare the hole for wire-line logging. A go-devil was pumped to lock the LFV in the open position and the hole was displaced with 78 barrels of 10.5 ppg Sepiolite mud. The drill string was then tripped, setting the EOP at 67.5 mbsf.

At 1800 hr on June 13, 2006, the logging tool pallet was moved forward from the helideck and rig-up for logging began. The first logging run was made with the Triple Combo tool suite. Tools went in at 2050 hr and reached only 127.9 mbsf. This limited amount of hole was logged; however, due to the existing hole conditions a decision was made to drill a dedicated logging hole. The triple combo tools were recovered and the logging sheaves were rigged down by 0200 hr on June 14, 2006. The drill string was pulled clear of the seafloor at 0230 hr on June 14 ending Hole NGHP-01-05D.

Hole NGHP-01-05E

The vessel was offset 10 m to the northwest of Hole NGHP-01-05A for the drilling of a dedicated wire-line logging hole. Hole NGHP-01-05E was spudded at 0330 hr on June 14, 2006, establishing a seafloor depth of 955.1 mbrf. The hole was drilled to a depth of 200.0 mbsf in 9.0 hr (net ROP including connections of ~22 m/h). A 25-barrel Sepiolite mud sweep was circulated at TD to flush any remnant cuttings from the hole. The XCB center bit was recovered, a logging go-devil was deployed, and the hole was displaced with 78 barrels of 10.5 ppg Sepiolite mud for logging. The drill string was pulled out of the hole with the top drive to a depth of 140.0 mbsf where 10–15K pounds overpull was noted. While attempting to rack back the top drive 20K pounds of downward drag was noted at 125.3 mbsf. The pipe trip continued with the top drive installed and the pipe eventually came free at a depth of 86.7 mbsf. The maximum overpull employed during the trip was 20K pounds. Another 1.5 hr were required to wash/ream the hole back to TD where another 25 barrel Sepiolite mud sweep was circulated and the hole was displaced for the second time with 78 barrels of 10.5 ppg mud. The drill string was tripped once again and the EOP was placed at 67.5 mbsf by 1830 hr on June 14.

The Schlumberger logging sheaves were rigged up and the first logging run, made up of the Sonic (DSI) tool and Gamma Ray, was deployed downhole at 1950 hr. Run Number 1 was successfully deployed to TD at 200.0 mbsf and the tools were back out by 2400 hr. The second logging run was made with the Triple Combo tool string. This tool string was deployed at 0125 hr on 15 June and also reached TD. The Triple Combo string was recovered by 0830 hr and the FMS-Sonic tool string was made up. The third logging run was initiated at 0545 hr and reached a logging depth of 198.0 mbsf or just 2.0 m off bottom. The third tool suite was out at 0830 hr. The fourth logging run was dedicated to zero offset VSP measurements. The IODP mammal watch (daylight operations only) protocols were followed. VSP tools were deployed at 0915 hr and reached a depth of 197.0 mbsf. Shot points for the VSP were spaced ~5 m apart and the fourth suite of tools was recovered by 1600 hr. Logging operations were completed at 1630 hr after rigging down the logging sheaves. The top of the hole was displaced with 20 bbl of 10.5 ppg mud and the drill string was pulled clear of the seafloor at 1715 hr. The pipe trip continued to the surface where the BHA was racked back in the derrick, latch subs were inspected, and the bit cleared the rotary table at 1930 hr. The beacon was recovered during the pipe trip and thrusters/hydrophones were pulled in preparation for the transit. Hole NGHP-01-05E and Site NGHP-01-05 were ended as the vessel switched from DP to cruise mode at 2000 hr on June 15, 2006, and got underway for Site NGHP-01-10.

Lithostratigraphy

Site NGHP-01-05 is located in the KG Basin, along the eastern continental margin of India. At Site NGHP-01-05, a total of five holes (NGHP-01-05A through NGHP-01-05E) were drilled; two were cored (NGHP-01-05C and NGHP-01-05D). Hole NGHP-01-05C was cored to 200.0 mbsf and Hole NGHP-01-05D was cored to 201.0 mbsf. Holes NGHP-01-05A and NGHP-01-05B were drilled for LWD (logging-while-drilling) and Hole NGHP-01-05E was drilled for wire-line and VSP (vertical seismic profiling) logging (see “Operations ”).

We classify the sedimentary sequence recovered at Sites NGHP-01-05C and NGHP-01-05D as a single lithostratigraphic unit (that is, Lithostratigraphic Unit I) based on sedimentological criteria such as variations in sedimentary structure and grain size or biogenic and lithologic components (figs. 5, 6 and Site NGHP-01-05 Visual Core Descriptions in the supplemental data files). We also compare and correlate our results with the physical property measurements (magnetic susceptibility and gamma ray attenuation density) to better understand sedimentation characteristics at Site NGHP-01-05 and define the stratigraphic sequence (figs. 5, 6 and Site NGHP-01-05 Visual Core Descriptions).

At Site NGHP-01-05, we observed cyclicity in the RGB color scans of the cores and, similar to other KG Basin sites, a lack of *Discoaster* spp. in the record. Both of these observations suggest that the age of the stratigraphy is Quaternary. Additional postcruise biostratigraphy, however, may help further constrain the history of deposition throughout the entire KG Basin.

Lithostratigraphic Units

Lithostratigraphic Unit I

Intervals: Hole NGHP-01-05C, Sections NGHP-01-05C-01H-1 to TD; Hole NGHP-01-05D, Sections NGHP-01-05D-01H-1 to NGHP-01-05D-12P-1.

Depth: Hole NGHP-01-05C, 0-200 mbsf; Hole NGHP-01-05D, 0-201 mbsf.

Age: Quaternary

Core recovery was good at this site for the upper 80 mbsf; below that, cores recovered from apparent gas-hydrate-bearing sediments (see “Downhole Logging” for additional wire-line and LWD information) resulted in significantly less recovery (figs. 5 and 6). Correlation of Lithostratigraphic Unit I in Holes NGHP-01-05C and NGHP-01-05D was possible using the sediment characteristics and physical property data. Lithostratigraphic Unit I is composed of nannofossil-bearing-to-rich clay that ranges in color from shades of very dark greenish gray (10GY 3/1) to very dark gray (5Y 3/1) to black (N 2.5). The darker colored clays consistently contain terrigenous organic matter, which is visible in smear slides (tables 1 and 2) and often contain a smaller percentage of nannofossils than the lighter colored clay zones. Abundant, thin (0.2–3.0 cm) silt laminae and beds are distributed throughout the section in discrete zones (5–20 m thick; figs. 5, 6, and 7; tables 3 and 4). Mollusk shells (primarily bivalves, but also rare gastropods) and visible foraminifera tests generally occur in intervals with a higher percentage of silt-sized grains.

Throughout Site NGHP-01-05, authigenic carbonates are common below 25 mbsf to TD and occur as both small (1–3 cm) nodules and thin (2–3 cm) fine-grained horizontal bands (figs. 5, 6, and 8). Several zones (most prevalent in Cores NGHP-01-05C-07 and -08) consist of thin (1–3 cm) alternating bands of light and dark clay, silts, and authigenic carbonates (fig. 9). Bioturbated zones occur throughout the unit, but are usually best observed when highlighted by iron sulfide precipitates (figs. 5, 6 and Site NGHP-01-05 Visual Core Descriptions in the supplemental data files). Magnetic iron sulfides (likely gregite and(or) pyrrhotite) have been observed in gas-hydrate-bearing sediments offshore western North America (Musgrave and others, 2006) and may be responsible for some of the magnetic susceptibility highs observed here at Site NGHP-01-05. Magnetic susceptibility is also high in stratigraphic packages containing abundant sand and silt beds, which often contain magnetite grains (opaque minerals in smear slide; for example, Trehu and others, 2003). At Site NGHP-01-05, many of the susceptibility highs are associated with zones rich in silt laminae; however, the highest zones (between 0–27 mbsf) appear to coincide with the abundance of iron sulfides and observed bioturbation (figs. 5 and 6).

Smear slide analyses indicate that Lithostratigraphic Unit I is primarily composed (as a major lithology) of sediment with a predominance of clay sized (80–100 percent) grains with minor amounts of silt (up to 20 percent) and generally no sand (table 1). Minor lithologies described in smear slides included silt beds and the authigenic carbonate rich zones. The major non-biogenic components of Lithostratigraphic Unit I are feldspar, quartz, and clay and opaque minerals. Opaque grains, mostly sulfides in irregular and framboidal forms, are common in all grain sizes, and typically comprise trace amounts of the total sediment. The total biogenic component of the sediment is dominated by calcareous nannofossils, which comprise 5–50 percent of the total (biogenic and non-biogenic) sediment grains. Foraminifera are also common in the coarse fractions (>63 mm) of the sediments. Terrestrial organic matter was also observed in trace amounts throughout Lithostratigraphic Unit I.

Sedimentation Cycles

Cyclicity is noticeable in many sedimentary parameters at Site NGHP-01-05, including red-green-blue (RGB) values of the DIS core images (a measure of sediment color; fig. 10) and in the down-core distribution of silt lamina and beds (an indicator of slope failure and(or) proximity of the river mouth, that is, Krishna and Godavari rivers; figs. 5 and 6; tables 3 and 4). Assuming that the down-core distribution of silt laminae and beds is controlled by sea level cycles that favor increased delivery of coarse sediment to the slope during lowstands, the cyclic presence of silt-rich intervals to the bottom of Holes NGHP-01-05C and NGHP-01-05D may suggest that the sediments drilled are younger than mid-Pleistocene (~1.25 Ma), when ice sheet-driven 100-ky sea level cycles started to be prominent (Berger and Jansen, 1994; Giosan and others, 2002). Average sedimentation rates at these sites are therefore on the order of 15 cm/ky or higher. Magnetic susceptibility does not show a clear cyclicity (fig. 5) suggesting that it might be the combined result of primary influences (sediment mineralogy) and secondary overprints (diagenesis) as described above. Color cycles show subtle lithological changes expressed in either R, G, or B (fig. 10) that have a higher frequency than the silt lamina and beds. These high frequency color cycles may be driven by either precession (21 ky) or obliquity (40 ky), which may have modulated monsoon-fed sediment delivery from the Krishna and Godavari Rivers during the Quaternary. Postcruise age constraint from biostratigraphy will confirm if these sedimentological indicators are indeed a result of Quaternary depositional processes.

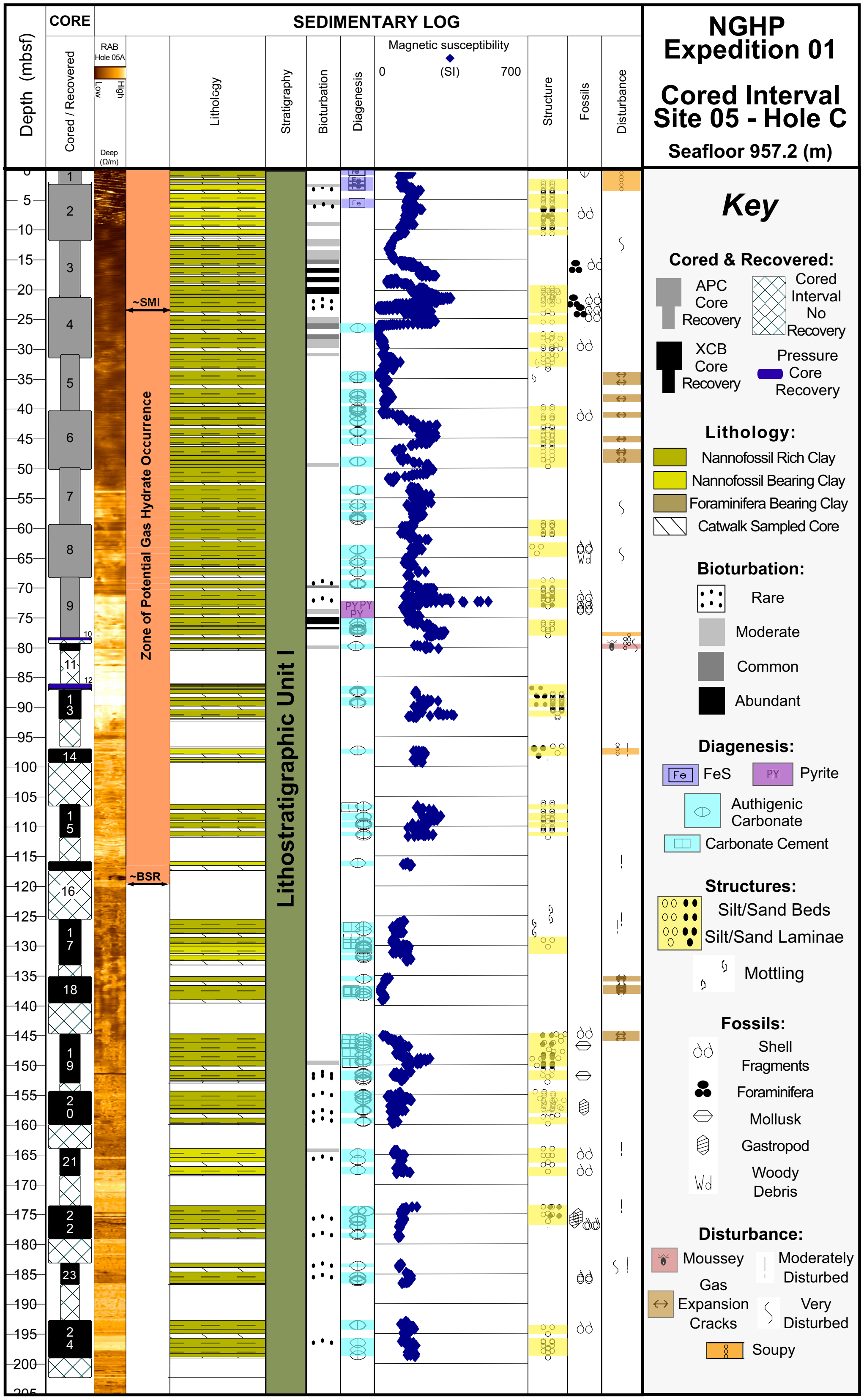

Figure 5. Lithostratigraphic summary of Hole NGHP-01-05C. [BSR, bottom-simulating reflector; SMI, sulfate-methane interface] Note: Colored intervals exceed symbol size when there is a range in the occurrence. Center point of each symbol represents depth of occurrence; therefore colored bars may slightly exceed core recovery; see Site NGHP-01-05 Visual Core Descriptions for the expanded scale, detailed core descriptions; see Site NGHP-01-05 Oversized Figures for the enlarged version of this summary.

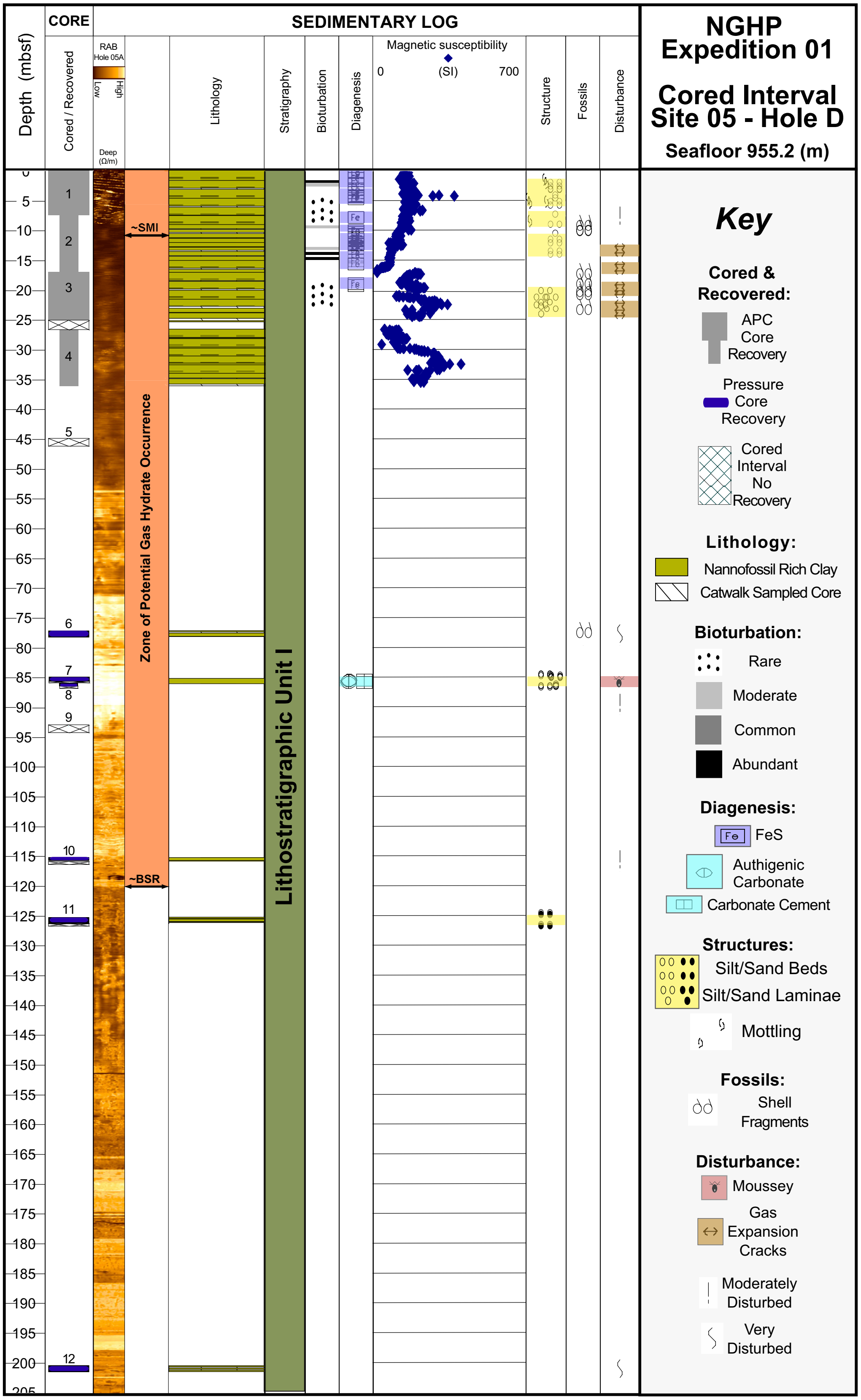

Figure 6. Lithostratigraphic summary of Hole NGHP-01-05D. [BSR, bottom-simulating reflector; SMI, sulfate-methane interface] Note: Colored intervals exceed symbol size when there is a range in the occurrence. Center point of each symbol represents depth of occurrence; therefore colored bars may slightly exceed core recovery; see Site NGHP-01-05 Visual Core Descriptions for the expanded scale, detailed core descriptions; see Site NGHP-01-05 Oversized Figures for the enlarged version of this summary.

Table 1. Smear slide data for Hole NGHP-01-05C.

Sample reference		Texture			Mineral								
Core, section, depth (cm, in section)	Lithology	Sand	Silt	Clay	Quartz	Feldspar	Mica	Heavy minerals	Clay minerals	Volcanic glass	Glauco-nite	Iron sulfides	Authigenic carbonates
NGHP-01-05C													
1H-1,40	D			100					60				
1H-2,14	D			100					58				
2H-3,60	D			100				5	84				
2H-1,73	M		100		60			30					
3H-2,70.5	D			100					42				
3H-4,37	D			100					42				
3H-6,121.5	D			100					49				
4H-6,50	D			100	10			2	68				
4H-3,20	D			100			trace	2	83				
5H-1,54	D			100	2				57				
5H-1,60	M		100		50							25	25
5H-2,85	D			100					70				
5H-3,40	D			100					69				
5H-5,95	M		100		59	1			37				
6H-3,55	D		2	98	3	1	1		67			1	
6H-3,85.5	M		10	90	1				48				10
6H-6,60	D			100	1				76				
7H-6,50	D			100	1				55			1	1
7H-3,68	D			100	1				76				1
8H-7,13	D			100				2	79				2
8H-5,130	D			100				2	83				
9H-8,53	D			100	2			2	78				
9H-4,12	M		100		71	5		20			2		
9H-3,86	D			100	2	trace			81				
11X-1,58	D			100	2			2	66				
12P-1,30	M		80	20	70	5		5	15				
13X-2,47	M		100		60	9	9		10				
13X-1,43	D			100	1				67				
14X-1,55	D		20	80	15			2	73				
15X-2,59	D			100	5			1	66				
15X-4,43	M		80	20	40	5	1	10	42				
16X-1,18	D			100				3	87				
17X-5,70	D		20	80	7	2			77				
17X-1,50	D			100					80				
18X-1,61	D		5	95	7	1			60				
19X-1,118	M		10	90	5	1			57			1	2
19X-3,70	D			100	2	1			63			1	2
20X-2,125	D			100	1	3			54				
21X-2,40	D			100	5		trace	2	83				
22X-3,50	D			100	3	trace	trace	2	80				
23X-2,90	D			100	5	trace	trace	2	68				
24X-3,70	D			100	2	trace	trace	1	74				
24X-3,119	M		100		90	5		3					2

Table 2. Smear slide data for Hole NGHP-01-05D.

Sample reference		Texture			Mineral								
Core, section, depth (cm, in section)	Lithology	Sand	Silt	Clay	Quartz	Feldspar	Mica	Heavy minerals	Clay minerals	Volcanic glass	Glauco-nite	Iron sulfides	Authigenic carbonates
Hole NGHP-01-05D													
1H-3,53	D			100	5		trace	2	73				
3H-2,79.5	D		5	95	10				54				
3H-4,71	M		95	5	70	20	2		7				
6P-1,50	D			100	1	1			59			1	1
12P-1,50	D			100	1	1	1					1	1
4H-4,91.5	D			100	1				66				1
7Y-1,64	M		80	20	60	20		9					10
11Y-1,44	D			100	1	1			77				

Table 1 Smear slide data for Hole NGHP-01-05C.—Continued

Sample reference		Biogenic							Comments
Core, section, depth (cm, in section)	Lithology	Fora-minifera	Nanno-fossils	Carbonate shell fragments	Diatoms	Radio-larians	Sponge spicules	Plant debris	
NGHP-01-05C—Continued									
1H-1,40	D		40					trace	
1H-2,14	D		40					2	
2H-3,60	D		10					1	
2H-1,73	M	5	5						From silt layer, framboidal pyrite
3H-2,70.5	D	6	50					2	
3H-4,37	D	6	50					2	
3H-6,121.5	D		50					1	
4H-6,50	D		15					5	
4H-3,20	D		10					5	
5H-1,54	D		40					1	
5H-1,60	M							trace	From silt layer.
5H-2,85	D		30						
5H-3,40	D		30					1	
5H-5,95	M							3	Take from flow-in feature.
6H-3,55	D	1	25					1	Possible trace glauconite.
6H-3,85.5	M	1	40						
6H-6,60	D	1	20					1	
7H-6,50	D	1	40					1	
7H-3,68	D		30					2	
8H-7,13	D		12					5	
8H-5,130	D		10					5	
9H-8,53	D	3	10					5	
9H-4,12	M	2							From a silt layer.
9H-3,86	D	2	10					5	
11X-1,58	D		25					5	
12P-1,30	M							5	
13X-2,47	M							2	From a silt layer.
13X-1,43	D		30					2	Silt sized plant debris.
14X-1,55	D		5					5	
15X-2,59	D		30						
15X-4,43	M							2	
16X-1,18	D		10						
17X-5,70	D		8					6	
17X-1,50	D		20						
18X-1,61	D		30					3	Some silt sized organic material.
19X-1,118	M	1	30					3	Silt sized plant debris.
19X-3,70	D	1	30						Carbonate needles
20X-2,125	D	1	40					1	Possilbe glauconite, silt sized grains.
21X-2,40	D		10					trace	
22X-3,50	D		15					trace	
23X-2,90	D		20					5	
24X-3,70	D		20					3	
24X-3,119	M	trace							Plag is the main feldspar.

Note: M = minor lithology, D = dominant lithology.

Table 2. Smear slide data for Hole NGHP-01-05D.—Continued

Sample reference		Biogenic							Comments
Core, section, depth (cm, in section)	Lithology	Fora-minifera	Nanno-fossils	Carbonate shell fragments	Diatoms	Radio-larians	Sponge spicules	Plant debris	
Hole NGHP-01-05D—Continued									
1H-3,53	D		20	trace			trace		
3H-2,79.5	D		35						
3H-4,71	M		1						
6P-1,50	D	1	35	trace				1	Trace mica and framboidal pyrite.
12P-1,50	D	1	30	trace				1	Trace amphibole, diatoms.
4H-4,91.5	D	1	30					1	Trace mica, feldspar, framboidal pyrite.
7Y-1,64	M	1		trace					
11Y-1,44	D		20					1	

Note: M = minor lithology, D = dominant lithology.

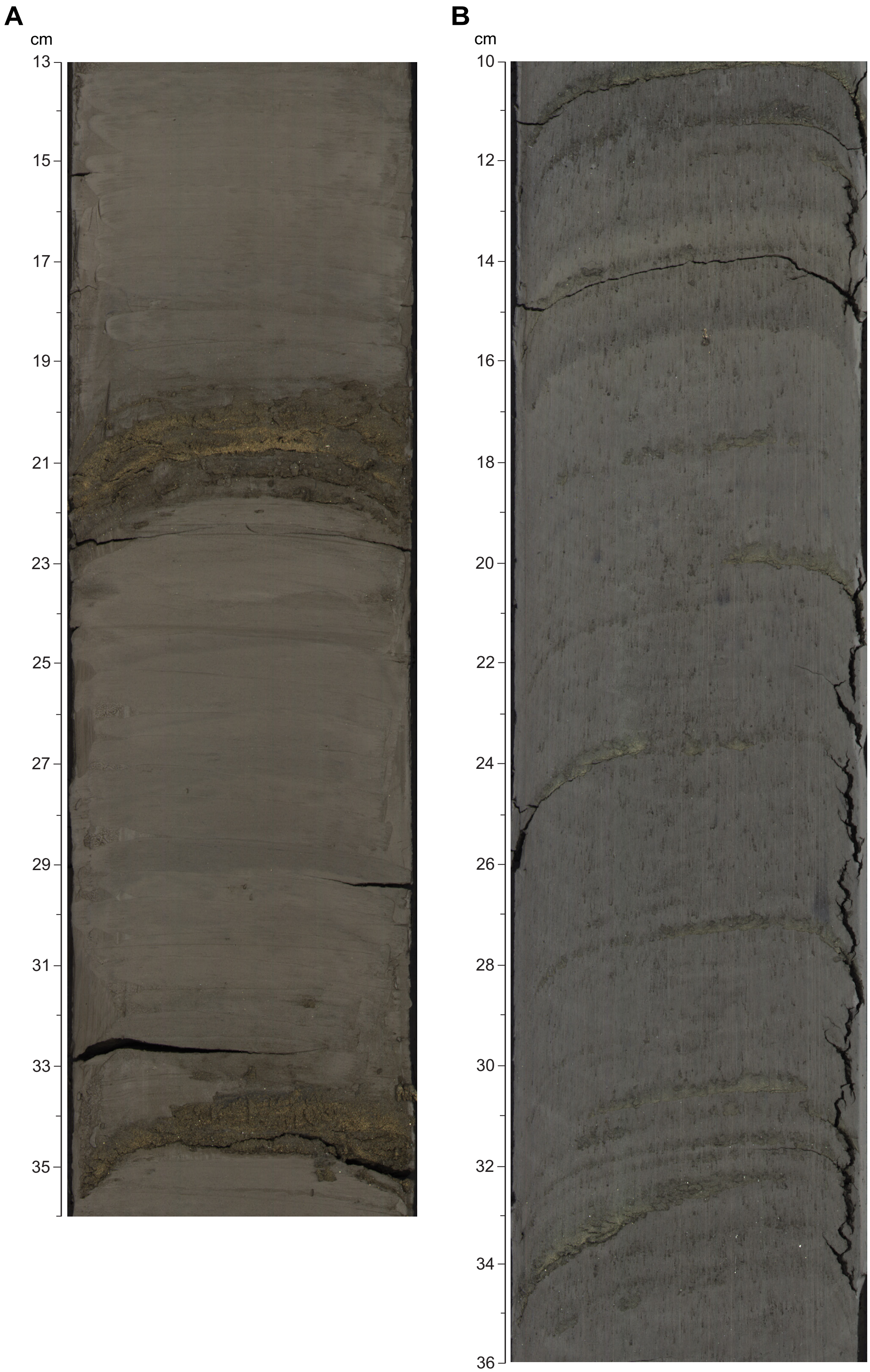

Figure 7. A, Silt laminae and beds from Section NGHP-01-05C-03H-7 and B, Section NGHP-01-05C-05H-2.

Table 3. Silt laminae and beds at Hole NGHP-01-05C.

Core, section	Position start	Position end	Depth top (mbsf)	Depth base (mbsf)	Type
			NGHP-01-05C		
20X-2	0	140	155.8	157.2	Silt laminae
20X-2	88	88	156.68	156.68	Silt bed
20X-2	91	91	156.71	156.71	Silt bed
20X-2	95	95	156.75	156.75	Silt bed
20X-2	106	106	156.86	156.86	Silt bed
20X-2	110	110	156.9	156.9	Silt bed
20X-2	113	114	156.93	156.94	Silt bed
20X-3	0	75	157.3	158.05	Silt laminae
20X-4	0	90	158.8	159.7	Silt laminae
21X-1	0	150	163.9	165.4	Silt beds
21X-2	0	75	165.4	166.15	Silt laminae
21X-3	9	90	166.99	167.8	Silt laminae
22X-1	0	150	173.53	175.03	Silt laminae
22X-1	85	86	174.38	174.39	Silt/v.f.sand beds
22X-1	88	89	174.41	174.42	Silt/v.f.sand beds
22X-2	0	140	175.03	176.43	Silt laminae
22X-3	77	76	177.3	177.29	Silt/v.f.sand beds
22X-4	56	57	178.59	178.6	Silt/v.f.sand beds
23X-3	5	5.5	186.15	186.155	Silt laminae
24X-3	117	119	196.87	196.89	Silt laminae
24X-4	47	48	196.17	196.18	Silt laminae
24X-4	51.5	53.5	196.215	196.235	Silt laminae
24X-4	62	63	196.32	196.33	Silt laminae
24X-5	0	3	198.2	198.23	Silt laminae

Gas-Hydrate Occurrence

Gas hydrates were inferred from the LWD data at Site NGHP-01-05 and recovered in some cores on the catwalk (where they were identified through IR images). Gas-hydrate occurrences at this site were interpreted to be disseminated accumulations throughout the cores that dissociated during the ascent from the seafloor to the ship. Two interstitial water (IW) samples associated with IR (infra-red) cold spots showed that the gas hydrate existed within silt beds (see “Inorganic Geochemistry”). X rays and logs from pressure cores document gas hydrate present as vein fills and in some horizontal bands (see “Pressure Coring”). Upon examination of the pressure cores, however, no obvious lithologic variation or control (in terms of grain size) was observed; implying the gas hydrate occupied fractures within the nannofossil bearing clay stratigraphy. Both of these observations of the distribution of gas hydrate within the sediments are constrained by limited data availability due to poor core recovery, abundant whole-round sampling of the cores on the catwalk, and limited pressure cores. Mousse-like and soupy sediments commonly result from the destabilization of gas hydrate in cores, however, in the cores described on the sedimentology table, only a few soupy and mousse-like textures were observed (figs. 5, 6, and Site NGHP-01-05 Visual Core Descriptions in the supplemental data files).

Table 4. Silt laminae and beds at Hole NGHP-01-05D.

Core, section	Position start	Position end	Depth top (mbsf)	Depth base (mbsf)	Type
			NGHP-01-05D		
1H-1	80	84	0.8	0.84	Silty burrow
1H-3	38	40	3.38	3.4	Multiple silt laminae
1H-3	90	91	3.9	3.91	Silt laminae
1H-3	104	110	4.04	4.1	Silt bed with laminae
1H-5	57	57.5	6.57	6.575	Silt laminae
2H-2	92	92.5	9.82	9.825	Silt laminae
2H-2	94	94.5	9.84	9.845	Silt laminae
2H-4	7	7.5	11.97	11.975	Silt bed
2H-4	44	46	12.34	12.36	Silt bed
2H-4	95	95.5	12.85	12.855	Silt bed
7P-1	14.5	15	77.045	77.05	Silt bed
7P-1	15.5	16	77.055	77.06	Silt bed
7P-1	17	17.5	77.07	77.075	Silt bed
7P-1	21	21.5	77.11	77.115	Silt bed
7P-1	26	26.5	77.16	77.165	Silt bed
7P-1	27.5	28	77.175	77.18	Silt bed
7P-1	49.5	50	77.395	77.4	Silt bed
7P-1	51	51.5	77.41	77.415	Silt bed
7P-1	61	62	77.51	77.52	Silt bed
7P-1	40	46	77.3	77.36	Multiple silt laminae
7P-1	62	65	77.52	77.55	Multiple silt laminae
7P-1	70	74	77.6	77.64	Multiple silt laminae
7P-1	78	79	77.68	77.69	Silt laminae

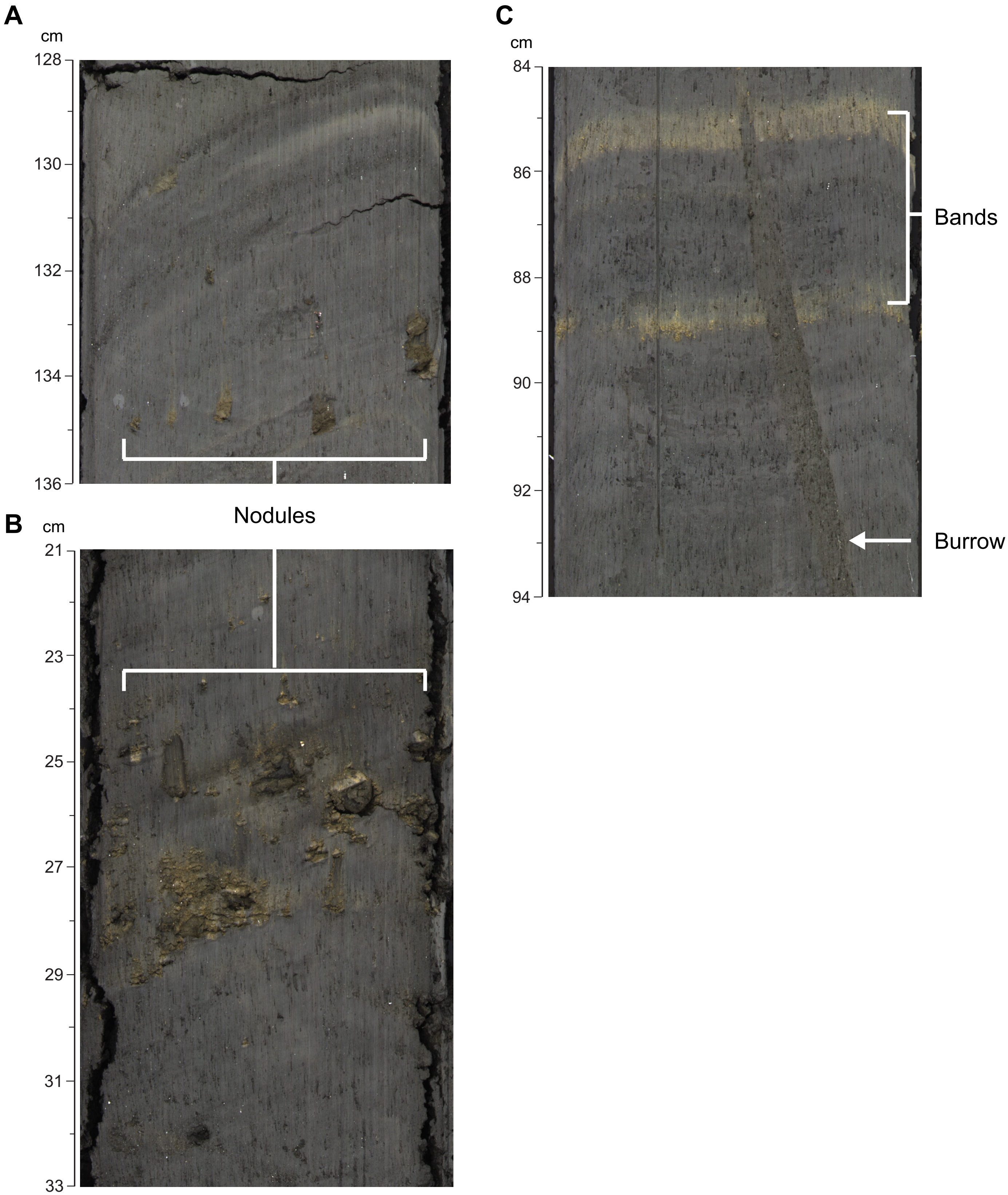

Figure 8. Authigenic carbonate nodules A, Section NGHP-01-05C-05H-5, B, Section NGHP-01-05C-17X-4 and bands C, Section NGHP-01-05C-6H-3. Notice in C the burrow cross-cuts the carbonate band, implying the authigenic carbonate formed relatively close to the seafloor, while the sediments were still in the zone of active bioturbation (10 cm to ~1 mbsf). Vertical scale in centimeters down core section. [msbf, meters below sea floor]

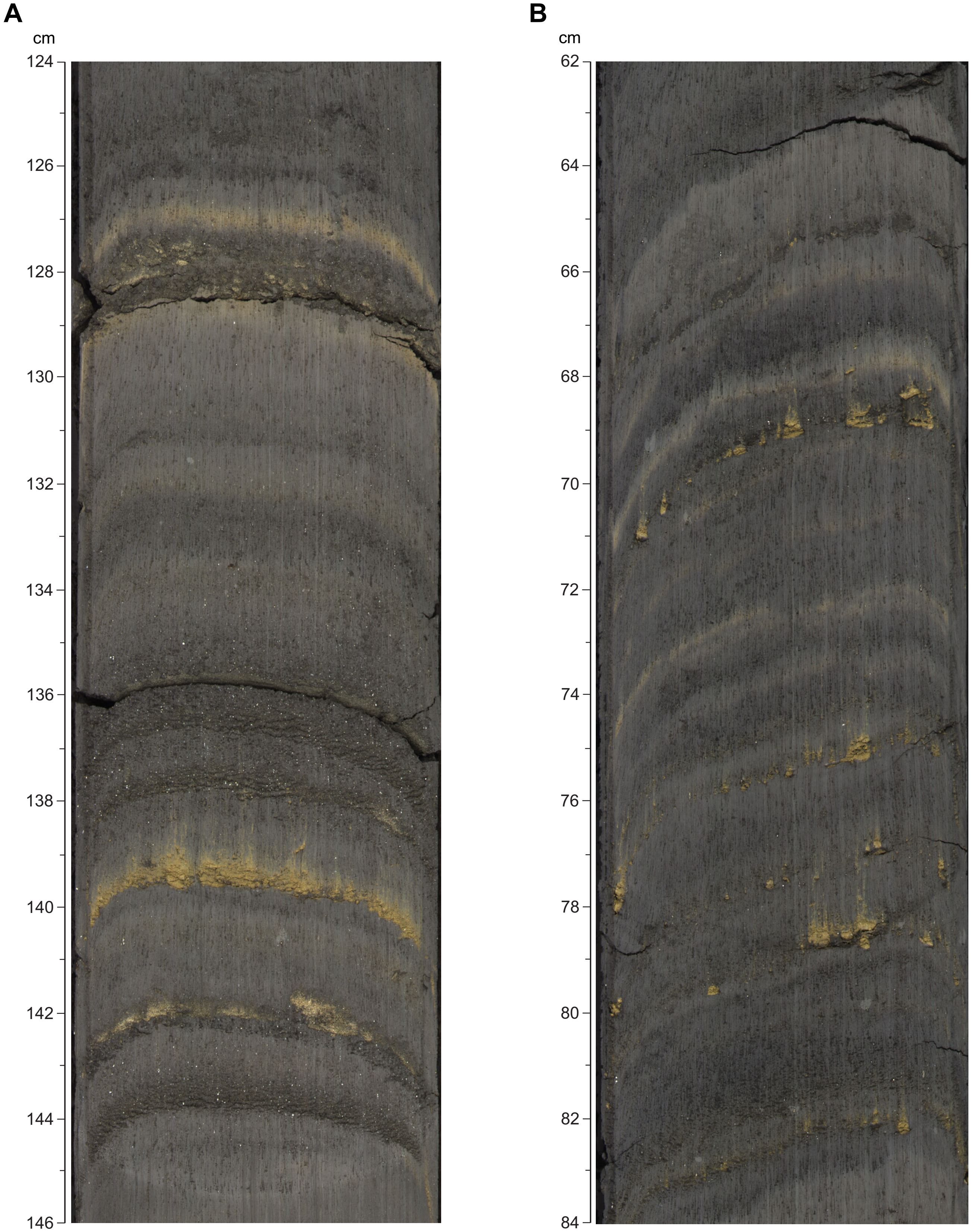

Figure 9. Succession of silt laminae and beds and carbonate bands and nodule bands in banded clayey matrix. A, Section NGHP-01-05C-07H-3 and B, Section NGHP-01-05C-08H-5. Vertical scale in centimeters down core section.

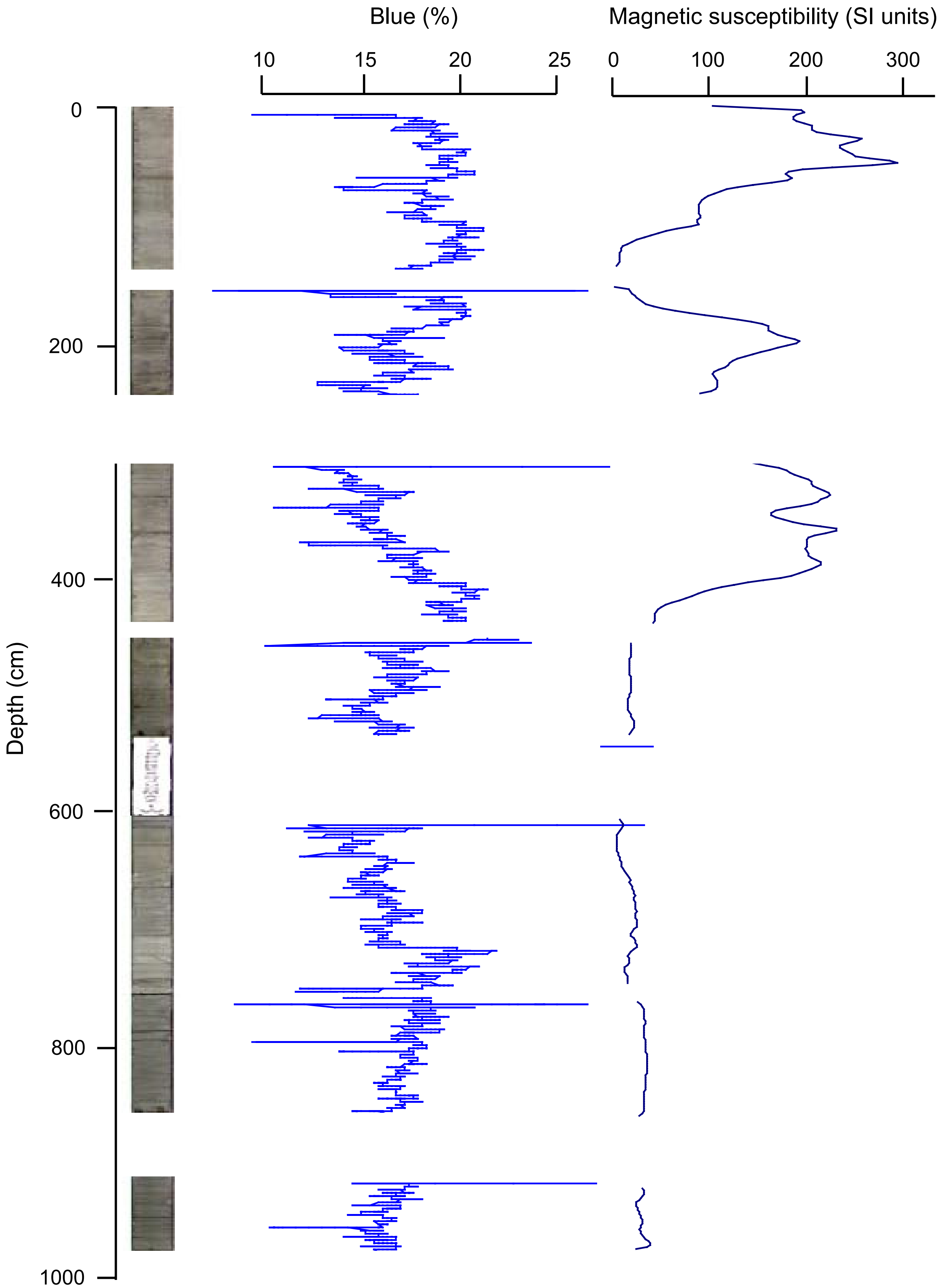

Figure 10. Apparent cyclicity in color of clays represented by DIS-derived blue (blue in percent). Also shown is magnetic susceptibility (SI units) from Core NGHP-01-05C-04H.

Inorganic Geochemistry

The main objectives of the inorganic geochemistry program at this site were to (1) constrain the fluid and gas source(s), subsurface hydrology (transport mechanisms and migration pathways), and biogeochemical reactions associated with subsurface gas hydrate; (2) quantify the content and distribution of gas hydrate based on dissolved chloride concentrations and determine the relationship between the regional hydrogeochemistry and gas-hydrate distribution. The primary objective of the high-resolution sampling in Hole NGHP-01-05D was to characterize the SMI for future geochemical modeling studies and to provide supporting data and samples for studies on the microbial dynamics of the sulfate-methane interface (SMI). The IW geochemistry data are tabulated in tables 5 and 6, and illustrated in figures 11 and 12.

A total of 63 whole-round samples were collected for interstitial water analyses at Site NGHP-01-05 in the Krishna-Godavari Basin offshore the eastern continental margin of the Indian Peninsula (40 samples from Hole NGHP-01-05C and 23 samples from Hole NGHP-01-05D). Whole-round lengths ranged from 10 to 20 cm, with longer sections subsampled from cores recovered deeper within the hole. Samples were collected at Hole NGHP-01-05C at a frequency of 4 samples per core in the upper 20 m, 3 whole-round samples per core to 40 m, 2 to 3 samples per core to the seismically inferred BSR, and 1 sample per core beneath the BSR. Samples were collected at higher spatial resolution in Hole NGHP-01-05D to better define the SMI, to quantify the magnitude of anaerobic methane oxidation (AMO) at this site, as well as for future geochemical and microbiological studies. In the high-resolution hole, 7 samples were taken per core from the seafloor to 10 m below the SMI.

Table 5. Interstitial-water data for Hole NGHP-01-05C. Note that a dash indicates the value was not determined.

Core, section	Top	Bottom	Depth (mbsf)	Volume (mL)	pH	Alkalinity (mM)	Salinity	Cl^- (mM)*	Br^- (mM)	SO_4^{2-} (mM)
NGHP-01-05C										
1H-1	140	150	1.4	35	-	-	34.5	558	0.92	22.51
2H-1	140	150	3.7	34	-	-	34.5	555	0.88	15.08
2H-3	140	150	6.7	35	7.5	19.40	34.5	556	0.91	13.20
2H-5	140	150	9.7	32	7.7	17.88	32.0	555	0.92	13.00
2H-7	50	60	11.3	30	7.7	-	30.0	556	0.91	13.38
3H-1	140	150	13.2	27	7.8	15.32	32.5	558	0.91	12.29
3H-3	140	150	16.2	33	7.8	13.06	33.0	557	0.91	11.87
3H-5	140	150	19.2	38	7.8	13.01	33.5	557	-	10.26
4H-2	140	150	24.2	31	-	19.00	33.5	559	0.93	0.18
4H-4	140	150	27.2	31	7.8	19.17	33.5	559	0.95	0.00
4H-6	140	150	30.2	22	8.0	20.12	33.5	567	1.00	0.00
5H-2	140	150	33.6	29	8.0	24.06	34.0	568	1.04	0.00
5H-4	134	144	36.5	26	7.9	27.07	34.0	571	1.09	0.00
5H-6	138	148	39.5	15	7.9	27.05	34.5	576	1.09	0.00
6H-3	140	150	43.2	20	7.8	26.00	34.5	575	1.14	0.00
6H-5	140	150	46.2	25	7.8	20.14	34.5	577	1.19	0.00
7H-2	140	150	52.6	19	7.7	16.75	32.5	574	1.22	0.51
7H-5	140	150	57.1	15	7.7	16.41	33.0	575	1.21	0.00
8H-2	140	150	62.2	24	7.7	14.19	32.0	576	1.29	0.13
8H-5	140	150	66.7	24	7.8	11.75	32.0	572	1.22	0.00
9H-2	98	108	70.4	27	7.7	13.50	31.0	558	1.16	0.29
9H-5	140	150	74.8	36	7.5	12.44	32.0	566	1.22	0.00
10P-1	0	10	78.3	-	-	-	-	-	-	-
11X-1	82	102	80.1	14	-	11.07	33.5	557	1.26	0.53
12P-1	5	15	86.1	18	7.6	8.76	-	-	1.19	0.52
12P-1	36	46	86.4	15	7.4	8.01	-	-	-	-
13X-1	110	130	88.1	17	7.8	-	30	547	-	-
13X-2	50	60	88.8	5	7.8	9.27	22.5	540	1.14	1.78
13X-3	130	150	90.2	26	-	-	30.0	-	-	-
14X-2	19	29	98.6	10	-	-	30.0	-	-	-
16X-1	108	128	116.9	12	8.0	7.24	29.5	527	1.14	0.43
17X-2	130	150	128.3	34	7.8	17.78	31.0	519	1.09	0.98
17X-5	125	145	132.8	22	7.9	23.78	31.0	522	1.11	0.97
18X-1	130	150	136.4	23	7.9	32.23	30.5	520	1.12	0.44
18X-3	101	121	139.1	22	7.8	-	33.0	526	1.13	0.33
20X-3	130	150	158.6	27	7.8	51.23	34.0	537	1.18	0.29
21X-2	130	150	166.7	21	7.9	50.54	34.5	543	1.18	0.23
22X-3	130	150	177.8	13	7.9	49.94	34.5	537	1.17	0.00
23X-1	130	150	184.4	9	7.5	-	34.5	544	1.19	0.00
24X-2	130	150	195.5	12	7.8	49.82	34.5	544	1.21	0.00

Note: *Cl^- analysis by titration.

Table 6. Interstitial water data for Hole NGHP-01-05D. Note that a dash indicates the value was not determined.

Core, section	Top	Bottom	Depth (mbsf)	Volume (mL)	pH	Alkalinity (mM)	Salinity	Cl^- (mM)*	Br^- (mM)	SO_4^{2-} (mM)
				NGHP-01-05D						
1H-2	140	150	2.9	35	-	13.71	34.5	561	0.82	15.8
1H-4	140	150	5.9	38	7.4	24.31	34.5	534	0.79	6.7
1H-5	118	128	7.18	33	7.7	25.66	34.0	557	0.83	5.8
2H-2	70	80	9.6	30	7.6	-	34.0	561	0.85	0.0
2H-2	140	150	10.3	30	7.4	26.92	33.5	553	0.83	1.2
2H-3	70	80	11.1	30	8.2	26.72	33.5	566	0.85	0.3
2H-4	70	80	12.6	28	-	24.46	33.5	456	0.68	0.0
2H-4	140	150	13.3	26	8.3	24.85	34.0	553	0.82	0.0
2H-5	70	80	14.1	27		23.05	33.5	-	0.72	0.0
2H-6	140	150	16.3	30	8.2	23.05	34.0	554	0.85	0.0
3H-1	140	150	18.3	33	8.2	18.64	33.0	555	0.84	0.0
3H-2	140	150	19.8	35	-	-	33.0	556	-	-
3H-3	140	150	21.3	35	-	22.07	31.0	560	0.85	0.0
3H-4	130	150	22.7	36	-	22.30	30.5	551	-	-
3H-5	65	75	23.55	35	8.4	21.42	31.0	568	-	-
3H-6	86	96	24.51	36	8.4	20.51	32.0	553	0.89	0.0
3H-7	0	38	24.61	-	-	-	-	-	-	-
4H-2	140	150	29.3	35	8.4	23.01	31.5	553	-	-
4H-6	71	81	34.53	25	8.1	25.30	33.5	558	-	0.0
6P-1	16	26	77.06	25	7.4	14.58	33.0	535	-	-
11Y-1	70	80	125.6	17	8.0	-	29.5	565	-	-
12P-1	30	37	200.3	16	7.8	36.40	35.5	550	-	-
12P-1	65	75	200.65	11	-	-	34.5	545	-	-

Note: *Cl^- analysis by titration

Two whole-rounds were taken per core beneath the SMI. The whole-round sampling program was coordinated with both the organic geochemistry and microbiology sampling programs. In addition to the general whole-round sampling scheme, intervals with IR anomalies were sampled on the catwalk. The IR anomaly whole-round samples were immediately transferred to the chemistry laboratory, taken out of the core liner, split in half, and imaged with a hand-held IR camera. The sediment section containing the IR anomaly was then separated from the whole-round sample and squeezed. If the anomaly was heterogeneous, then lithologies were separated (that is silt and clay) and squeezed separately to determine the percent pore-space gas-hydrate occupancy of each sediment type. Pressure cores were subsampled for squeezing based on X-ray logs. Typically, one gas hydrate sample and one background sample were collected per pressure core, and Cl^- concentration in each subsample will be used to determine the percent hydrate in gas-hydrate-bearing sections.

Interstitial Water Chloride—Gas-Hydrate Distribution

The Cl^- concentration depth profile at this site shows four distinct zones (fig. 11A). Between the seafloor and 27 mbsf, Cl^- concentrations range between 555 mM and 559 mM. Pore-fluid Cl^- concentrations increase markedly from 27 to 46 mbsf where concentrations peak at 577 mM (3.2 percent greater than modern seawater value). The abrupt change from Cl^- concentrations similar to modern seawater (SW) to elevated pore-water Cl^- concentrations at 27 mbsf likely reflects buried interglacial seawater with an average chloride concentration of ~579 mM (3.5 percent greater than modern seawater). Chloride concentrations remain elevated above modern seawater concentration to a depth of 75 mbsf. The origin of the higher than seawater Cl^- concentrations between ~30 to 65 mbsf is not yet understood.

The third zone of interest is from 70 to 140 mbsf (fig. 11A), and is characterized by progressively depleted Cl^- concentrations with depth ranging from 558 mM at 70 mbsf to 519 mM at 128 mbsf. The depletion in Cl^- concentrations most likely reflects *in situ* dilution of the interstitial waters by gas-hydrate dissociation induced during the core retrieval process. Two of the interstitial water whole-round samples (NGHP-01-05C-13X-2, 50–60 and NGHP-01-05C-14X-2, 19–29) were associated with IR anomalies observed on the catwalk. These whole-rounds were immediately transferred to the chemistry laboratory and scanned with a hand-held IR camera. The IR anomalies were very focused and associated with laminations of silt to very fine sand bounded by clay (fig. 13), indicating that some of the gas hydrate at this site is associated with coarser grained sediments. The lithologies were separated and the silty sediment was squeezed. The Cl^- concentration of sample NGHP-01-05C-13X-2 was 540 mM, and the Cl^- concentration of sample NGHP-01-05C-14X-2 was not determined shipboard because

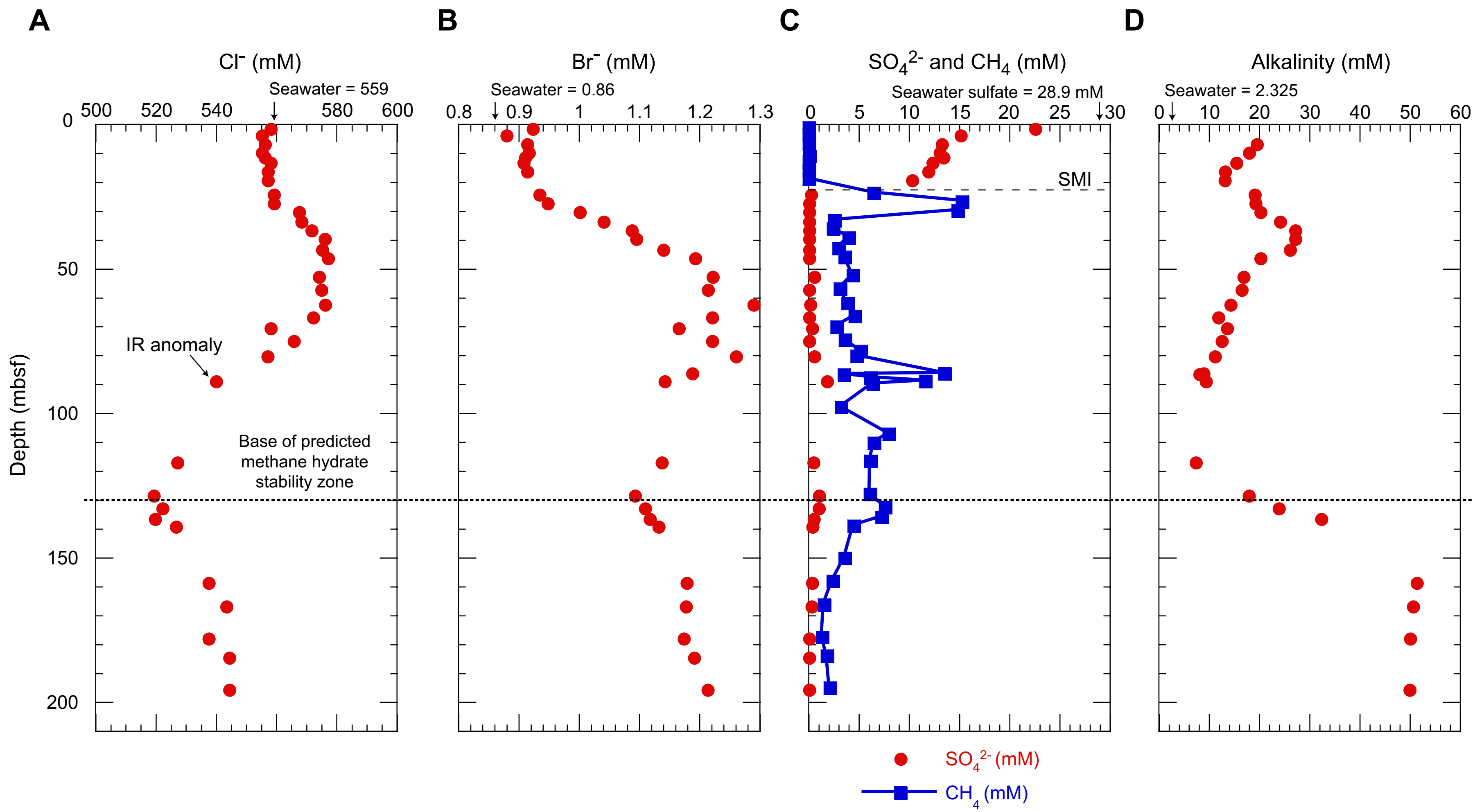

Figure 11. Concentration depth profiles of A, chloride (errors are smaller than the symbols); B, bromide; *C*, sulfate and methane; and *D*, alkalinity at Hole NGHP-01-05C.

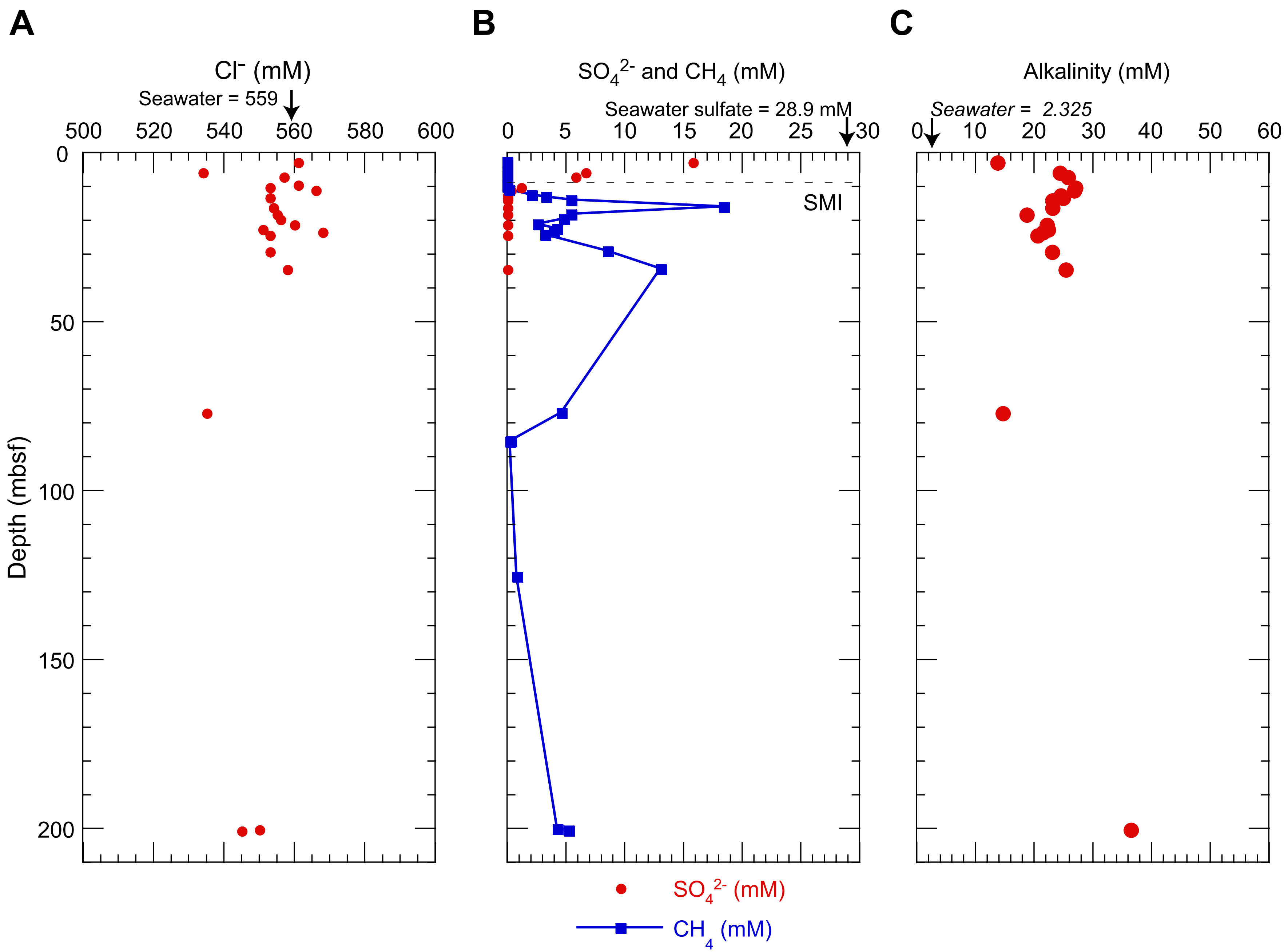

Figure 12. Concentration depth profiles of A, chloride (errors are smaller than the symbols); B, bromide; C, sulfate and methane; and D, alkalinity at Hole NGHP-01-05D.

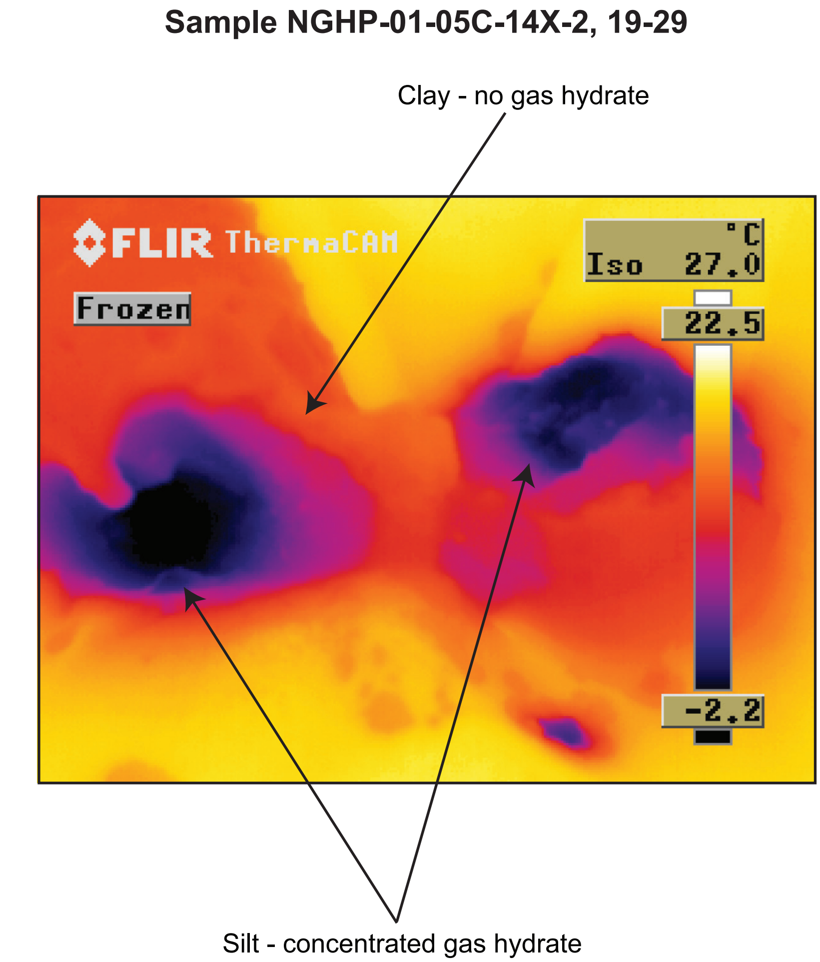

Figure 13. Infrared image of a gas hydrate bearing silt (blue) surrounded by clay (red) from sample NGHP-01-05C-14X-2, 19–29 cm.

of low recovery of pore fluid from the silty section of this sample. The Cl^- concentration of the IR anomaly in sample NGHP-01-05C-14X-2 was determined in our shore-based laboratory. The minima in Cl^- concentrations occurs at a depth of 130 mbsf and remains depleted to 140 mbsf, which places constraints on the base of the gas-hydrate stability zone at this site. Headspace methane concentrations also decrease at this depth (see "Organic Geochemistry"). Based on the relative dilution of the Cl^- concentration depth profile, gas hydrate is most abundant at the base of the gas-hydrate stability zone and gas-hydrate concentration decreases up section. The extent of Cl^- dilution coupled with background Cl^- concentrations will be used to model the amount of pore space occupied by gas hydrate at this site. The downhole logging shows gas hydrate is present from 55 to 95 mbsf (fig. 43B).

The fourth zone is below 140 mbsf, where Cl^- concentrations remain fairly constant and range from 537 to 544 mM. The Cl^- concentrations within this interval likely reflect *in situ* formation fluid with slightly depleted Cl^- values due to gas-hydrate dissociation as the section shifted out of the gas-hydrate stability zone by progressive burial.

Sulfate Concentrations and the SMI

The primary objectives of the high-resolution sampling in the upper 20 m of sediment at this site were to characterize the SMI for future geochemical modeling of methane fluxes and to provide supporting data and samples for studies on the microbial dynamics of the sulfate-methane interface. Above the interface, sulfate reducing microbial communities utilize interstitial sulfate to oxidize sedimentary organic matter, reducing sulfate to sulfide and producing bicarbonate. Below the interface, methanogens generate methane. At the interface, in some environments (especially diffusive settings), microorganisms symbiotically reduce sulfate and oxidize methane by anaerobic methane oxidation (AMO). The net biogeochemical process is described by:

$$CH_4 + SO_4^{2-} \rightarrow HCO^{3-} + HS^- + H_2O$$

(Reeburgh, 1976). When methane oxidation by AMO is complete, usually in diffusional settings, but not necessarily in advection-dominated environments, all of the methane fluxing upward is consumed before entering the water column. AMO also drives precipitation of authigenic carbonates, affecting carbon chemistry both above and below the SMI. The d^{13}C of dissolved organic carbon produced by anaerobic methane oxidation is depleted with respect to that produced by oxidation of organic matter by sulfate, and shore-based samples for carbon isotopic analyses were preserved to determine the presence and relative amount of AMO occurring at Site NGHP-01-05. High-resolution microbiological samples were also collected from the seafloor across the SMI.

In Hole NGHP-01-05C, the SMI is located at approximately 24 mbsf (fig. 11C), whereas the SMI is located at ~11.5 mbsf at Hole NGHP-01-05D (fig. 12C). At Site NGHP-01-05C sulfate is 22.5 mM at 1.4 mbsf and is totally depleted by 24 mbsf, whereas sulfate decreases from 15.8 mM at 2.9 mbsf to zero sulfate by 11.5 mbsf at Hole NGHP-01-05D. Concomitant with the depleted sulfate at these two depths is a rise in headspace methane values from concentrations below the detection limit (see "Organic Geochemistry"). The reason for the offset of the SMI between the two holes, only ~20 m away from each other, is still under investigation. Below the SMI, sulfate remains depleted with a few minor excursions up to 1.5 mM at depth. These excursions most likely represent contamination of the whole-round samples collected for interstitial water analyses by seawater circulating in the borehole during drilling.

Alkalinity and Bromide

Alkalinity, like Cl^-, can be split into four zones. The first is from 6.7 to 19 mbsf at Hole NGHP-01-05C where alkalinity decreases from 19.4 mM (8 times seawater value) to 13.01 mM (fig. 11D). The drop in alkalinity within this interval may reflect precipitation of authigenic carbonates. From 20 mbsf to 43 mbsf at Hole NGHP-01-05C alkalinity increases to 26 mM reflecting alkalinity production by anaerobic oxidation of methane in the upper portion of the interval, as well as alkalinity produced closer to the surface before burial. Alkalinity at Hole NGHP-01-05D follows a similar profile to that of Hole NGHP-01-05C, except alkalinity is produced in the first 11 m due to oxidation of organic matter by sulfate reduction in the shallower sediments and anaerobic oxidation of methane at 11 m (fig. 12C). Zone 3 is characterized by progressively lower alkalinities from 40 mbsf to 117 mbsf where alkalinity reaches a minimum value of 7.24 mM. The depletion of alkalinity down section within this interval could reflect a combination of precipitation of authigenic carbonates consuming Ca^{2+} (and some Mg^{2+}), varying degrees of trapped ancient seawater mixed with alkalinity produced by organic matter oxidation and AMO when the respective sediment package was close to the surface, and dilution of alkalinity by gas-hydrate dissociation induced during core recovery. From 116 to 158 mbsf, alkalinity increases monotonically to a concentration of 51 mM, after which the alkalinity remains relatively constant to the base of the hole (Zone 4, fig. 11). The high alkalinity in Zone 4, ~50 mM, may have been produced up-section prior to burial or may reflect dissolution of carbonate driven by methanogenesis.

Bromide concentrations are not typically measured shipboard during IODP/ODP cruises. During Leg 3 of NGHP Expedition 01, an ion chromatograph was utilized to measure both SO_4^{2-} and Br^-. Bromide concentrations in marine interstitial waters are sensitive to organic matter diagenesis, with concentrations higher than seawater reflecting marine organic matter decomposition. In Hole NGHP-01-05C, Br^- is slightly higher than seawater value (0.86 mM) in the upper 20 m then increases to approximately 1.28 mM (~20 percent greater than modern SW value) at 50 mbsf (fig. 11B). Sharp minima in the Br^- concentration depth profile between 70 and 100 mbsf reflect dilution by gas-hydrate dissociation overprinted on the background profile during core recovery. Like Cl^- and alkalinity, Br^- concentrations are relatively constant below a depth of 140 mbsf, further indicating that there is no measurable metabolism of marine organic matter at depths greater than 50 mbsf.

Organic Geochemistry

Organic geochemical studies at Site NGHP-01-05 (KGGH-02A) included analysis of the composition of volatile hydrocarbons including methane, ethane, and propane (C_1–C_3) and fixed natural gases (that is, O_2, CO_2, and N_2+Ar) from headspace, void gas, and pressure core sampler (PCS) degassing experiments. In general, these analyses indicate that the predominant hydrocarbon gas found in the cores at this site was methane; however, ethane was measurable in samples collected from pressure-core degassing experiments. Samples collected above the SMI were dominated by air, while C_1 and C_2 hydrocarbon gases were enriched below the SMI and above the seismically-inferred bottom simulating reflector (BSR). The C_1 and C_2 hydrocarbon gas levels decline steadily below the BSR to the TD of 200 mbsf (see below). Specific details of the shipboard gas chemistry results for Site NGHP-01-05, Holes C and D are provided in the following statements.

Headspace gas analyses were performed on 42 samples from Hole NGHP-01-05C and 24 samples from Hole NGHP-01-05D ranging in depth from 1.1 to 200.6 m below seafloor (mbsf). The concentrations given here represent minimum proxy measurements of the actual concentrations due to limitations of the gas headspace method (Kvenvolden and Lorenson, 2000). The sediment pore water contained methane at concentrations ranging from nondetectable near the surface to 8.7 mM at ~16 mbsf (table 7). Theoretical methane saturation in pore water under site-specific physical conditions, calculated using the Duan and others (1992) and Xu (2002, 2004) methodologies, ranges from 63.7 mM at the seafloor to 117.8 mM at 130 mbsf, then declines to 114.9 mM near the borehole completion depth of 200 mbsf. C_2 and C_3 hydrocarbon gases were not detected in headspace samples suggesting a microbial source of hydrocarbon gases. Methane concentrations are highest just above 15 mbsf likely denoting the sulfate-methane interface (SMI), and increase again at ~85 mbsf (fig. 14). The upper methane concentration peak was confirmed in Hole NGHP-01-05D, however was offset ~5 m in this borehole (fig. 14). The lower methane concentration peak at about 90 mbsf lies nearly 40 m above the inferred BSR and represents sediment with higher concentrations of gas hydrate. Other proxy measurements such as an IR temperature anomoly and pore water Cl^- decrease (see "Inorganic Geochemistry") also indicate gas hydrate occurence. Downhole logging (figure 43B) shows a high concentration of gas hydrate from 55 to 95 mbsf. Methane concentration decreases below the BSR and are generally at levels below saturation. The presence of methane levels similar to SMI concentrations below the BSR, may imply that methane gas bubbles exist below at depth (fig. 14). There is a slight increase in methane concentration just below the BSR inferring that methane gas is trapped below the BSR at depths of about 135–140 mbsf.

Carbon dioxide (CO_2) concentrations ranged from 0.4 to 16.3 mM in pore water contained within the sediment. An equivalent concentration expression of gas volume to sediment volume ranges from 7,100 to nearly 180,000 microliters CO_2/liter wet sediment (table 7). There is no consistent, fine-scale trend in the CO_2 concentration with depth; however, the results can be roughly divided into three zones based on CO_2 concentrations. The highest CO_2 concentrations are found below the BSR ranging from 140 to 165 mbsf (fig. 15). No apparent change in lithology could be inferred at or near this interval. More intermediate concentrations were found in the interval below the SMI and above the BSR, and could be associated with gas hydrate. The lowest concentrations are found in the upper 15 mbsf above the SMI. The methane-to-carbon-dioxide ratio for headspace also reflects these zones, indicating that methane is preferentially concentrated between the SMI and BSR (fig. 16). The air gases (N_2+Ar), and O_2 were the balance gases, however the (N_2+Ar)/O_2 ratios were typically greater than air and may reflect a higher ratio in pore fluids, as well as present a partitioning of O_2 into the pore fluids over N_2 from air trapped in the headspace samples. The (N_2+Ar)/O_2 ratio represents air concentration plus pore fluid composition. Air gases are present in all samples as the core plugs were degassed in an air headspace.

Void gas samples were collected from twenty different intervals ranging in depth from 16.2 to 72.4 mbsf. The void gas samples contained methane at all intervals except the uppermost 16.2 mbsf (above the SMI), as noted in table 8. Methane concentrations within voids averaged nearly 850,000 ppm (±294,000); however higher molecular weight hydrocarbon gases were not detected. Carbon dioxide concentrations ranged from 686 to 62,300 ppmv and are tabulated with other gas data in table 8. The methane to carbon dioxide ratios are higher in the depths between the SMI and BSR indicating that gas hydrate has concentrated the methane relative to carbon dioxide (fig. 16). This trend occurs in headspace gas samples although the magnitude of the ratios is typically two orders less due to the preferential loss of volatile methane by the headspace sample method. The air gases (N_2+Ar), and O_2 composed the balance gases, and represent concentration in the sediments plus air contamination.

Gas was collected from six pressure-core sampler (PCS) cores, two in Hole NGHP-01-05C and four in Hole NGHP-01-05D. The gas concentration results are very similar to the void gas results (tables 8 and 9); however, CO_2 concentrations were approximately 10 fold lower (see explanation in "Organic geochemistry" in "Site NGHP-01-03". PCS core gases did indicate the presence of C_2 with concentrations ranging from non-detectable to ~50 ppmv. Ratio values for C_1 to C_2 gases ranged from ~20,500 to ~100,000 and showed no apparent trend with depth (fig. 17). The high methane concentrations versus low concentrations of ethane are strong evidence of a microbially-dominated hydrocarbon gas source.

Microbiology

Hole NGHP-01-05C

Analysis of all microbiological samples for this expedition is shore-based. Twenty-one samples were collected for cell enumeration (CEL) and 18 samples for hydrogenase activity analysis (SPH) (table 10). Sampling followed the procedures described in the "Methods" section. Additional microbiological samples were taken (Lab code JUD, 37 samples; Lab code JAN, 18 samples).

Hole NGHP-01-05D

Eleven samples with Lab code JAN were collected (table 10).

Physical Properties

The physical properties program at Site NGHP-01-05 concentrated on Hole NGHP-01-05C and consisted of infrared (IR) imaging of whole-round cores on the catwalk to determine the location of temperature anomalies and the removal of sediment sections for gas-hydrate preservation and study. Nondestructive measurements were conducted on temperature-equilibrated whole-round core sections with the MSCL. Thermal conductivity measurements were also performed on whole-round cores. Various tests were conducted on split cores including: electrical resistivity by use of a Wenner array, P-wave velocity by an inserted spade, and shear strength by mini-vane, Torvane, and Pocket Penetrometer. Core subsamples were placed in 10-mL beakers and dried at 105 °C to determine water content. The dried samples were further analyzed for grain density using gas pycnometers and phase relations were then calculated. Only MSCL and four moisture and density (MAD) samples on pressure cores were processed for Hole NGHP-01-05D. See the "Physical Properties" section of the "Methods" chapter for more details.

Table 7. Headspace gas (HS) composition for Site NGHP-01-05.

Sample	Site	Hole	Core	Section	Interval (cm)	Sed wt. (g)	Sample depth (mbsf)	CO_2	C_1	C_2	C_3
								(ppm-v)			
05C-1H1-105-110	5	C	1	1	105–110	7.3	1.1	11,000	nd	nd	nd
05C-2H1-105-110	5	C	2	1	105–110	7.0	3.4	15,800	nd	nd	nd
05C-2H3-105-110	5	C	2	3	105–110	6.1	6.4	16,200	nd	nd	nd
05C-2H7-15-20	5	C	2	7	15–20	7.4	11.0	11,600	100	nd	nd
05C-3H1-105-110	5	C	3	1	105–110	8.1	12.9	6,400	nd	nd	nd
05C-3H3-105-110	5	C	3	3	105–110	17.4	15.9	13,100	nd	nd	nd
05C-3H5-105-110	5	C	3	5	105–110	15.2	18.9	19,000	nd	nd	nd
05C-4H2-95-100	5	C	4	2	95–100	14.0	23.8	47,900	31,700	nd	nd
05C-4H4-95-100	5	C	4	4	95–100	14.6	26.6	37,000	79,000	nd	nd
05C-4H6-95-100	5	C	4	6	95–100	16.6	29.8	31,800	92,000	nd	nd
05C-5H2-95-100	5	C	5	2	95–100	13.4	33.1	30,100	11,800	nd	nd
05C-5H4-95-100	5	C	5	4	95–100	12.2	36.0	36,400	9,900	nd	nd
05C-5H6-95-100	5	C	5	6	95–100	12.1	39.0	42,200	16,000	nd	nd
05C-6H3-95-100	5	C	6	3	95–100	13.4	42.8	67,400	13,600	nd	nd
05C-6H5-105-110	5	C	6	5	105–110	11.7	45.8	63,700	13,900	nd	nd
05C-7H2-95-100	5	C	7	2	95–100	12.6	52.2	53,600	18,700	nd	nd
05C-7H5-105-110	5	C	7	5	105–110	12.2	56.8	35,900	10,600	nd	nd
05C-8H2-95-100	5	C	8	2	95–100	12.5	61.8	56,000	13,500	nd	nd
05C-8H5-105-110	5	C	8	5	105–110	11.8	66.4	57,800	15,000	nd	nd
05C-9H2-95-100	5	C	9	2	95–100	10.8	69.9	21,900	8,000	nd	nd
05C-9H5-105-110	5	C	9	5	105–110	9.5	74.5	21,800	9,000	nd	nd
05C-10P-10-15-1	5	C	10	1	10–15	8.3	78.4	24,200	11,000	nd	nd
05C-11X1-77-82	5	C	11	1	77–82	8.4	80.1	26,000	10,300	nd	nd
05C-12P-15-20	5	C	12	P	15–20	6.4	86.2	10,700	21,300	nd	nd
05C-12P-46-51	5	C	12	P	46–51	5.8	86.5	11,000	5,000	nd	nd
05C-13X1-65-70	5	C	13	1	65–70	10.0	87.7	21,200	13,100	nd	nd
05C-13X2-45-50	5	C	13	2	45–50	10.9	88.8	10,100	27,400	nd	nd
05C-13X3-85-90	5	C	13	3	85–90	10.7	89.8	14,200	14,800	nd	nd
05C-14X1-85-90	5	C	14	1	85–90	13.4	97.8	23,200	9,900	nd	nd
05C-15X1-85-90	5	C	15	1	85–90	14.7	107.1	39,300	27,700	nd	nd
05C-15X3-100-105	5	C	15	3	100–105	11.9	110.2	32,500	17,100	nd	nd
05C-16X1-63-68	5	C	16	1	63–68	9.8	116.4	10,500	12,700	nd	nd
05C-17X2-85-90	5	C	17	2	85–90	9.5	127.9	27,300	12,200	nd	nd
05C-17X5-90-95	5	C	17	5	90–95	8.6	132.4	28,000	13,500	nd	nd
05C-18X1-85-90	5	C	18	1	85–90	8.6	135.9	41,300	12,900	nd	nd
05C-18X3-81-86	5	C	18	3	81–86	11.5	138.9	67,700	11,300	nd	nd
05C-19X4-80-85	5	C	19	4	85–90	10.4	150.0	88,100	8,000	nd	nd
05C-20X4-80-85	5	C	20	4	85–90	9.7	158.0	74,600	4,900	nd	nd
05C-21X2-70-75	5	C	21	2	70–75	11.4	166.1	27,700	3,800	nd	nd
05C-22X3-80-85	5	C	22	3	85–90	12.9	177.3	30,700	4,000	nd	nd
05C-23X1-70-75	5	C	23	1	70–75	9.1	183.8	44,200	3,400	nd	nd
05C-24X2-70-75	5	C	24	2	70–75	12.0	194.9	23,100	5,600	nd	nd
05D-1H2-125-130	5	D	1	2	125–130	15.7	2.8	7,100	nd	nd	nd
05D-1H4-125-130	5	D	1	4	125–130	14.4	5.8	17,200	nd	nd	nd
05D-1H5-103-108	5	D	1	5	103–108	14.5	7.0	27,200	nd	nd	nd
05D-2H2-65-70	5	D	2	2	65–70	8.0	9.6	30,900	nd	nd	nd
05D-2H2-125-130	5	D	2	2	125–130	10.1	10.2	22,200	nd	nd	nd
05D-2H3-65-70	5	D	2	3	65–70	9.5	11.1	37,000	500	nd	nd
05D-2H4-65-70	5	D	2	4	65–70	10.8	12.6	29,600	7,400	nd	nd
05D-2H4-125-130	5	D	2	4	125–130	8.8	13.2	19,300	9,100	nd	nd
05D-2H5-65-70	5	D	2	5	65–70	9.4	14.1	26,500	16,100	nd	nd
05D-2H6-125-130	5	D	2	6	125–130	9.0	16.2	13,900	51,900	nd	nd
05D-3H1-135-140	5	D	3	1	135–140	7.7	18.3	9,200	12,700	nd	nd
05D-3H2-125-130	5	D	3	2	125–130	7.7	19.7	8,800	11,300	nd	nd
05D-3H3-125-130	5	D	3	3	125–130	8.4	21.3	7,200	6,800	nd	nd
05D-3H4-115-120	5	D	3	4	115–120	6.7	22.6	12,100	8,500	nd	nd
05D-3H5-55-60	5	D	3	5	55–60	6.7	23.5	12,900	7,900	nd	nd
05D-3H6-71-76	5	D	3	6	71–76	7.0	24.4	17,100	6,800	nd	nd
05D-4H2-125-130	5	D	4	2	125–130	8.0	29.3	15,700	17,400	nd	nd
05D-4H6-66-71	5	D	4	6	66–71	7.4	34.5	7,000	24,400	nd	nd
05D-6P-10-15	5	D	6	P	10–15	6.0	77.0	19,100	6,800	nd	nd
05D-7Y-46-47	5	D	7	Y	46–51	11.7	85.4	26,000	1,000	nd	nd
05D-7Y-66-67	5	D	7	Y	66–71	9.8	85.6	15,400	700	nd	nd
05D-11Y-65-70	5	D	11	Y	65–70	7.5	125.6	24,300	1,500	nd	nd
05D-12P-20-25	5	D	12	P	20–25	9.9	200.2	61,800	11,300	nd	nd
05D-12P-60-65	5	D	12	P	60–65	7.1	200.6	42,200	9,300	nd	nd

Table 7. Headspace gas (HS) composition for Site NGHP-01-05.—Continued

Sample	O_2	N_2+Ar	H_2S	C_1 (mL/L WS)	C_1 (mM PW)	CO_2 (mL/L WS)	CO_2 (mM PW)	C_1/CO_2
	(ppm-v)							
05C-1H1-105-110	183,800	735,900	nd	nd	nd	36,400	1.7	-
05C-2H1-105-110	175,900	726,500	nd	nd	nd	55,200	3.0	-
05C-2H3-105-110	178,700	739,000	nd	nd	nd	67,400	4.0	-
05C-2H7-15-20	181,800	739,700	nd	400	0.0	37,800	2.4	0.0
05C-3H1-105-110	182,400	741,500	nd	nd	nd	18,500	1.2	-
05C-3H3-105-110	165,800	740,700	nd	nd	nd	10,600	0.7	-
05C-3H5-105-110	163,100	751,900	nd	nd	nd	20,300	1.4	-
05C-4H2-95-100	136,400	733,500	nd	39,600	2.9	59,900	4.3	0.7
05C-4H4-95-100	106,600	728,900	nd	91,500	6.8	42,800	3.2	2.1
05C-4H6-95-100	81,400	751,400	nd	82,500	6.3	28,500	2.2	2.9
05C-5H2-95-100	141,500	750,200	nd	15,900	1.2	40,700	3.1	0.4
05C-5H4-95-100	148,600	744,200	nd	15,600	1.2	57,600	4.4	0.3
05C-5H6-95-100	133,000	750,800	nd	25,700	2.0	67,600	5.2	0.4
05C-6H3-95-100	140,900	717,000	nd	18,400	1.4	91,000	7.1	0.2
05C-6H5-105-110	143,200	721,600	nd	23,600	1.8	107,900	8.4	0.2
05C-7H2-95-100	127,600	761,600	nd	28,100	2.3	80,400	6.5	0.3
05C-7H5-105-110	152,500	747,400	nd	16,700	1.4	56,800	4.6	0.3
05C-8H2-95-100	120,100	746,000	nd	20,500	1.7	85,200	7.0	0.2
05C-8H5-105-110	134,300	755,400	nd	25,000	2.1	96,500	8.0	0.3
05C-9H2-95-100	166,800	735,000	nd	15,400	1.3	41,900	3.5	0.4
05C-9H5-105-110	168,700	739,600	nd	20,900	1.7	50,400	4.1	0.4
05C-10P-10-15-1	52,500	746,700	nd	30,700	2.5	67,600	5.6	0.5
05C-11X1-77-82	154,000	753,100	nd	28,300	2.3	71,500	5.9	0.4
05C-12P-15-20	180,300	722,200	nd	83,700	6.9	42,100	3.5	2.0
05C-12P-46-51	181,200	721,200	nd	21,900	1.8	48,900	4.0	0.5
05C-13X1-65-70	156,900	752,300	nd	28,100	2.4	45,500	3.8	0.6
05C-13X2-45-50	81,200	724,900	nd	51,800	4.4	19,100	1.6	2.7
05C-13X3-85-90	141,600	781,600	nd	28,700	2.4	27,600	2.4	1.0
05C-14X1-85-90	66,500	756,200	nd	13,300	1.2	31,300	2.8	0.4
05C-15X1-85-90	27,000	788,700	nd	31,700	2.9	44,900	4.1	0.7
05C-15X3-100-105	35,100	787,700	nd	28,200	2.5	53,600	4.8	0.5
05C-16X1-63-68	37,300	739,200	nd	28,200	2.5	23,200	2.0	1.2
05C-17X2-85-90	300	742,200	nd	28,200	2.5	63,200	5.6	0.4
05C-17X5-90-95	47,500	761,600	nd	35,900	3.2	74,500	6.6	0.5
05C-18X1-85-90	45,700	743,700	nd	34,400	3.0	109,900	9.7	0.3
05C-18X3-81-86	30,200	703,100	nd	19,700	1.8	117,700	10.7	0.2
05C-19X4-80-85	59,100	770,300	nd	16,300	1.5	178,800	16.3	0.1
05C-20X4-80-85	105,700	724,600	nd	10,900	1.0	167,700	15.3	0.1
05C-21X2-70-75	46,800	722,100	nd	6,600	0.6	48,900	4.6	0.1
05C-22X3-80-85	45,600	735,100	nd	5,700	0.5	44,300	4.2	0.1
05C-23X1-70-75	42,000	746,800	nd	8,400	0.8	108,700	10.1	0.1
05C-24X2-70-75	43,000	741,400	nd	9,100	0.9	37,500	3.6	0.2
05D-1H2-125-130	40,400	743,200	nd	nd	nd	7,100	0.4	-
05D-1H4-125-130	39,500	736,900	nd	nd	nd	20,400	1.2	-
05D-1H5-103-108	35,000	721,300	nd	nd	nd	31,900	1.9	-
05D-2H2-65-70	36,400	727,300	nd	nd	nd	90,700	5.6	-
05D-2H2-125-130	38,900	749,400	nd	nd	nd	47,100	3.0	-
05D-2H3-65-70	33,300	725,300	nd	1,200	0.1	85,800	5.5	0.0
05D-2H4-65-70	35,200	726,500	nd	14,100	0.9	56,700	3.7	0.3
05D-2H4-125-130	36,700	719,000	nd	23,300	1.5	49,900	3.2	0.5
05D-2H5-65-70	33,800	717400	nd	37,900	2.5	62,300	4.1	0.6
05D-2H6-125-130	147,700	712,500	nd	129,800	8.7	34,800	2.3	3.7
05D-3H1-135-140	35,900	716,600	nd	39,300	2.7	28,500	1.9	1.4
05D-3H2-125-130	36,500	728,100	nd	35,000	2.4	27,100	1.9	1.3
05D-3H3-125-130	40,500	734,300	nd	18,700	1.3	19,700	1.4	0.9
05D-3H4-115-120	39,000	737,600	nd	31,300	2.2	44,600	3.1	0.7
05D-3H5-55-60	36,800	724,800	nd	29,300	2.0	47,800	3.3	0.6
05D-3H6-71-76	35,100	738,400	nd	23,800	1.7	60,000	4.2	0.4
05D-4H2-125-130	31,500	749,100	nd	51,200	3.7	46,100	3.3	1.1
05D-4H6-66-71	36,100	749,000	nd	79,300	5.8	22,700	1.7	3.5
05D-6P-10-15	158,200	758,300	nd	28,900	2.3	81,000	6.6	0.4
05D-7Y-46-47	37,400	763,100	nd	1,600	0.1	44,000	3.8	0.0
05D-7Y-66-67	44,700	751,100	nd	1,500	0.1	34,100	2.9	0.0
05D-11Y-65-70	124,800	767,700	nd	4,900	0.4	77,900	6.8	0.1
05D-12P-20-25	127,600	772,900	nd	24,600	2.3	134,700	12.7	0.2
05D-12P-60-65	135,900	765,800	nd	32,000	2.9	144,900	13.3	0.2

Notes: nd = not detected. WS = Wet sediment. PW = porewater. Approximate detection limits are about 15 ppmv for methane, 30 ppmv for ethane, 50 ppmv for propane, and 20 ppmv for hydrogen sulfide.

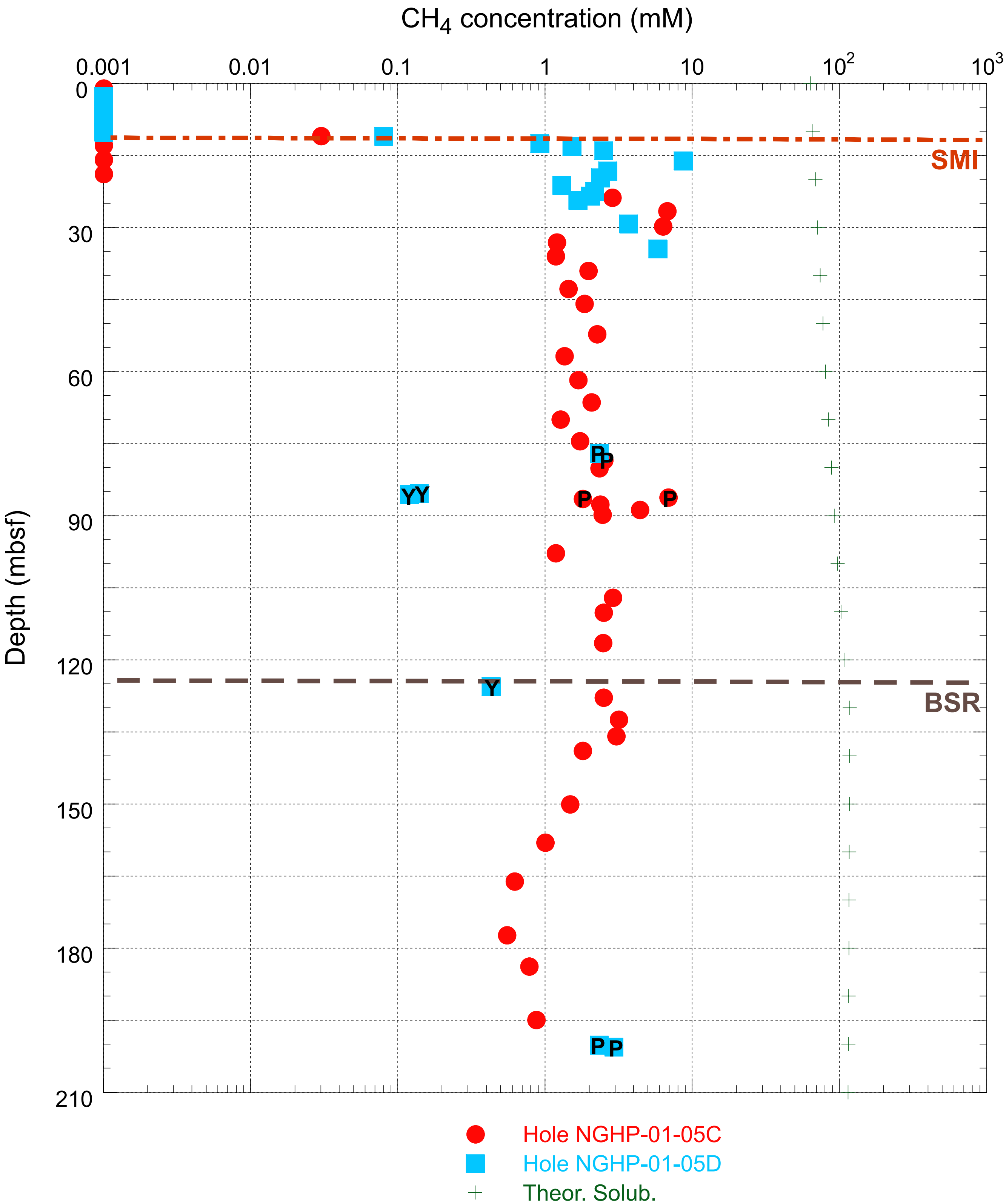

Figure 14. Plot of headspace methane gas concentration (mM) with depth for Site NGHP-01-05, Holes C and D. Note the two apparent peaks in methane just above 15 mbsf and 85 mbsf. Values less than 0.003 mM are below instrument detection limits, but plotted for reference. Text inside a symbol denotes special coring tool (E, HRC; P, PCS; Y, FPC). Theoretical solubility of methane calculated using the Duan and others (1992) and Xu (2002, 2004) methodologies. Hole NGHP-01-05D was not sampled continuously, thus resulting in the random data collection intervals at depth. [mbsf, meters below sea floor]

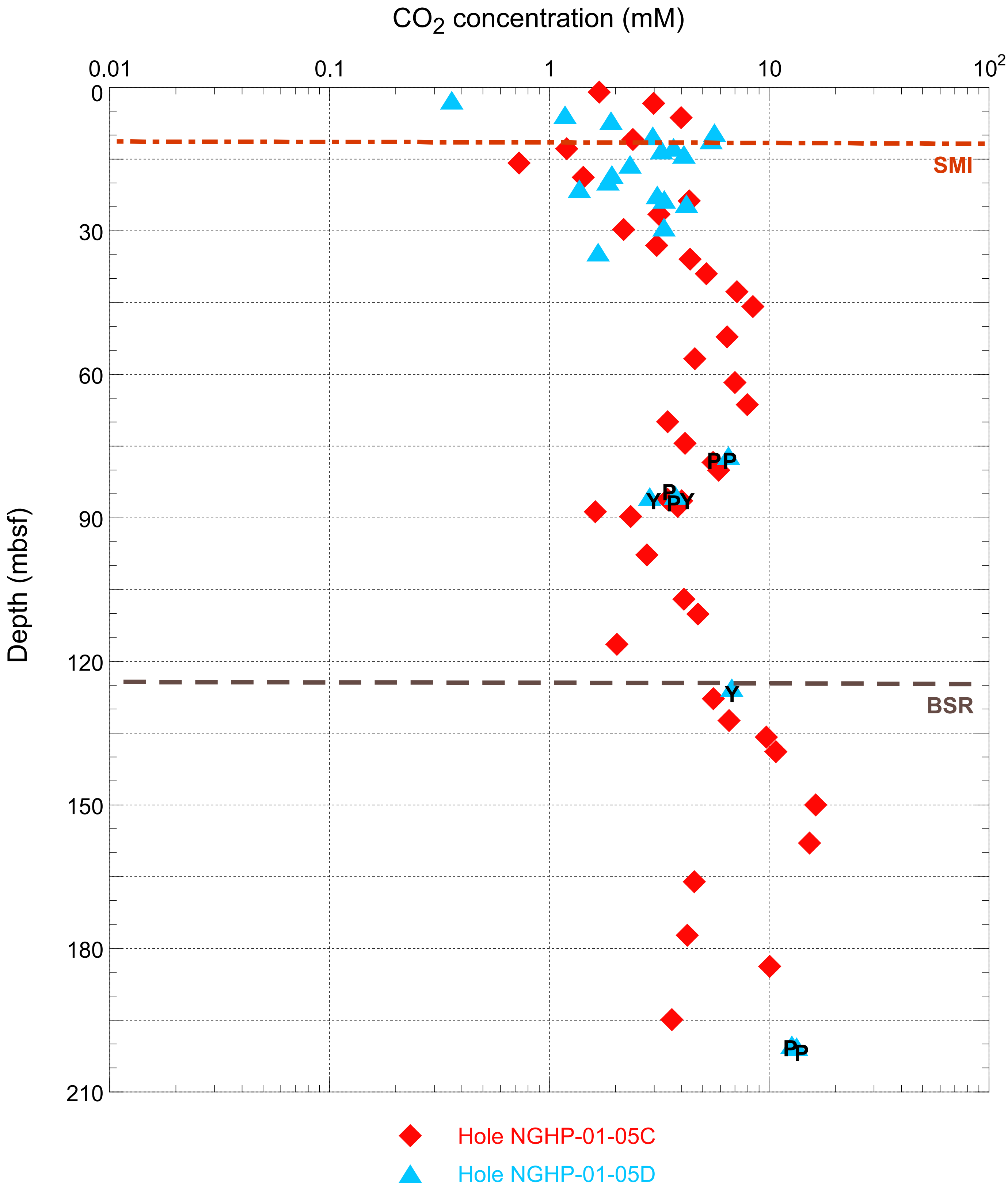

Figure 15. Plot of headspace carbon dioxide gas concentration (mM) with depth for Site NGHP-01-05, Holes C and D. Note the apparent peak in concentration below 140 mbsf. Text inside a symbol denotes special coring tool (E, HRC; P, PCS; Y, FPC). Hole NGHP-01-05D was not sampled continuously, thus resulting in the random data collection intervals at depth, and as such could not confirm the elevated concentration at depth. [mbsf, meters below sea floor]

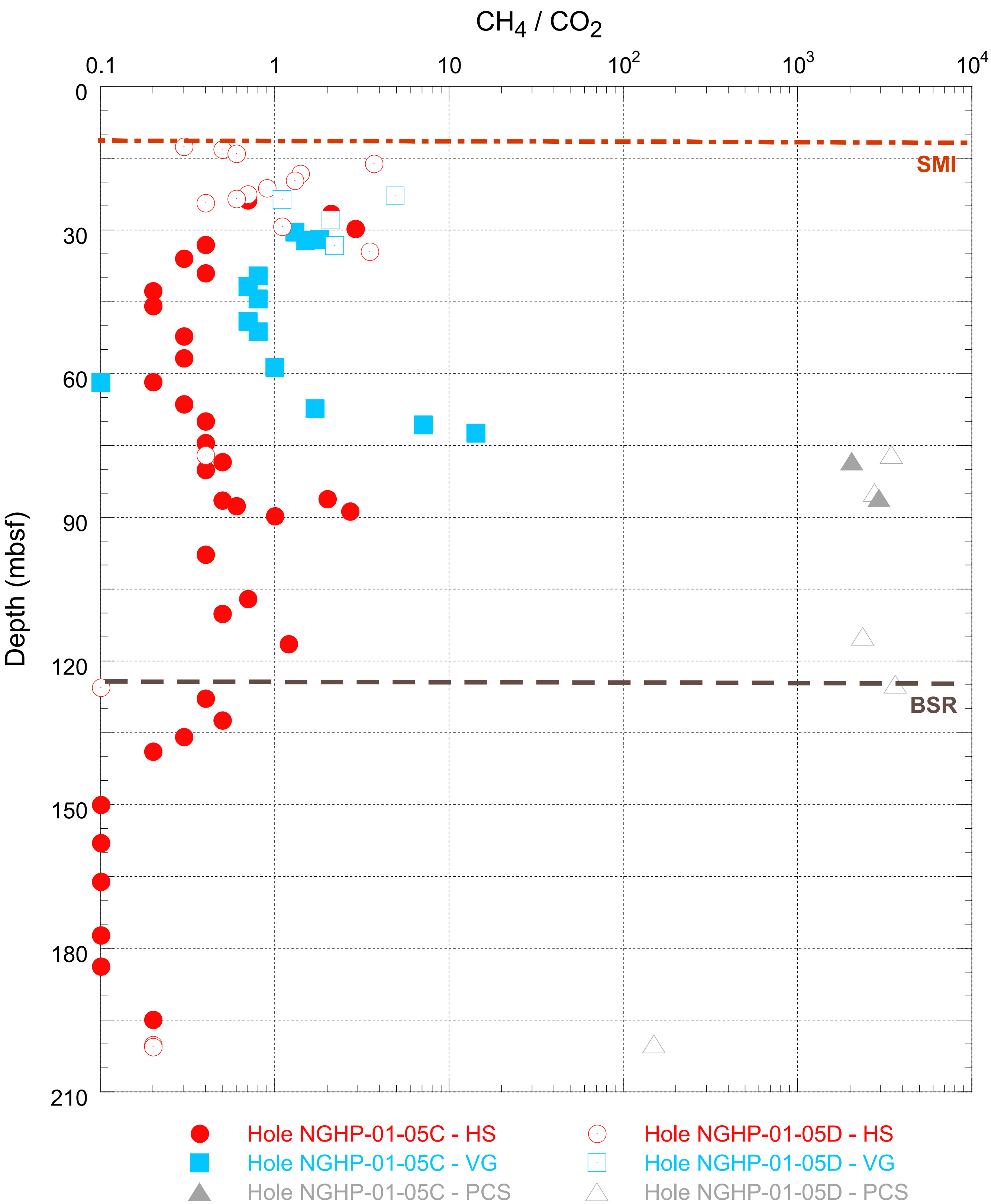

Figure 16. Plot of methane to carbon dioxide gas ratio with depth for headspace, void gas, and PCS gas for Site NGHP-01-05, Holes C and D. Note the spikes in methane concentration are a likely proxy of gas-hydrate occurrence. Hole NGHP-01-05D was not sampled continuously and void gas samples are rarely obtained after XCB coring begins (~80 mbsf at this site), thus resulting in the random data collection intervals at depth. [HS, headspace; VG, void gas; PCS, Pressure Core Sampler; mbsf, meters below sea floor]

Table 8. Void gas (vac) composition for Site NGHP-01-05.

Sample	Site	Hole	Core	Section	Interval (cm)	Sample depth (mbsf)	CO_2	C_1	C_2	C_3	O_2	N_2+Ar	H_2S	C_1/CO_2
							(ppmv) normalized to nitrogen+argon							
5C-3H3-136	5	C	3	3	136	16.16	1,100	nd	nd	nd	48,900	950,000	nd	-
5C-4H7-14	5	C	4	7	14	30.44	6,000	809,400	nd	nd	4,200	180,400	nd	130
5C-5H1-115	5	C	5	1	115	31.95	5,400	969,200	nd	nd	2,400	22,900	nd	180
5C-5H1-137	5	C	5	1	137	32.17	6,400	959,900	nd	nd	4,600	29,200	nd	150
5C-5H4-7	5	C	5	4	7	35.22	1,400	3,600	nd	nd	208,000	787,100	nd	0
5C-5H7-1	5	C	5	7	1	39.58	6,100	488,900	nd	nd	109,200	395,800	nd	80
5C-6H2-116	5	C	6	2	116	41.8	14,800	964,900	nd	nd	2,800	17,500	nd	70
5C-6H4-110	5	C	6	4	110	44.41	13,000	977,800	nd	nd	1,900	7,300	nd	80
5C-6H7-131	5	C	6	7	131	49.1	13,300	973,600	nd	nd	4,500	8,600	nd	70
5C-7H2-1	5	C	7	2	1	51.23	12,700	979,800	nd	nd	1,600	5,800	nd	80
5C-7H7-1	5	C	7	7	1	58.68	10,100	984,600	nd	nd	1,900	3,400	nd	100
5C-8H2-107	5	C	8	2	107	61.87	62,300	896,000	nd	nd	15,400	26,400	nd	10
5C-8H7-1	5	C	8	7	1	67.32	1,000	166,400	nd	nd	75,200	757,400	nd	170
5C-9H3-23	5	C	9	3	23	70.71	1,400	995,700	nd	nd	1,000	1,900	nd	710
5C-9H4-51	5	C	9	4	51	72.42	700	996,200	nd	nd	1,200	1,900	nd	1,420
5C-9H6-_	5	C	9	6	NR	NR	5,300	991,100	nd	nd	1,400	2,200	nd	190
5D-3H5-0	5	D	3	5	0	22.9	2,000	985,400	nd	nd	4,700	7,900	nd	490
5D-3H6-0	5	D	3	6	0	23.65	8,500	972,700	nd	nd	6,000	12,800	nd	110
5D-4H2-115	5	D	4	2	115	27.9	4,700	982,400	nd	nd	4,500	8,500	nd	210
5D-4H5-85	5	D	4	5	85	33.25	4,500	992,200	nd	nd	800	2,500	nd	220

Notes: nd = not detected. nr = not recorded. Approximate detection limits are about 15 ppmv for methane, 30 ppmv for ethane, 50 ppmv for propane, and 20 ppmv for hydrogen sulfide.

Table 9. Pressure Core Sampler (PCS) gas composition for Site NGHP-01-05.

Sample	Site	Hole	Core	Section	Sample depth (mbsf)	Time	Gas vol. (ml)	CO_2	C_1	C_2	C_3	O_2	N_2+Ar	H_2S	C_1/CO_2	C_1/C_2
								(ppmv) normalized to nitrogen+argon								
05C-10P-t1	5	C	10	P	78.3	1	-	300	987,200	10	nd	4,200	8,200	nd	3,300	98,700
05C-10P-t2	5	C	10	P	78.3	2	-	500	404,500	nd	nd	130,600	464,400	nd	800	-
05C-12P-t1	5	C	12	P	86	1	-	200	963,100	10	nd	4,300	32,400	nd	4,800	96,300
05C-12P-t2	5	C	12	P	86	2	-	300	962,700	10	nd	2,700	34,200	nd	3,200	96,300
05C-12P-t3	5	C	12	P	86	3	-	400	813,900	10	nd	6,200	179,500	nd	2,000	81,400
05D-6P-t1	5	D	6	P	76.9	1	-	200	991,500	40	nd	3,000	5,200	nd	5,000	24,800
05D-6P-t2	5	D	6	P	76.9	2	-	200	995,600	40	nd	1,700	2,500	nd	5,000	24,900
05D-6P-t3	5	D	6	P	76.9	3	-	200	995,400	50	nd	1,800	2,600	nd	5,000	19,900
05D-6P-t4	5	D	6	P	76.9	4	-	300	994,400	50	nd	2,000	3,300	nd	3,300	19,900
05D-6P-t5	5	D	6	P	76.9	5	-	400	987,500	40	nd	3,900	8,200	nd	2,500	24,700
05D-6P-t6	5	D	6	P	76.9	6	-	1,100	987,200	30	nd	2,600	9,100	nd	900	32,900
05D-7Y-t1	5	D	7	Y	84.9	1	-	200	995,800	40	nd	1,700	2,100	nd	5,000	24,900
05D-7Y-t2	5	D	7	Y	84.9	2	-	300	997,100	40	nd	1,200	1,400	nd	3,300	24,900
05D-7Y-t3	5	D	7	Y	84.9	3	-	300	996,900	40	nd	1,300	1,400	nd	3,300	24,900
05D-7Y-t4	5	D	7	Y	84.9	4	-	300	997,200	40	nd	1,200	1,200	nd	3,300	24,900
05D-7Y-t5	5	D	7	Y	84.9	5	-	300	997,200	40	nd	1,100	1,400	nd	3,300	24,900
05D-7Y-t6	5	D	7	Y	84.9	6	-	1,000	976,100	20	nd	7,200	15,700	nd	1,000	48,800
05D-7Y-t7	5	D	7	Y	84.9	7	-	800	883,400	30	nd	24,800	91,000	nd	1,100	29,400
05D-7Y-t8	5	D	7	Y	84.9	8	-	300	897,500	20	nd	20,800	81,400	nd	3,000	44,900
05D-10E-t1	5	D	10	E	114.9	1	-	300	976,900	40	nd	7,500	15,300	nd	3,300	24,400
05D-10E-t2	5	D	10	E	114.9	2	-	500	976,000	40	nd	6,100	17,300	nd	2,000	24,400
05D-10E-t3	5	D	10	E	114.9	3	-	800	979,000	40	nd	4,200	15,900	nd	1,200	24,500
05D-11Y-t1	5	D	11	Y	124.9	1	-	300	956,500	20	nd	9,900	33,200	nd	3,200	47,800
05D-11Y-t1	5	D	11	Y	124.9	1	-	300	954,900	20	nd	10,400	34,500	nd	3,200	47,700
05D-11Y-t2	5	D	11	Y	124.9	2	-	200	965,300	30	nd	6,900	27,500	nd	4,800	32,200
05D-11Y-t2	5	D	11	Y	124.9	2	-	200	962,700	20	nd	7,800	29,200	nd	4,800	48,100
05D-11Y-t3	5	D	11	Y	124.9	3	-	300	983,300	20	nd	4,100	12,200	nd	3,300	49,200
05D-11Y-t3	5	D	11	Y	124.9	3	-	300	983,300	nd	nd	4,200	12,300	nd	3,300	-
05D-12P-t1	5	D	12	P	200	1	-	5,100	768,400	20	nd	11,500	215,000	nd	200	38,400
05D-12P-t2	5	D	12	P	200	2	-	9,600	753,200	20	nd	10,700	226,500	nd	100	37,700

Notes: nd = not detected. Approximate detection limits are about 15 ppmv for methane, 30 ppmv for ethane, 50 ppmv for propane, and 20 ppmv for hydrogen sulfide.

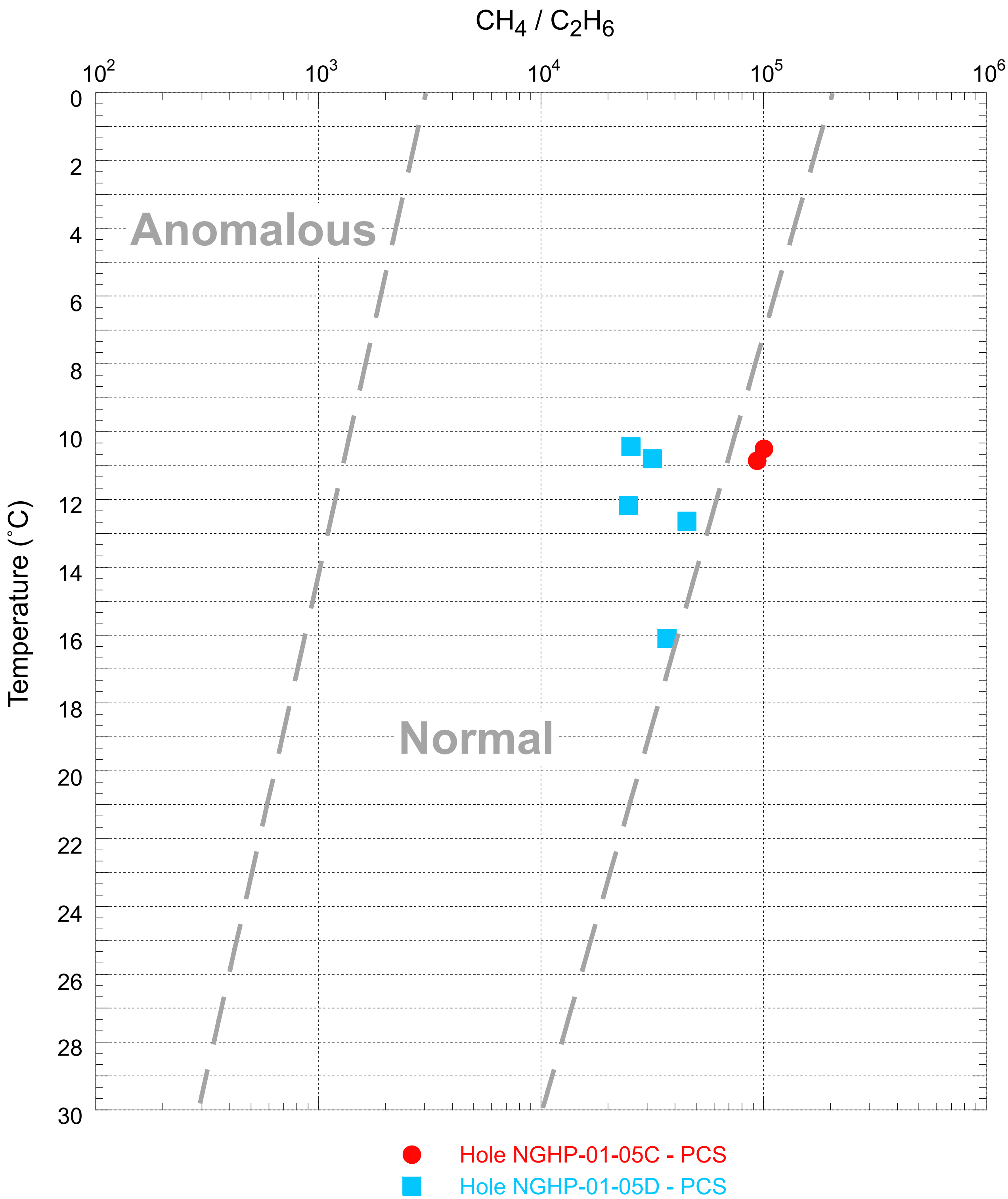

Figure 17. Plot of PCS methane to ethane gas ratio with depth for Site NGHP-01-05, Holes C and D. Ethane levels were below detection limits for all headspace and free gas samples (tables 7 and 8). Note that the hydrocarbon gas occurrences fall into the typical range. [PCS, pressure sensor core]

Table 10. List of microbiological samples taken for Site NGHP-01-05.

Core, section, interval (cm)	Sample code	Depth (mbsf)	Volume (cc)	Comments
NGHP-01-05C				
2H-4,120-125	CEL	6.7	5	
3H-4,115-120	CEL	17.45	5	
4H-4,80-85	CEL	24	5	
5H-4,80-85	CEL	33.55	5	
6H-4,118-123	CEL	43.11	5	
7H-4,120-125	CEL	55.47	5	
8H-4,120-125	CEL	65.05	5	
9H-4,120-125	CEL	73.11	5	
11X-1,77-82	CEL	80.07	5	
13X-4,111-116	CEL	91.51	5	
14X-1,85-90	CEL	97.75	5	
15X-2,120-125	CEL	108.9	5	
16X-1,63-68	CEL	116.43	187	
17X-4,120-125	CEL	131.2	5	
18X-3,81-86	CEL	138.91	5	
19X-4,80-85	CEL	150	5	
20X-3,70-75	CEL	158	5	
21X-2,70-75	CEL	166.1	5	
22X-3,80-85	CEL	177.3	5	
23X-1,70-75	CEL	183.8	5	
24X-2,70-75	CEL	194.9	5	
2H-4,130-140	JAN	8.05	374	
3H-4,130-140	JAN	17.5	374	
4H-4,90-100	JAN	26.6	374	
5H-4,84-94	JAN	35.95	374	
6H-4,128-138	JAN	44.49	374	
7H-4,130-140	JAN	55.62	374	
8H-4,130-140	JAN	65.2	374	
9H-4,130-140	JAN	73.21	374	
13X-4,121-131	JAN	91.61	374	
15X-2,130-140	JAN	109	374	
17X-4,130-140	JAN	131.3	374	
18X-3,91-101	JAN	139.01	374	
19X-4,100-110	JAN	150.2	374	
20X-3,90-100	JAN	158.2	374	
21X-2,90-100	JAN	166.3	374	
22X-3,90-100	JAN	177.4	374	
23X-1,90-100	JAN	184	374	
24X-2,90-100	JAN	195.1	374	
1H-2,130-140	JAN	2.8	374	
1H-4,130-140	JAN	5.8	374	
1H-5,108-118	JAN	7.08	374	
2H-2,130-140	JAN	10.2	374	
2H-4,130-140	JAN	13.2	374	
2H-6,130-140	JAN	16.2	374	
3H-2,130-140	JAN	19.7	374	
3H-4,120-130	JAN	22.6	374	
3H-6,76-86	JAN	24.41	374	
6P-1,26-30	JAN	77.16	150	
6P-1,50-55	JAN	77.4	187	
7Y-1,44-46	JAN	85.34	10	Only taken from working half
7Y-1,63-66	JAN	85.53	10	Only taken from working half
11Y-1,20-23	JAN	125.1	56	Only taken from working half
1H-1,120-130	JUD	1.2	374	
2H-1,120-130	JUD	3.4	374	
2H-3,120-130	JUD	6.4	374	
2H-5,120-130	JUD	9.4	374	
2H-7,30-40	JUD	11	374	
3H-1,120-130	JUD	13	374	
3H-3,120-130	JUD	16	374	
NGHP-01-05C—Continued				
3H-5,120-130	JUD	18.9	374	
4H-2,120-130	JUD	23.75	374	
4H-4,120-130	JUD	26.7	374	
4H-6,120-130	JUD	29.75	374	
5H-2,120-130	JUD	32.17	374	
5H-4,114-124	JUD	36.09	374	
5H-6,118-128	JUD	39.07	374	
6H-3,120-130	JUD	42.76	374	
6H-5,120-130	JUD	44.69	374	
7H-2,120-130	JUD	52.52	374	
7H-5,120-130	JUD	57.02	374	
8H-2,120-130	JUD	62.1	374	
8H-5,120-130	JUD	66.6	374	
9H-2,78-88	JUD	70.18	374	
9H-5,120-130	JUD	74.61	374	
13X-1,90-100	JUD	87.9	374	
13X-3,110-120	JUD	90	374	
14X-1,110-120	JUD	98	374	
15X-1,110-120	JUD	107.3	374	
15X-3,110-120	JUD	110.3	374	
16X-1,88-98	JUD	116.68	374	
17X-2,110-120	JUD	128.1	374	
17X-5,105-115	JUD	132.55	374	
18X-1,110-120	JUD	136.2	374	
19X-4,120-130	JUD	150.4	374	
20X-3,110-120	JUD	158.4	374	
21X-2,110-120	JUD	166.5	374	
22X-3,110-120	JUD	177.6	374	
23X-1,110-120	JUD	184.2	374	
24X-2,110-120	JUD	195.3	374	
2H-4,125-130	SPH	8	187	
3H-4,120-130	SPH	17.45	374	
4H-4,85-90	SPH	26.6	187	
5H-4,79-84	SPH	35.95	187	
6H-4,123-128	SPH	43.21	187	
7H-4,125-130	SPH	55.52	187	
8H-4,125-130	SPH	65.1	187	
9H-4,125-130	SPH	73.16	187	
13X-4,116-121	SPH	91.56	187	
15X-2,125-130	SPH	108.95	187	
17X-4,125-130	SPH	131.25	187	
18X-3,86-91	SPH	138.96	187	
19X-4,85-90	SPH	150.05	187	
20X-3,75-80	SPH	158.05	187	
21X-2,75-80	SPH	166.15	187	
22X-3,85-90	SPH	177.35	187	
23X-1,75-80	SPH	183.85	187	
24X-2,75-80	SPH	194.95	187	
NGHP-01-05D				
1H-2,130-140	JAN	2.8	374	
1H-4,130-140	JAN	5.8	374	
1H-5,108-118	JAN	7.08	374	
2H-2,130-140	JAN	10.2	374	
2H-4,130-140	JAN	13.2	374	
2H-6,130-140	JAN	16.2	374	
3H-2,130-140	JAN	19.7	374	
3H-4,120-130	JAN	22.6	374	
3H-6,76-86	JAN	24.41	374	
6P-1,26-30	JAN	77.16	150	
6P-1,50-55	JAN	77.4	187	
7Y-1,44-46	JAN	85.34	10	
7Y-1,63-66	JAN	85.53	10	
11Y-1,20-23	JAN	125.1	56	

With the exception of the thermal conductivity system, all instruments in the physical properties laboratory were set up specifically for NGHP Expedition 01. This was the first site at which a full suite of physical properties were measured during this cruise. The MSCL and thermal conductivity systems were previously used during Leg 1. The testing and sampling strategy optimized the time required to perform measurements and subsample for MAD tests.

Infrared Imaging (IR)

Environmental Conditions

Catwalk environment was monitored during the entire drilling operation at Site NGHP-01-05. Temperature on the catwalk remained relatively constant at 30.8 to 31.8° ± 3 °C during the drilling operation, as shown in figure 18. Relative humidity of 80 percent was typical (fig. 18), which is consistent with a marine environment setting in the Indian Ocean. No adverse environmental conditions such as high winds or thunderstorms persisted during drilling operations at this site.

Infrared Images

All cores were systematically scanned upon arrival on the catwalk using the track-mounted IR camera described in the “Physical properties” section of the “Methods” chapter. IR anomalies, commonly referred to as “cold spots,” indicate gas-hydrate dissociation during core recovery, which subsequently provided guidance to catwalk sampling. Summaries of all scans are provided in tables 11, 12, 13, 14, and 15, and bit maps of the scans of all cores are available in the supplemental data files section of this report. Temperature arrays in the format of text files or comma separated value (CSV) files were exported from the IR camera software and then concatenated for each core. The arrays were then further concatenated for all cores available in a given borehole and down-core temperatures were averaged for each pixel row in the array, excluding pixels ~1 cm from the edge of the image and 2 cm along the midline of the image. Exclusion of these particular sets of pixels minimizes the effects caused by major thermal artifacts in the images. This processing enables us to measure the average amplitude of the cold anomalies and separate warm anomalies due to voids from the background temperature field.

Infrared track imaging at Hole NGHP-01-05C consisted of 24 runs. The complete set of IR images collected for Hole NGHP-01-05C is presented in figure 19 along with the corresponding down-core temperatures. The median core temperature ranged from a high of 25.5 °C for Core NGHP-01-05C-16X (115.8 mbsf) to a low of 19.2 °C for Core NGHP-01-05C-14X (96.9 mbsf). The lowest temperatures measured (excluding the upper most two sections) were 20.1 °C and 19.2 °C, for Core NGHP-01-05C-13X (87.0 mbsf) and NGHP-01-05C-14X (96.9 mbsf), respectively. IR anomalies occurred only in Cores NGHP-01-05C-13X and NGHP-01-05C-14X (fig. 19). These were systematically sampled for interstitial pore water following the completion of IR track imaging.

Four infrared track images were collected from Hole NGHP-01-05D. Complete down-core temperature and the corresponding concatenated IR images are provided in figure 20. The maximum temperature (29.9 °C) was recorded in Core NGHP-01-05D-02H (7.4 mbsf) and the coldest temperature was identified in Core NGHP-01-05D-01H, approximately 9 °C less. No IR anomalies were observed in the four cores collected from Hole NGHP-01-05D.

IR images of the ends of core sections were acquired with a hand-held IR camera. Figure 21 shows a typical section-end IR image from Section NGHP-01-05C-24X-4 (top) with a reference temperature scale. A total of sixteen images were collected from Hole NGHP-01-05C; no core end images were collected from Site NGHP-01-05D. Images from Hole NGHP-01-05C were collected sequentially down core as the core was processed on the catwalk and were used to illustrate the temperature changes in the core over space and time. Analysis of the core end images resulted in a minimum temperature of 19 °C (Section NGHP-01-05C-14X-5, bottom) which corresponded to one of the two cores that contained IR anomalies.

In addition to the IR core end images, a similar technique was used to identify cold anomalies in the sediment selected for interstitial water samples. For example, Cores NGHP-01-05C-13 and NGHP-01-05C-14 were identified as containing IR anomalies while on the catwalk with the IR tracking system. Core sections were removed for interstitial water samples. After extracting the sediment from the liner, IR imaging with the hand-held camera was used to identify gas hydrate or “cold spots” in the sediment as well as to provide guidance for background sediment sampling. IR images of these extracted sediments were also collected and processed to document temperature variations.

Core-End Temperature Readings

Core-end temperature readings were taken on all cores immediately following the IR track imaging. Typically four temperature probes were inserted approximately 8 cm into the end of each core and allowed to remain there until the core was completely processed and removed from the catwalk. As an example, a summary of two temperature thermocouple results representing the edge closest to the core liner (blue) and the core center (red) are shown in figure 22. Temperatures ranged from 10 to 24 °C, with the coldest measurement occurring in Core NGHP-01-05C-01H. Obvious from figure 22 is the general warming of the core center (red) as a function of subbottom depth, which is to be expected. Similar results were observed in Hole NGHP-01-05D.

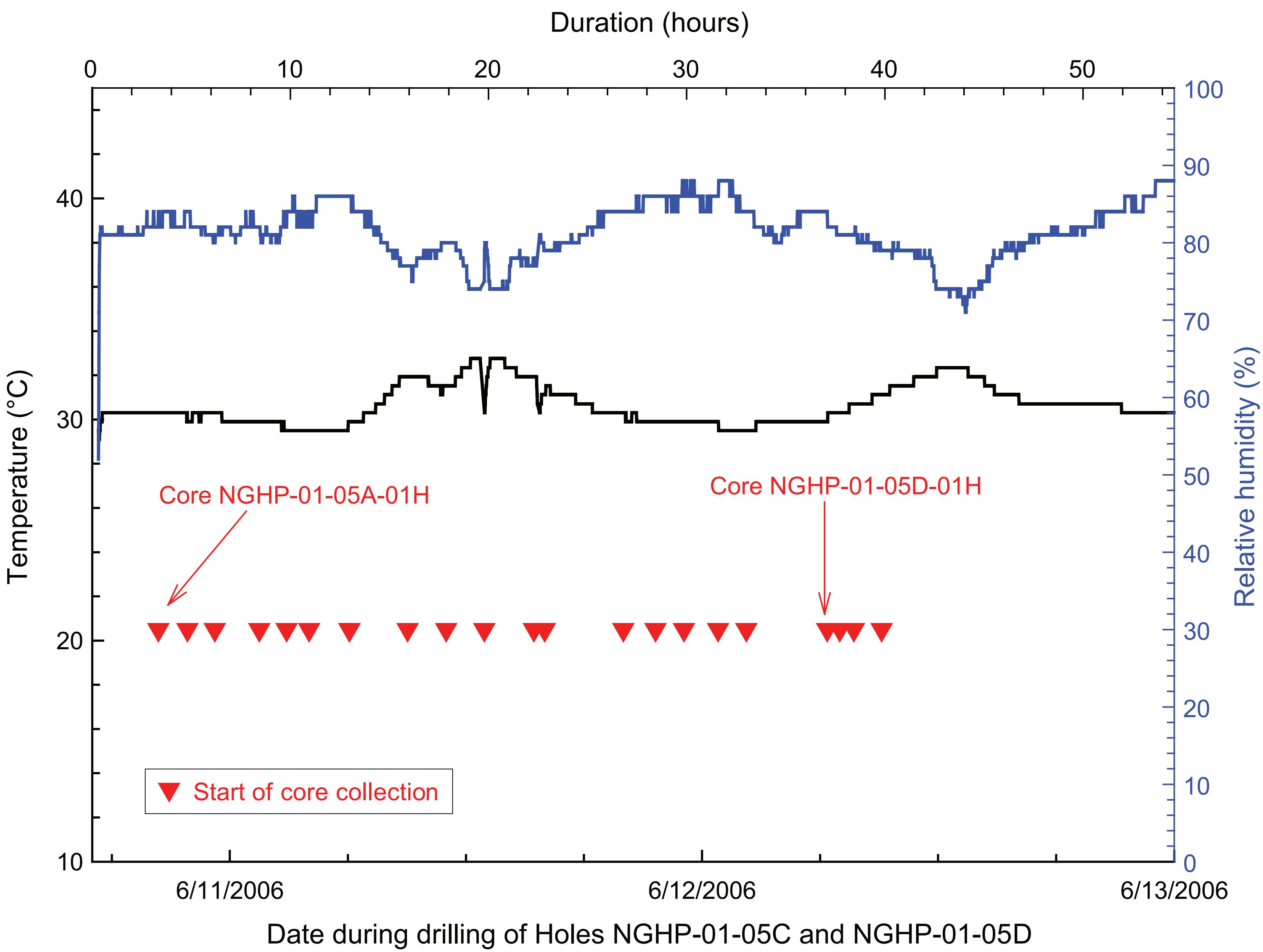

Figure 18. Catwalk temperature and humidity during drilling operations at Site NGHP-01-05.

Table 11. List of all infrared image files collected for Hole NGHP-01-05C.

Core	Imaging length (cm)	First run	Date	Start time	Temperature (start/end) (°C)	File ID	Screen image saved	Comments*
1H	210	x	6/10	19:30	30.33/30.33	NGHP-05-C-1	Yes	15–25 °C
2H	910	x	6/10	20:22	30.33/30.33	NGHP-05-C-2	Yes	15–30 °C
3H	970	x	6/10	21:51	30.33/30.33	NGHP-05-C-3	Yes	15–30 °C
4H	970	x	6/10	23:14	30.33/30.33	NGHP-05-C-4	Yes	15–30 °C
5H	970	x	6/10	0:12	30.33/30.33	NGHP-05-C-5	Yes	15–30 °C
6H	970	x	6/11	1:30	29.94/29.94	NGHP-05-C-6	Yes	15–30 °C
7H	970	x	6/11	2:53	29.94/29.94	NGHP-05-C-7	Yes	15–30 °C
8H	900	x	6/11	4:02	29.56/29.56	NGHP-05-C-8	Yes	15–30 °C
9H	970	x	6/11	6:05	29.56/29.56	NGHP-05-C-9	Yes	15–30 °C
10P								Not imaged
11X	110	x	6/11	9:02	31.5/31.5	NGHP-05-C-10	Yes	15–25 °C
12P								Not imaged
13X	490	x	6/11	11:00	31.1/31.1	NGHP-05-C-11	Yes	15–25 °C
14X	210	x	6/11	6:05	31.7/31.7	NGHP-05-C-12	Yes	15–25 °C
15X	530	x	6/11	12:56	32.2/32.2	NGHP-05-C-13	Yes	15–25 °C
16X	130	x	6/11	15:27	31.7/31.7	NGHP-05-C-14	Yes	15–25 °C; reprocessed @ 15–30 °C
17X	740	x	6/11	16:00	31.7/31.7	NGHP-05-C-15	Yes	15–30 °C
18X	425	x	6/11	16:00	31.1/31.1	NGHP-05-C-16	Yes	15–30 °C
19X								Not imaged—camera malfunction
20X	530	x	6/11	20:00	30.3/30.3	NGHP-05-C-20		15–30 °C
21X	430	x	6/11	21:38	29.9/29.9	NGHP-05-C-21		15–30 °C
22X	540	x	6/11	23:05	29.9/29.9	NGHP-05-C-22		15–30 °C
23X	340	x	6/12	0:49	29.5/29.9	NGHP-05-C-23		15–30 °C
24X	620	x	6/12	2:15	29.5/29.5	NGHP-05-C-24		15–30 °C

Table 12. List of all infrared section-end image files (catwalk) collected from Hole NGHP-01-05C.

Core	Section	Top	Date	Time	Image #	Comments
3	5	x	6/10	22:23	G0610-05	IMG file
3	5	x	6/10	22:23	G0610-06	Core end, BMP
4	5	x	6/10	23:33	G0610-07	IMG file
4	5	x	6/10	23:33	G0610-08	Core end, BMP
5	5	x	6/11	0:43	G0611-01	IMG file
5	5	x	6/11	0:43	G0611-02	Core end, BMP
7	5	x	6/11	3:17	G0611-03	IMG file
7	5	x	6/11	3:17	G0611-04	Core end, BMP
8	5	x	6/11	4:28	G0611-05	IMG file
8	5	x	6/11	4:28	G0611-06	Core end, BMP
9	5	x	6/11	6:43	G0611-07	IMG file
9	5	x	6/11	6:43	G0611-08	Core end, BMP
13	2	x	6/11	11:11	G0611-11	IMG file
13	2	x	6/11	11:11	G0611-12	Sediment, BMP
14	2	x	6/11	12:07	G0611-13	IMG file
14	2	x	6/11	12:07	G0611-14	Sediment, BMP
14	2	x	6/11	12:08	G0611-15	IMG file
14	2	x	6/11	12:08	G0611-16	Sediment, BMP
14	5	x	6/11	12:12	G0611-17	IMG file
14	5	x	6/11	12:12	G0611-18	Core end, BMP
16	4	x	6/11	13:20	G0611-19	IMG file
16	4	x	6/11	13:20	G0611-20	Core end, BMP
17	5	x	6/11	16:00	G0611-21	IMG file
17	5	x	6/11	16:00	G0611-22	Core end, BMP
18	2	x	6/11	17:00	G0611-23	IMG file
18	2	x	6/11	17:00	G0611-24	Core end, BMP
19	5	x	6/11	18:00	G0611-25	IMG file
19	5	x	6/11	18:00	G0611-26	Core end, BMP
20	4	x	6/11	20:23	G0611-27	IMG file
20	4	x	6/11	20:23	G0611-28	Core end, BMP
23	2	x	6/12	0:05	G0612-1	IMG file
23	2	x	6/12	0:05	G0612-2	Core end, BMP
24	4	x	6/12	2:35	G0612-7	IMG file
24	4	x	6/12	2:35	G0612-8	Core end, BMP

Table 13. List of all infrared image files collected from Hole NGHP-01-05D.

Core	Imaging length (cm)	First run	Date	Start time	Temperature (start/end) (°C)	File ID	Screen image saved	Comments*
1H	720	x	6/12	6:22	29.9/29.9	NGHP_05D_1	Yes	15–25 °C
2H	960	x	6/12	7:00	30.3/30.3	NGHP_05D_2	Yes	15–30 °C
3H	970	x	6/12	7:43	30.3/30.3	NGHP_05D_3	Yes	15–30 °C
4H	970	x	6/12	9:08	30.7/31.1	NGHP_05D_4	Yes	15–30 °C

*Temperature range for images displayed during core collection.

Table 14. List of all section-end temperature measurements collected from cores stored in core rack from Hole NGHP-01-05C.

Core	Section	Top	Bottom	Date	In time	Out time	Temperature probe #	Comments
1H	end		x	6/10	6:22	6:27	1,2,3,4	
2H	end		x	6/10	7:02	7:11	1,2,3,4	
3H	end		x	6/10	7:45	7:52	1,2,3,4	
4H	end		x	6/10	9:10	9:23	1,2,3,4	
5H	end		x	6/11	0:12	12:39	1,2,3,4	
6H	end		x	6/11	1:36	2:06	1,2,3,4	
7H	end		x	6/11	2:56	3:10	1,2,3,4	
8H	end		x	6/11	4:08	4:24	1,2,3,4	
9H	end		x	6/11	6:13	6:55	1,2,3,4	
10H							not measured	
11H							not measured	
12H							not measured	
13X	end		x	6/11	11:13	11:20	1,2,3,4	
14X	end		x	6/11	12:04	12:20	1,2,3,4	
15X	end		x	6/11	12:58	13:24	1,2,3,4	
16X	end		x	6/11	15:08	15:14	1,2,3,4	
17X	end		x	6/11	15:58	16:16	1,2,3,4	
18X	end		x	6/11	16:51	17:03	1,2,3,4	
19X	end		x	6/11	17:49	17:58	1,2,3,4	
20X	end		x	6/11	20:11	20:30	1,2,3,4	
21X	end		x	6/11	21:40	21:45	1,2,3,4	
22X	end		x	6/11	23:06	23:12	1,2,3,4	
23X	end		x	6/12	0:49	0:56	1,2,3,4	
24X	end		x	6/12	2:08	2:37	1,2,3,4	

Table 15. List of all section-end temperature measurements collected from cores stored in core rack from Hole NGHP-01-05D.

Core	Section	Top	Bottom	Date	In time	Out time	Temperature probe #	Comments
01H	end		x	6/12	6:22	6:27	1,2,3,4	
02H	end		x	6/12	7:02	7:11	1,2,3,4	
03H	end		x	6/12	7:45	7:52	1,2,3,4	
04H	end		x	6/12	9:10	9:23	1,2,3,4	

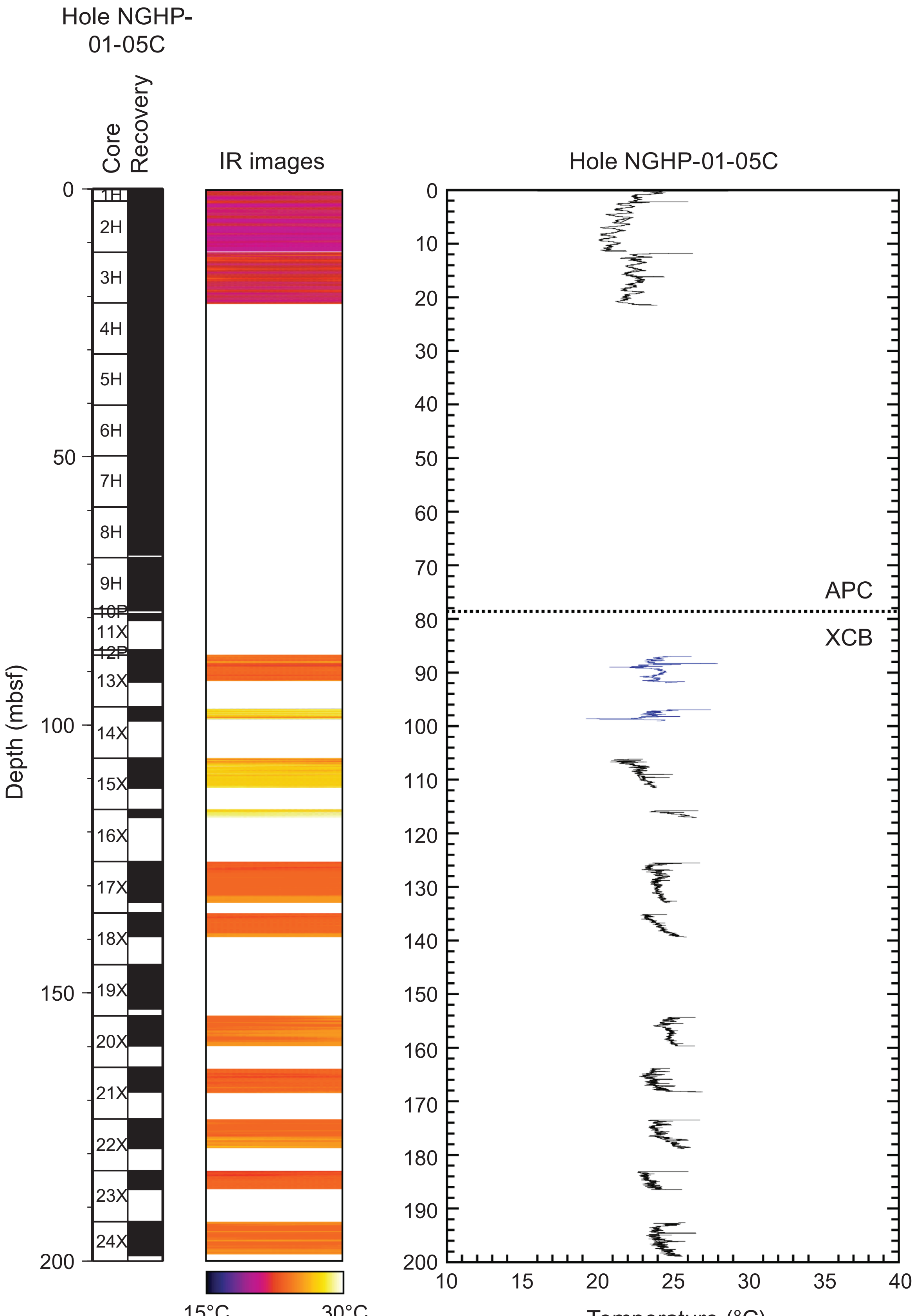

Figure 19. Infrared imaging and the derived downhole temperature profile for Hole NGHP-01-05C.

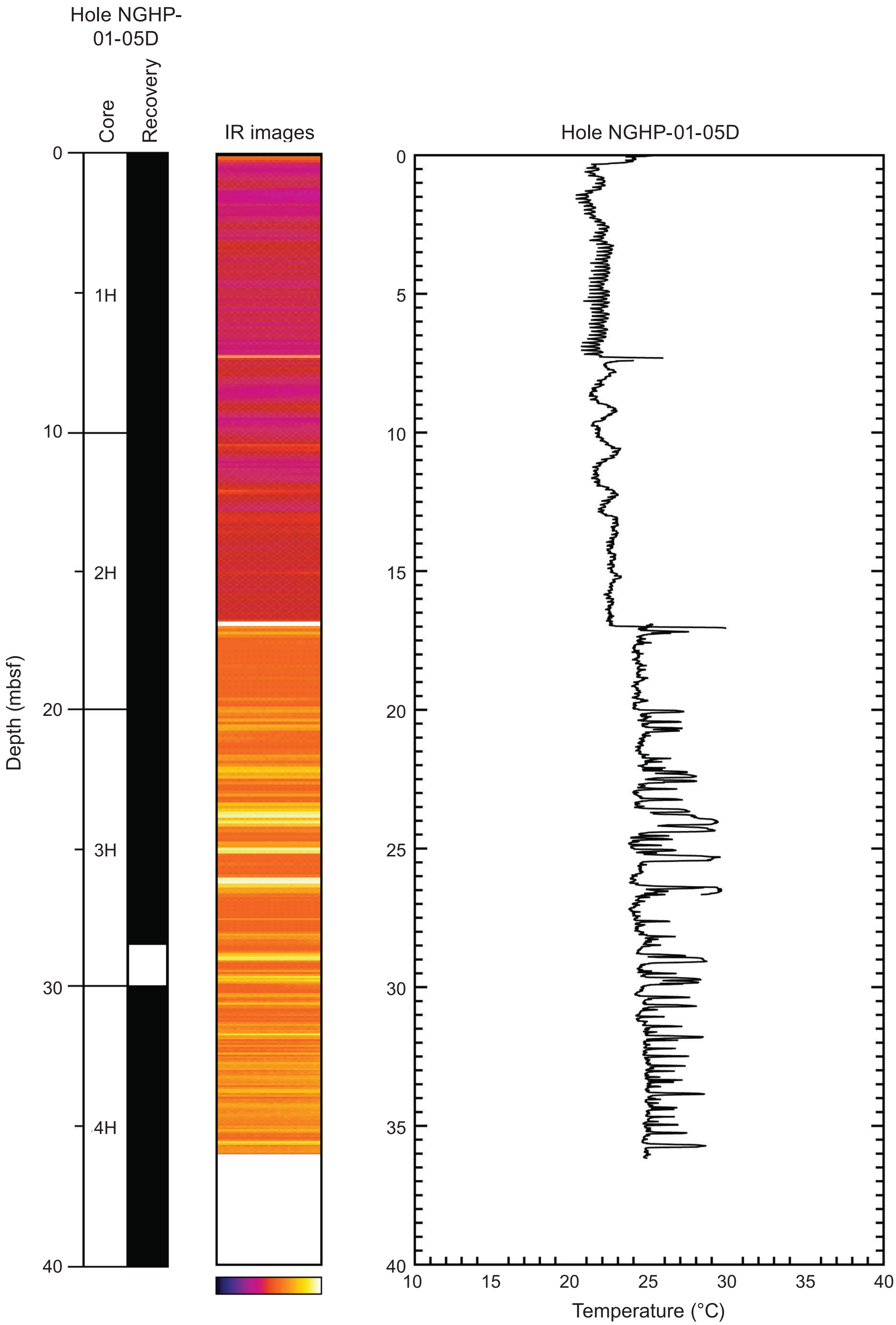

Figure 20. Infrared imaging and the derived downhole temperature profile for Hole NGHP-01-05D.

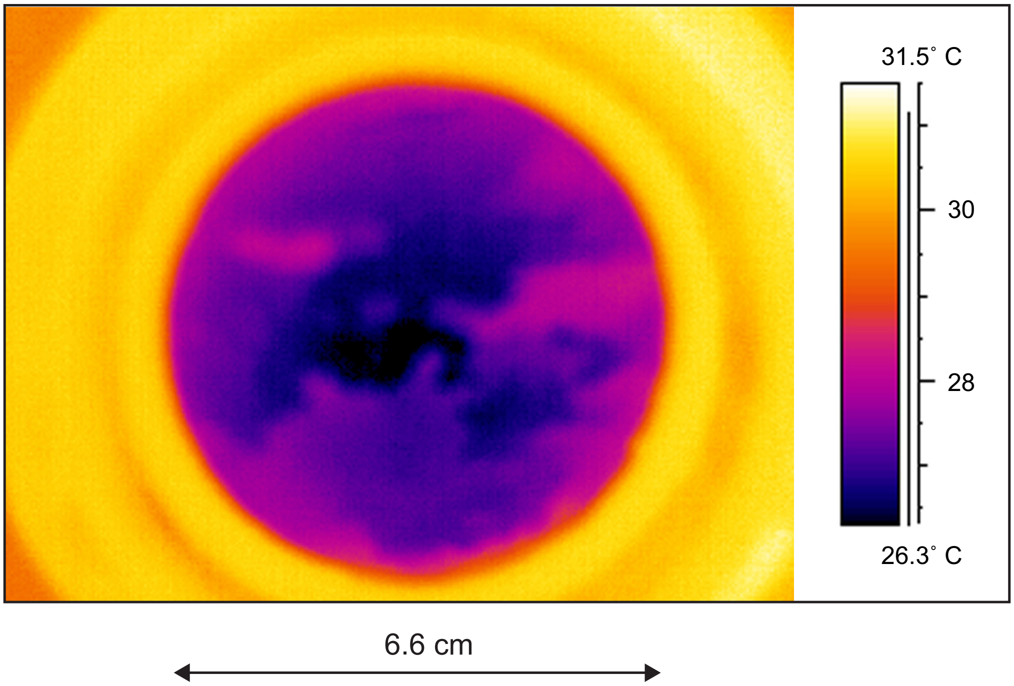

Figure 21. Core-end infrared image of Section NGHP-01-05C-24X-4, top, with the corresponding reference temperature scale.

Index Properties

Composite profiles of core recovery and measurements and results from LWD, IR imaging, MSCL, MAD, and other programs are presented in figures 23 and 24. Water content (related to solids) varies from 128 percent at the top of Hole NGHP-01-05C to 32 percent at the bottom of the hole and has a high linear rate of decrease in the upper 16 m (table 16; fig. 23). The rate becomes more gradual below that depth. Porosity determined from MAD samples decreases nearly linearly from 76 to 46 percent downhole. This trend is overall in close agreement with the porosity values determined from LWD except in the upper 50 m where borehole conditions prevented accurate *in situ* measurements. The LWD porosity values decrease near the base of gas-hydrate stability; however, this trend is not lithologically controlled. The dissociation of gas hydrate greatly influences the consistency of recovered cores. For example, water contents varied over a factor of two, from 33 to 68 percent, in PCS Core NGHP-01-05C-12P recovered from 86.0 to 86.6 mbsf. Parts of the core that apparently contained gas hydrate exhibited classic soupy behavior, while nearby sediment was intact and less disturbed. There is a change in slope of both the water content and porosity at the APC–XCB boundary located at 78.3 mbsf.

Coincident with the decrease in porosity, bulk density from MAD measurements increased at a greater rate with depth in the top of the core and more gradually below 50 mbsf (fig. 23). Bulk density determined from the MSCL as well as LWD indicated a coincidental increase in density near the base of gas-hydrate stability. MAD density changed significantly in Core NGHP-01-05C-12P as a result of gas-hydrate dissociation.

Grain density varied from 2.45 to 2.91 g/cm^3 with an average value of 2.69. Some of this variation is a result of performing mass measurements at sea on small sediment samples after the water has been removed by drying. This result is most pronounced in the upper sections of the hole where water contents are highest. Grain densities are lower in the upper part of the hole, possibly the result of increased organic content (see "Lithostratigraphy"). The pycnometers often had difficulty measuring volume of samples from the top of the hole. Higher grain densities may be related to the presence of carbonate which has a slightly higher grain density (2.73 g/cm^3).

Strength

Shear strength increased linearly with depth to approximately 40 mbsf as determined using three different methods (tables 17, 18 and 19; fig. 23). Below that depth there was somewhat more variation in the properties. However, the variation in properties increased when XCB coring began, illustrating the effect of disturbance caused by rotary coring on sediment. Although testing was to be restricted to intact biscuits, sometimes it was difficult to differentiate between intact biscuits and adjacent disturbed sediment.

The measured shear strengths were normalized to the effective vertical stress, σ'_v (fig. 23) to provide qualitative information on the stress history of the sediment. The strength/effective vertical stress ranges from 0.49 at the top of the hole to 0.04 near the bottom of the hole. These values are in overall agreement with a number of other normally consolidated clays (Holtz and Kovacs, 1981), although the values below 0.1 probably represent the deeper subbottom depth from this hole compared to most engineering-type projects from which the comparison samples were taken. Hunt (1984) states that the strength/effective vertical stress ratio typically is between 0.4 and 0.16. The wide scatter in the results at the top of the hole reflects the dependency of this ratio on the stress path as well as the test method (Bjerrum, 1972; Ladd, and others, 1977). The implication is that these sediments are depositional in nature and have not been overconsolidated by erosional or other geologic processes.

The peak (Sv) and remolded (Srem) vane shear strengths and sensitivity (St), which equals Sv/Srem, all increase with depth (fig. 25). Sensitivity values from Hole NGHP-01-05C represent the amount of strength loss after remolding and in extreme examples can reach values of 500 (Lambe and Whitman, 1969). Sensitivity values range from 2 to 18, with values about 3 above 25 mbsf and higher values up to 10 below that depth. The classification typically used in the United States categorizes the clays as low to highly sensitive (Holtz and Kovacs, 1981). However, other classifications that are used in regions containing uplifted marine clays would only classify the sediment as low sensitivity. High values of sensitivity are indicative of good quality core recovery because the sediment has not been highly disturbed.

Electrical Resistivity

Electrical resistivity values between LWD (A40L) conducted in Hole NGHP-01-05A, MSCL, and the Wenner array performed on split cores show interesting trends (fig. 24). The LWD values increase slightly downhole to 2 Ω-m at 70 mbsf, then increase abruptly and stay elevated in the gas-hydrate zone to 95 mbsf. The LWD values decrease to 1 Ω-m at 115 mbsf and stay at that value to the bottom of the hole. Obviously, the increase in LWD resistivity is due to the presence of gas hydrate *in situ*.

The MSCL and Wenner-array data reflect background sediment values after gas hydrate has dissociated. Electrical resistivity measured by the MSCL increases at approximately 30 mbsf and then decreases to values in the range between 0.4 and about 1.0 Ω-m (fig. 24). The Wenner-array measurements (table 20; fig. 24) gradually increase from about 0.4 Ω-m near the seafloor to about 0.7 Ω-m at 100 mbsf. They then gradually decrease to about 0.5 Ω-m at the bottom of the hole. The Wenner measurements are performed at selected locations on intact core material, hence the lower values than for the MSCL which senses a wider portion of core that may contain voids or small expansion cracks. Lower MSCL values are more representative of undisturbed sediment as they do not reflect the presence of such micro voids caused by gas expansion.

P-Wave Velocity

P-wave velocity measured with the MSCL increased slightly from 1.48 to 1.55 km/s from the top of NGHP-01-05C to 22 mbsf, where gas and voids present in the sediment prevented further valid measurements from being logged. The contact V_p values (table 21; fig. 24) are in close agreement and increased from 1.5 km/s at the top of Hole NGHP-01-05C to 1.54 km/s at 23 mbsf with one excursion at 10.5 mbsf.

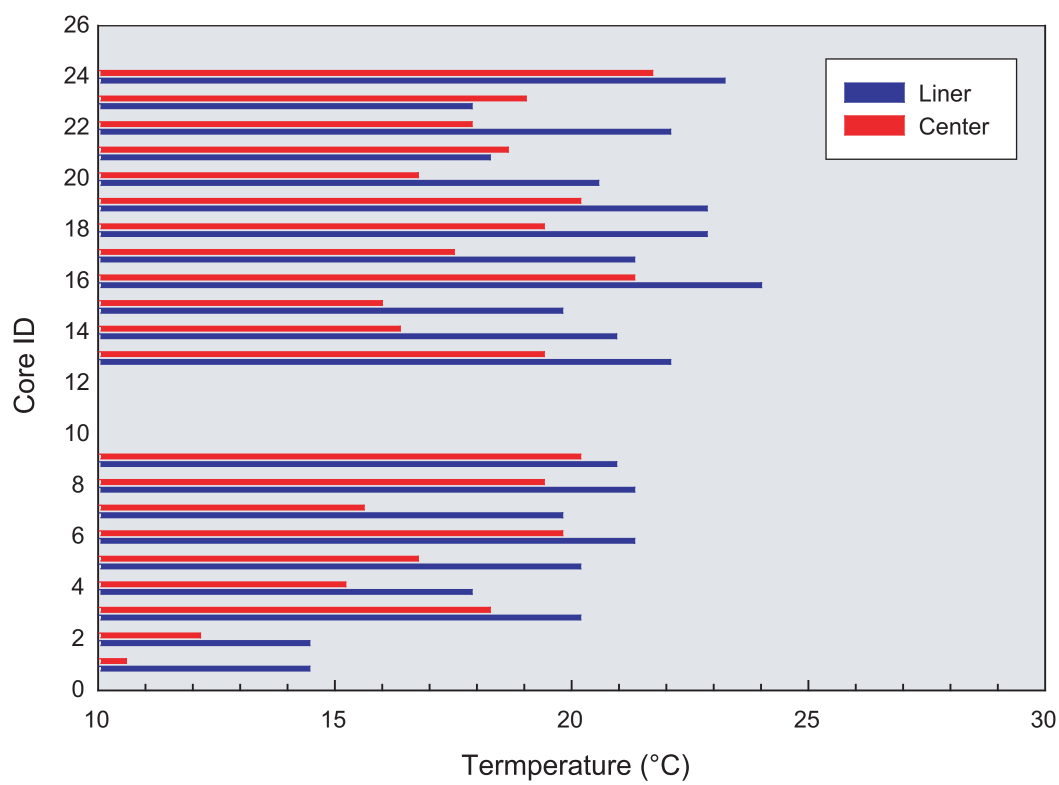

Figure 22. Core-end temperature measurements for Hole NGHP-01-05C.

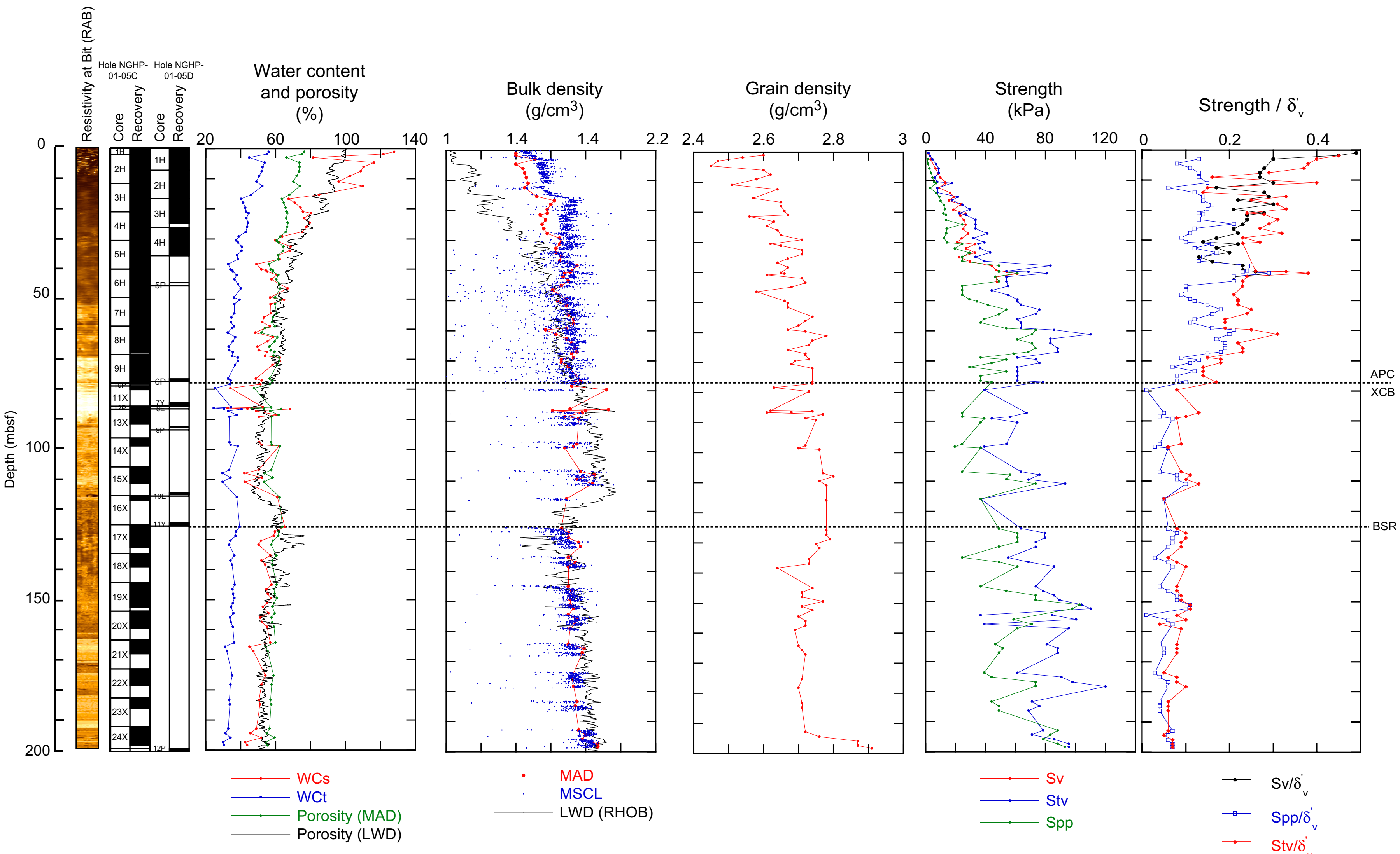

Figure 23. Profiles of LWD resistivity-at-bit (RAB), core recovery, index and strength properties for Site NGHP-01-05. [LWD, logging-while-drilling]

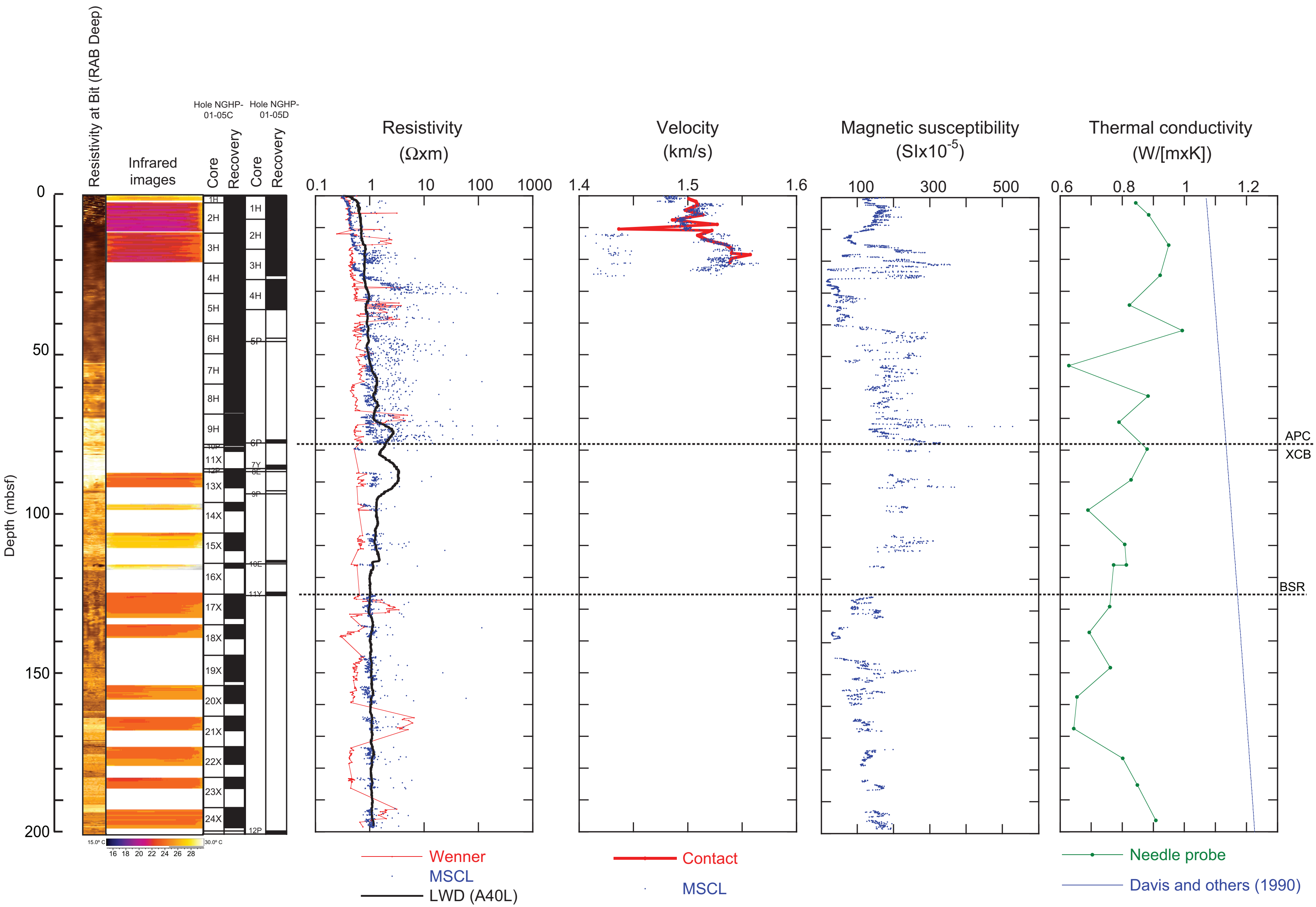

Figure 24. Profiles of LWD resistivity-at-bit (RAB), core recovery, infrared images, electrical resistivity, acoustic P-wave velocity, magnetic susceptibility, and thermal conductivity for Site NGHP-01-05. [LWD, logging-while-drilling]

Table 16. Moisture and density (MAD) physical properties for Holes NGHP-01-05C and NGHP-01-05D.

Core, section, interval (cm)	Sample code	Depth (mbsf)	WCt (%)	WCs (%)	Grain density (g/cm³)	Bulk density (g/cm³)	Dry bulk density (g/cm³)	Porosity (%)	Void ratio	Unit weight (kN/m³)
					NGHP-01-05C					
1H-1,102-104	MAD	1.02	56.12	127.88	2.6	1.4	0.61	76.37	3.23	13.7
1H-2,33-35	MAD	1.83	54.91	121.8	2.54	1.4	0.63	75.06	3.01	13.76
2H-1,64-66	MAD	2.94	44.91	81.54	2.47	1.51	0.83	66.25	1.96	14.85
2H-2,81-83	MAD	4.61	53.78	116.36	2.45	1.4	0.65	73.5	2.77	13.76
2H-3,72-74	MAD	6.02	52.49	110.47	2.6	1.44	0.68	73.7	2.8	14.14
2H-4,72-74	MAD	7.52	52.09	108.72	2.62	1.45	0.69	73.5	2.77	14.21
2H-5,72-74	MAD	9.02	50.61	102.47	2.58	1.46	0.72	72.05	2.58	14.33
2H-7,11-13	MAD	10.91	49.02	96.15	2.51	1.47	0.75	70.12	2.35	14.4
3H-1,60-62	MAD	12.4	52.37	109.96	2.64	1.45	0.69	73.86	2.83	14.2
3H-3,58-60	MAD	15.38	45.87	84.74	2.57	1.52	0.82	67.92	2.12	14.91
3H-4,37-39	MAD	16.67	40.28	67.46	2.65	1.62	0.97	63.55	1.74	15.88
3H-5,16-18	MAD	17.96	41.51	70.97	2.65	1.6	0.94	64.69	1.83	15.69
3H-6,33-35	MAD	19.63	42.65	74.36	2.66	1.58	0.91	65.77	1.92	15.53
3H-7,9-11	MAD	20.89	43.06	75.63	2.67	1.58	0.9	66.31	1.97	15.5
4H-1,12-14	MAD	21.42	44.53	80.28	2.56	1.54	0.85	66.7	2	15.08
4H-2,28-30	MAD	23.08	43.32	76.42	2.63	1.57	0.89	66.13	1.95	15.37
4H-3,29-31	MAD	24.59	44.3	79.53	2.61	1.55	0.87	67	2.03	15.23
4H-4,20-22	MAD	26.00	43.74	77.74	2.64	1.56	0.88	66.65	2	15.34
4H-5,32-34	MAD	27.62	42.91	75.17	2.65	1.58	0.9	65.95	1.94	15.47
4H-6,36-38	MAD	29.16	38.92	63.73	2.71	1.65	1.01	62.68	1.68	16.21
4H-7,22-24	MAD	30.52	37.45	59.88	2.62	1.66	1.04	60.42	1.53	16.24
5H-1,34-36	MAD	31.14	38.37	62.26	2.65	1.65	1.02	61.69	1.61	16.19
5H-2,43-45	MAD	32.58	40.68	68.59	2.71	1.63	0.96	64.44	1.81	15.95
5H-3,36-38	MAD	34.01	40.51	68.1	2.71	1.63	0.97	64.24	1.8	15.97
5H-4,26-28	MAD	35.41	38.05	61.41	2.67	1.66	1.03	61.52	1.6	16.28
5H-5,22-24	MAD	36.81	38.42	62.38	2.64	1.65	1.01	61.62	1.61	16.15
5H-6,26-28	MAD	38.35	32.89	49.01	2.67	1.75	1.17	56.06	1.28	17.16
5H-7,52-54	MAD	40.09	34.16	51.89	2.65	1.72	1.13	57.25	1.34	16.87
6H-1,14-16	MAD	40.44	35.23	54.4	2.66	1.71	1.1	58.52	1.41	16.72
6H-2,22-24	MAD	40.86	35.59	55.26	2.61	1.68	1.09	58.4	1.4	16.52
6H-3,16-18	MAD	41.97	37.77	60.7	2.71	1.67	1.04	61.57	1.6	16.41
6H-4,16-18	MAD	43.47	36.53	57.56	2.72	1.7	1.08	60.39	1.52	16.64
6H-5,16-18	MAD	44.95	38.34	62.18	2.68	1.66	1.03	62.17	1.64	16.33
6H-6,17-19	MAD	46.46	40.09	66.9	2.58	1.61	0.96	62.74	1.68	15.76
6H-8,20-22	MAD	49.46	36.27	56.92	2.66	1.69	1.08	59.62	1.48	16.55
7H-1,42-44	MAD	50.22	39.33	64.82	2.67	1.64	0.99	62.77	1.69	16.07
7H-2,44-46	MAD	51.66	36.38	57.18	2.67	1.69	1.07	59.76	1.49	16.54
7H-4,55-57	MAD	54.77	36.45	57.37	2.74	1.7	1.08	60.5	1.53	16.71
7H-5,44-46	MAD	56.16	34.75	53.27	2.72	1.73	1.13	58.49	1.41	16.95
7H-6,45-47	MAD	57.67	34.39	52.41	2.7	1.73	1.14	57.97	1.38	16.97
7H-7,45-47	MAD	59.12	36.22	56.8	2.67	1.69	1.08	59.65	1.48	16.58
8H-1,37-39	MAD	59.67	35.12	54.14	2.72	1.57	1.02	53.83	1.17	15.43
8H-2,32-34	MAD	61.12	32.65	48.47	2.78	1.63	1.1	51.82	1.08	15.98
8H-3,37-39	MAD	62.67	36.95	58.61	2.74	1.69	1.07	60.98	1.56	16.62
8H-4,32-34	MAD	64.12	35.59	55.26	2.73	1.72	1.1	59.47	1.47	16.82
8H-5,48-50	MAD	65.78	33.19	49.67	2.67	1.74	1.17	56.39	1.29	17.11
8H-6,26-28	MAD	67.06	33.5	50.37	2.72	1.75	1.17	57.2	1.34	17.19
8H-7,24-26	MAD	67.55	35.53	55.11	2.72	1.72	1.11	59.37	1.46	16.82
9H-1,10-12	MAD	68.9	35.02	53.89	2.73	1.73	1.12	58.87	1.43	16.93
9H-2,11-13	MAD	69.51	38.43	62.42	2.69	1.66	1.02	62.01	1.63	16.25
9H-3,5-7	MAD	70.53	38.48	62.55	2.68	1.66	1.02	62.06	1.64	16.24
9H-4,4-6	MAD	71.95	36.79	58.21	2.74	1.7	1.07	60.86	1.55	16.65
9H-7,4-6	MAD	76.45	32.79	48.78	2.74	1.77	1.19	56.58	1.3	17.37

Table 16. Moisture and density (MAD) physical properties for Holes NGHP-01-05C and NGHP-01-05D.—Continued

Core, section, interval (cm)	Sample code	Depth (mbsf)	WCt (%)	WCs (%)	Grain density (g/cm³)	Bulk density (g/cm³)	Dry bulk density (g/cm³)	Porosity (%)	Void ratio	Unit weight (kN/m³)
NGHP-01-05C—Continued										
9H-8,12-14	MAD	77.1	34.22	52.03	2.74	1.74	1.15	58.11	1.39	17.1
10P-1,7-9	MAD	78.37	33.93	51.35	2.63	1.72	1.14	56.82	1.32	16.86
11X-1,34-36	MAD	79.64	25.48	34.19	2.73	1.92	1.43	47.64	0.91	18.83
12P-1,0-2	MAD	86	34.56	52.81	2.62	1.71	1.12	57.42	1.35	16.73
12P-1,26-28	MAD	86.26	24.58	32.6	2.74	1.93	1.46	46.26	0.86	18.95
12P-1,48-50	MAD	86.48	30.5	43.89	2.68	1.8	1.25	53.38	1.15	17.62
12P-1,60-62	MAD	86.6	40.52	68.13	2.61	1.61	0.95	63.36	1.73	15.74
13X-1,28-30	MAD	87.28	32.84	48.91	2.77	1.78	1.2	56.92	1.32	17.45
13X-2,22-24	MAD	88.52	37.76	60.66	2.72	1.68	1.04	61.68	1.61	16.45
13X-3,27-29	MAD	89.17	33.59	50.58	2.75	1.76	1.17	57.53	1.35	17.25
14X-1,70-72	MAD	97.6	33.67	50.75	2.72	1.75	1.16	57.39	1.35	17.16
14X-2,12-14	MAD	98.52	34.23	52.04	2.7	1.73	1.14	57.74	1.37	16.98
14X-3,26-28	MAD	98.95	38.27	62	2.76	1.68	1.03	62.49	1.67	16.44
15X-1,63-65	MAD	106.83	33.46	50.29	2.77	1.77	1.18	57.57	1.36	17.32
15X-2,20-22	MAD	107.9	29.65	42.16	2.8	1.85	1.3	53.5	1.15	18.17
15X-3,16-18	MAD	109.36	34.21	52	2.76	1.75	1.15	58.29	1.4	17.15
15X-4,15-17	MAD	110.85	29.73	42.31	2.78	1.84	1.3	53.4	1.15	18.09
16X-1,10-12	MAD	115.9	37.88	60.99	2.78	1.69	1.05	62.27	1.65	16.55
17X-1,28-30	MAD	125.78	39.49	65.25	2.78	1.66	1.01	63.88	1.77	16.29
17X-2,28-30	MAD	127.28	37.38	59.69	2.78	1.7	1.06	61.75	1.61	16.63
17X-3,29-31	MAD	128.79	37.08	58.94	2.79	1.7	1.07	61.56	1.6	16.71
17X-4,35-37	MAD	130.35	34.1	51.74	2.75	1.76	1.16	58.5	1.41	17.27
17X-5,24-26	MAD	131.74	33.45	50.25	2.76	1.77	1.17	57.5	1.35	17.31
18X-1,27-29	MAD	135.37	36.37	57.17	2.73	1.7	1.08	60.33	1.52	16.7
18X-2,35-37	MAD	136.95	34.18	51.92	2.73	1.74	1.15	58.01	1.38	17.09
18X-3,25-27	MAD	138.35	35.11	54.12	2.64	1.7	1.1	58.18	1.39	16.68
19X-1,34-36	MAD	145.04	36.58	57.68	2.74	1.7	1.08	60.61	1.54	16.68
19X-2,31-33	MAD	146.51	35.37	54.73	2.71	1.72	1.11	59.11	1.45	16.83
19X-3,32-34	MAD	148.02	35.71	55.56	2.71	1.71	1.1	59.47	1.47	16.77
19X-4,24-26	MAD	149.44	36.43	57.3	2.77	1.71	1.09	60.74	1.55	16.79
19X-5,31-33	MAD	151.11	35.51	55.05	2.71	1.71	1.1	59.22	1.45	16.79
19X-6,17-19	MAD	152.37	34.54	52.77	2.74	1.73	1.13	58.25	1.4	16.98
20X-1,19-21	MAD	154.49	35.87	55.92	2.7	1.7	1.09	59.5	1.47	16.7
20X-2,18-20	MAD	155.98	33.9	51.29	2.72	1.75	1.15	57.63	1.36	17.12
20X-3,18-20	MAD	157.48	34.33	52.28	2.72	1.74	1.14	58.09	1.39	17.04
20X-4,21-23	MAD	159.01	35.53	55.1	2.69	1.71	1.1	59.09	1.44	16.75
21X-1,39-41	MAD	164.29	36.29	56.95	2.7	1.7	1.08	59.93	1.5	16.63
21X-2,23-25	MAD	165.63	31.09	45.11	2.71	1.79	1.24	54.34	1.19	17.6
21X-3,25-27	MAD	167.15	32.1	47.28	2.72	1.78	1.21	55.57	1.25	17.43
22X-2,20-22	MAD	175.2	35.16	54.21	2.71	1.72	1.11	58.85	1.43	16.86
22X-3,25-27	MAD	176.75	34.12	51.78	2.71	2	1.32	66.39	1.98	19.59
22X-4,25-27	MAD	178.25	34.21	51.99	2.7	1.73	1.14	57.78	1.37	17.01
23X-1,24-26	MAD	183.34	33.58	50.57	2.71	1.75	1.16	57.16	1.33	17.14
23X-2,18-20	MAD	184.78	33.82	51.1	2.71	1.74	1.15	57.43	1.35	17.1
24X-1,16-18	MAD	192.86	32.89	49.01	2.72	1.76	1.18	56.52	1.3	17.3
24X-2,25-27	MAD	194.45	31.29	45.54	2.76	1.8	1.24	55.01	1.22	17.7
24X-3,25-27	MAD	195.95	34.21	52	2.87	1.78	1.17	59.27	1.46	17.44
24X-4,25-27	MAD	197.45	29.9	42.64	2.87	1.87	1.31	54.38	1.19	18.32
24X-5,18-20	MAD	198.38	30.42	43.72	2.91	1.87	1.3	55.3	1.24	18.3
NGHP-01-05D										
6P-1,16-18	MAD	77.06	35.99	56.22	2.73	1.71	1.09	59.94	1.5	16.73
7Y-1,56-58	MAD	85.46	33.17	49.64	2.73	1.76	1.17	56.84	1.32	17.21
11Y-1,30-32	MAD	125.2	34.74	53.22	2.73	1.73	1.13	58.64	1.42	16.96
12P-1,16-18	MAD	200.16	30.11	43.09	2.72	1.82	1.27	53.61	1.16	17.88

Table 17. Vane shear strength results for Hole NGHP-01-05C.

Core, section, depth (cm, in section)	Sample	Depth in section (cm)	Depth (mbsf)	Sv (kPa)	Sres (kPa)	Srem (kPa)	St
NGHP-01-05C							
1H-1,100	VS	100	1	1.73	1.56	0.91	1.91
1H-2,31	VS	31	1.81	2.96	1.81	0.16	18
2H-1,62	VS	62	2.92	3.37	2.47	1.73	1.95
2H-3,71	VS	71	6.01	6.58	4.28	2.3	2.86
2H-4,78	VS	78	7.58	8.23	4.11	2.3	3.57
2H-5,75	VS	75	9.05	9.87	3.95	2.3	4.29
2H-6,68	VS	68	10.48	13	4.94	3.46	3.76
2H-7,10	VS	10	10.9	13.33	6.75	3.79	3.52
3H-1,67	VS	67	12.47	8.89	3.46	3.29	2.7
3H-2,79	VS	79	14.09	16.46	6.58	4.94	3.33
3H-3,60	VS	60	15.4	18.93	11.52	6.58	2.88
3H-4,40	VS	40	16.7	15.63	9.87	5.02	3.11
3H-5,16	VS	16	17.96	23.53	13.99	6.58	3.58
3H-6,41	VS	41	19.71	18.51	9.46	6.42	2.88
3H-7,20	VS	20	21	26.74	15.63	8.23	3.25
4H-1,33	VS	33	21.63	23.2	12.18	6.42	3.62
4H-2,35	VS	35	23.15	25.51	13.08	10.08	2.53
4H-3,40	VS	40	24.7	26.74	14.81	9.38	2.85
4H-4,31	VS	31	26.11	25.18	11.44	4.94	5.1
4H-5,40	VS	40	27.7	28.39	9.05	3.29	8.63
4H-6,44	VS	44	29.24	24.03	8.06	3.21	7.49
4H-7,21	VS	21	30.51	21.23	6.42	1.97	10.75
5H-1,40	VS	40	31.2	32.91	18.93	11.68	2.82
5H-2,40	VS	40	32.55	26.99	19.09	11.6	2.33
5H-3,40	VS	40	34.05	32.91	15.63	7.08	4.65
5H-4,40	VS	40	35.55	22.38	9.46	4.2	5.33
5H-5,40	VS	40	36.99	29.7	14.81	6.5	4.57
5H-6,33	VS	33	38.42	44.27	16.46	6.5	6.81
5H-7,21	VS	21	39.78	47.07	14.73	6.58	7.15
6H-1,12	VS	12	40.42	54.31	20.65	15.63	3.47
6H-2,40	VS	40	41.04	61.06	18.1	5.76	10.6
6H-3,30	VS	30	42.11	46.9	19.75	16.46	2.85
6H-4,35	VS	35	43.66	47.64	16.46	13.99	3.41

Table 18. Torvane strength results for Hole NGHP-01-05C.

Core, section, depth (cm, in section)	Sample	Depth (mbsf)	Stv (kPa)	Core, section, depth (cm, in section)	Sample	Depth (mbsf)	Stv (kPa)
NGHP-01-05C							
1H-1,91	TV	0.91	1.96	9H-4,19	TV	72.1	61.29
1H-2,34	TV	1.84	2.94	9H-5,18	TV	73.59	61.29
2H-1,65	TV	2.95	4.51	9H-6,9	TV	75	61.29
2H-2,82	TV	4.62	7.06	9H-8,7	TV	77.05	78.45
2H-3,73	TV	6.03	8.83	11X-1,38	TV	79.68	39.23
2H-4,73	TV	7.53	8.83	13X-1,33	TV	87.33	67.42
2H-5,73	TV	9.03	5.88	13X-2,27	TV	88.57	56.39
2H-6,67	TV	10.47	7.85	13X-3,23	TV	89.13	44.13
2H-7,8	TV	10.88	17.65	13X-4,6	TV	90.46	61.29
3H-1,69	TV	12.49	7.85	14X-1,71	TV	97.61	53.94
3H-2,73	TV	14.03	7.85	14X-2,14	TV	98.54	39.23
3H-3,62	TV	15.42	21.57	14X-3,19	TV	98.88	36.77
3H-4,33	TV	16.63	17.65	15X-1,68	TV	106.88	63.74
3H-5,23	TV	18.03	24.52	15X-2,21	TV	107.91	76
3H-6,34	TV	19.64	29.42	15X-3,26	TV	109.46	68.65
3H-7,13	TV	20.93	22.56	15X-4,16	TV	110.86	93.16
4H-1,10	TV	21.4	26.97	16X-1,13	TV	115.93	36.77
4H-2,29	TV	23.09	33.34	17X-1,27	TV	125.77	63.74
4H-3,29	TV	24.59	33.34	17X-2,27	TV	127.27	79.68
4H-4,21	TV	26.01	33.34	17X-3,32	TV	128.82	79.68
4H-5,33	TV	27.63	41.19	17X-4,32	TV	130.32	73.55
4H-6,37	TV	29.17	31.87	17X-5,32	TV	131.82	73.55
4H-7,30	TV	30.6	39.23	18X-1,34	TV	135.44	55.16
5H-1,27	TV	31.07	35.3	18X-2,34	TV	136.94	68.65
5H-2,36	TV	32.51	36.28	18X-3,28	TV	138.38	85.81
5H-3,37	TV	34.02	43.15	19X-1,31	TV	145.01	73.55
5H-4,27	TV	35.42	33.34	19X-2,30	TV	146.5	78.45
5H-5,28	TV	36.87	39.23	19X-3,30	TV	148	85.81
5H-6,30	TV	38.39	83.36	19X-4,30	TV	149.5	89.49
5H-7,61	TV	40.18	53.94	19X-5,30	TV	151.1	104.2
6H-1,9	TV	40.39	68.65	19X-6,22	TV	152.42	110.32
6H-2,22	TV	40.86	80.9	20X-1,22	TV	154.52	36.77
6H-3,23	TV	42.04	53.94	20X-1,25	TV	154.55	84.58
6H-4,29	TV	43.6	53.94	20X-2,22	TV	156.02	100.52
6H-5,37	TV	45.16	55.16	20X-3,23	TV	157.53	39.23
6H-7,30	TV	48.09	55.16	20X-4,19	TV	158.99	95.61
6H-8,31	TV	49.57	61.29	21X-1,36	TV	164.26	80.9
7H-1,42	TV	50.22	61.29	21X-2,20	TV	165.6	88.26
7H-2,10	TV	51.32	63.74	21X-3,23	TV	167.13	88.26
7H-3,23	TV	52.95	76	22X-1,23	TV	173.73	61.29
7H-4,11	TV	54.33	73.55	22X-2,18	TV	175.18	90.71
7H-5,41	TV	56.13	61.29	22X-3,29	TV	176.79	98.07
7H-6,8	TV	57.3	63.74	22X-4,31	TV	178.31	120.13
7H-7,44	TV	59.11	63.74	23X-1,23	TV	183.33	71.1
8H-1,42	TV	59.72	85.81	23X-2,22	TV	184.82	76
8H-2,37	TV	61.17	110.32	23X-3,22	TV	186.32	68.65
8H-4,36	TV	64.16	83.36	24X-1,19	TV	192.89	78.45
8H-5,53	TV	65.83	88.26	24X-2,19	TV	194.39	71.1
8H-6,29	TV	67.09	88.26	24X-3,19	TV	195.89	85.81
9H-1,7	TV	68.87	61.29	24X-4,19	TV	197.39	95.61
9H-2,8	TV	69.48	73.55	24X-5,19	TV	198.39	95.61
9H-3,26	TV	70.74	76				

Table 19. Pocket Penetrometer strength results for Hole NGHP-01-05C.

Core, section, depth (cm, in section)	Sample	Depth (mbsf)	Spp (kPa)	Core, section, depth (cm, in section)	Sample	Depth (mbsf)	Spp (kPa)
NGHP-01-05C							
2H-1,60	PP	2.9	1.5	9H-2,14	PP	69.54	53.9
2H-2,62	PP	4.42	1.5	9H-3,22	PP	70.7	44.1
2H-3,68	PP	5.98	2.6	9H-4,15	PP	72.06	29.4
2H-4,71	PP	7.51	3.8	9H-5,16	PP	73.57	53.9
2H-5,77	PP	9.07	4.6	9H-6,10	PP	75.01	36.8
2H-6,70	PP	10.5	5.8	9H-7,15	PP	76.56	36.8
2H-7,12	PP	10.92	6.9	9H-8,10	PP	77.08	44.1
3H-1,69	PP	12.49	3.1	13X-1,28	PP	87.28	24.5
3H-2,81	PP	14.11	6.9	13X-2,23.5	PP	88.535	24.5
3H-3,59	PP	15.39	9.2	13X-3,26	PP	89.16	39.2
3H-4,46	PP	16.76	10	13X-4,8	PP	90.48	36.8
3H-5,31	PP	18.11	12.3	14X-1,73.5	PP	97.635	24.5
3H-6,30	PP	19.6	12.9	14X-2,13	PP	98.53	19.6
3H-7,10	PP	20.9	11.9	14X-3,27	PP	98.96	36.8
4H-1,11	PP	21.41	13.6	15X-1,66	PP	106.86	24.5
4H-2,33	PP	23.13	13.6	15X-2,19	PP	107.89	56.4
4H-3,33	PP	24.63	24.5	15X-3,16	PP	109.36	53.9
4H-4,18	PP	25.98	14.1	15X-4,14	PP	110.84	73.5
4H-5,29	PP	27.59	13.8	16X-1,16	PP	115.96	36.8
4H-6,33	PP	29.13	12.3	17X-1,30	PP	125.8	49
4H-7,30	PP	30.6	14.2	17X-2,30	PP	127.3	61.3
5H-1,35	PP	31.15	24.5	17X-3,30	PP	128.8	61.3
5H-2,45	PP	32.6	19.6	17X-4,30	PP	130.3	61.3
5H-3,43	PP	34.08	29.4	17X-5,30	PP	131.8	49
5H-4,29	PP	35.44	24.5	18X-1,30	PP	135.4	24.5
5H-5,25	PP	36.84	24.5	18X-2,31	PP	136.91	49
5H-6,25	PP	38.34	49	18X-3,30	PP	138.4	61.3
5H-7,58	PP	40.15	49	19X-1,30	PP	145	36.8
6H-1,7	PP	40.37	49	19X-2,30	PP	146.5	53.9
6H-2,21	PP	40.85	61.3	19X-3,30	PP	148	73.5
6H-3,20	PP	42.01	46.6	19X-4,30	PP	149.5	73.5
6H-4,26	PP	43.57	49	19X-5,30	PP	151.1	102.9
6H-5,25	PP	45.04	24.5	19X-6,20	PP	152.4	98
6H-6,20	PP	46.49	24.5	20X-2,23	PP	156.03	58.8
6H-7,25	PP	48.04	24.5	20X-3,24	PP	157.54	71.1
6H-8,25	PP	49.51	29.4	20X-4,19	PP	158.99	61.3
7H-1,42	PP	50.22	34.3	21X-1,38	PP	164.28	46.6
7H-2,12	PP	51.34	41.7	21X-2,19	PP	165.59	51.5
7H-3,21	PP	52.93	53.9	21X-3,23	PP	167.13	49
7H-4,29	PP	54.51	49	22X-1,20	PP	173.7	39.2
7H-5,40	PP	56.12	39.2	22X-2,16	PP	175.16	44.1
7H-6,8	PP	57.3	36.8	22X-3,28	PP	176.78	73.5
7H-7,46	PP	59.13	53.9	22X-4,20	PP	178.2	73.5
8H-1,41	PP	59.71	73.5	23X-1,21	PP	183.31	44.1
8H-2,40	PP	61.2	71.1	23X-2,21	PP	184.81	49
8H-3,50	PP	62.8	61.3	23X-3,21	PP	186.31	49
8H-4,38	PP	64.18	71.1	24X-1,21	PP	192.91	88.2
8H-5,54	PP	65.84	73.5	24X-2,21	PP	194.41	83.3
8H-6,21	PP	67.01	68.6	24X-3,21	PP	195.91	78.4
8H-7,28	PP	67.59	58.8	24X-4,21	PP	197.41	88.2
9H-1,9	PP	68.89	36.8	24X-5,15	PP	198.35	93.1

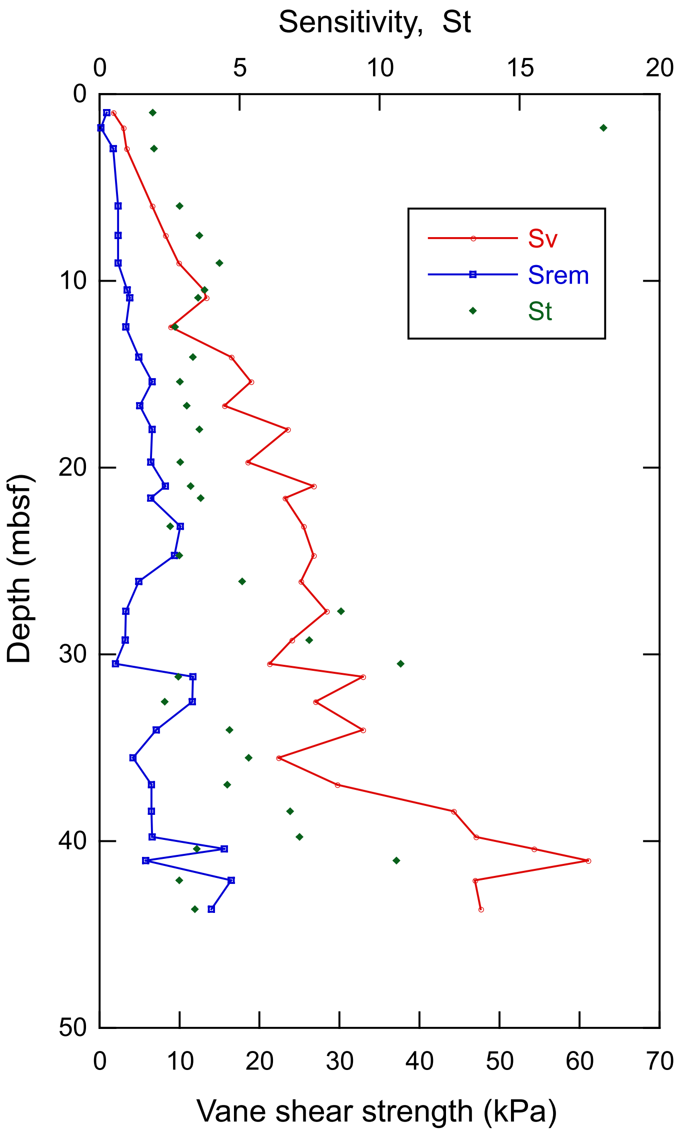

Figure 25. Peak and remolded vane shear strengths and sensitivity for Hole NGHP-01-05C.

Magnetic Susceptibility

Background magnetic susceptibility typically varies between 100 and 200x10^{-5} SI above 15 mbsf and below 140 mbsf (fig. 24). In between those depths, wide excursions exist in the data indicating that primary magnetic minerals are present (see "Lithostratigraphy"). However, such excursions are not related to lithologic controls and, although coincident to the location of gas hydrate, do not have a known direct influence on the formation of gas hydrate.

Thermal Conductivity

Thermal conductivities vary between 0.63 and 0.99 W/(m×K) and decrease down core to 170 mbsf at which point the values increase (table 22; fig. 24). Such values are well within the range of marine sediments (for example, Novosel, and others, 2007). However, they are less than values determined by Davis and others, 1990 for sediment from the Cascadia accretionary prism and Nankai Trough.

Downhole Temperature Measurements

A number of different tools are available for determining downhole sediment temperature (see "Physical Properties" section of the "Methods" chapter). At Site NGHP-01-05, APCT 16, the APCT–3 and the DVTP were used to measure temperatures at six subbottom depths at Site NGHP-01-05**.** Seafloor temperature was determined to be 7.1 ± 0.2 °C and the geothermal gradient was calculated as 44 ± 3 °C per km (fig. 26; table 23). The intersection of the geothermal gradient with the gas-hydrate pressure (depth) – temperature stability field from Sloan (1998) provides an estimated depth to the BGHS of ~130 mbsf for porewater with a salinity of 35 ppt and a water depth of 955 m, in close agreement with the observed BSR depth of 125 mbsf (shipboard calculated seafloor temperature 6.9 °C, geothermal gradient 46 °C per km).

Pressure Coring

The main objectives of pressure coring during NGHP Expedition 01 were to quantify natural gas composition and concentration in sediments and to determine the nature and distribution of gas hydrate and free gas within the sediment matrix. Secondary objectives were to obtain measurements of physical properties on gas-hydrate-bearing sediments under *in situ* conditions, which can be used to help interpret regional seismic data, and obtain samples under full pressure for shorebased studies. To achieve these objectives, we conducted depressurization experiments and captured resultant gas to calculate gas-hydrate quantity, made nondestructive measurements (X-ray imaging, P-wave velocity, gamma density) at *in situ* pressures and during depressurization to examine gas hydrate habit within sediments, and archived gas-hydrate-bearing sediments at *in situ* pressures for more comprehensive investigations on shore.

The BSR at Site NGHP-01-05, located in the Krishna-Godavari Basin, is a distinct reflector with an estimated depth of 125 mbsf. LWD data from Hole NGHP-01-05A showed high electrical resistivities from 70–95 mbsf (see "Downhole Logging"). High-amplitude reflections below the BSR were interpreted as possible free gas. Specific objectives at Site NGHP-01-05 were to confirm and quantify the presence of gas hydrate above the BSR, with special attention to the layer of high electrical resistivities, and predicted free gas below the BSR.

Pressure-Core Operations and Measurements

Pressure-coring tools were deployed ten times at Site NGHP-01-05 (table 24); six PCS cores (two in Hole NGHP-01-5C and four in Hole NGHP-01-05D), two FPC cores (both in Hole NGHP-01-05D), and two HRC cores (both

Table 20. Wenner array electrical resistivity results for Hole NGHP-01-05C. (To view the complete table, please see the ASCII files.)

Core, section	Sample	Top	Depth (mbsf)	Electrical resistivity (Ω.m)	Core, section	Sample	Top	Depth (mbsf)	Electrical resistivity (Ω.m)
NGHP-01-05C									
1H-1	ER	6	0.06	0.572103	3H-4	ER	60	16.9	0.429834
1H-1	ER	58	0.58	0.369294	3H-4	ER	80	17.1	0.417726
1H-1	ER	74	0.74	0.299673	3H-4	ER	100	17.3	0.472212
1H-1	ER	93	0.93	0.326916	3H-5	ER	8	17.88	0.469185
1H-1	ER	103	1.03	0.348105	3H-5	ER	30	18.1	0.472212
1H-2	ER	10	1.6	0.435888	3H-5	ER	40	18.2	0.490374
1H-2	ER	35	1.85	0.405618	3H-5	ER	60	18.4	0.457077
2H-1	ER	17	2.47	0.432861	3H-5	ER	80	18.6	0.435888
2H-1	ER	56	2.86	0.411672	3H-5	ER	101	18.81	0.435888
2H-1	ER	92	3.22	0.417726	3H-6	ER	10	19.4	0.475239
2H-2	ER	30	4.1	0.387456	3H-6	ER	30	19.6	0.481293
2H-2	ER	30	4.1	0.366267	3H-6	ER	50	19.8	0.48432
2H-2	ER	91	4.71	0.432861	3H-6	ER	70	20	0.463131
2H-2	ER	124	5.04	0.451023	3H-6	ER	90	20.2	0.475239
2H-3	ER	10	5.4	0.444969	3H-6	ER	110	20.4	0.475239
2H-3	ER	20	5.5	3.17835	3H-6	ER	130	20.6	0.45405
2H-3	ER	30	5.6	1.337934	3H-7	ER	10	20.9	0.438915
2H-3	ER	40	5.7	0.42378	3H-7	ER	10	20.9	0.535779
2H-3	ER	50	5.8	0.399564	3H-7	ER	30	21.1	0.447996
2H-3	ER	60	5.9	0.387456	3H-7	ER	50	21.3	0.475239
2H-3	ER	70	6	0.460104	4H-1	ER	10	21.4	0.48432
2H-3	ER	80	6.1	0.417726	4H-1	ER	30	21.6	0.441942
2H-3	ER	90	6.2	0.435888	4H-1	ER	50	21.8	0.475239
2H-4	ER	10	6.9	0.417726	4H-1	ER	70	22	0.411672
2H-4	ER	20	7	0.444969	4H-1	ER	90	22.2	0.432861
2H-4	ER	30	7.1	0.441942	4H-1	ER	110	22.4	0.438915
2H-4	ER	40	7.2	0.396537	4H-1	ER	130	22.6	0.460104
2H-4	ER	50	7.3	0.417726	4H-2	ER	10	22.9	0.475239
2H-4	ER	60	7.4	0.408645	4H-2	ER	30	23.1	0.511563
2H-4	ER	70	7.5	0.366267	4H-2	ER	50	23.3	0.463131
2H-4	ER	80	7.6	0.432861	4H-2	ER	70	23.5	0.429834
2H-4	ER	90	7.7	0.420753	4H-2	ER	90	23.7	0.447996
2H-4	ER	100	7.8	0.438915	4H-3	ER	10	24.4	0.487347
2H-5	ER	20	8.5	0.441942	4H-3	ER	30	24.6	0.444969
2H-5	ER	40	8.7	0.45405	4H-3	ER	50	24.8	0.444969
2H-5	ER	60	8.9	0.447996	4H-3	ER	70	25	0.541833
2H-5	ER	80	9.1	0.420753	4H-3	ER	90	25.2	0.457077
2H-6	ER	20	10	0.441942	4H-3	ER	110	25.4	0.447996
2H-6	ER	40	10.2	0.42378	4H-3	ER	130	25.6	0.490374
2H-6	ER	60	10.4	0.417726	4H-4	ER	10	25.9	0.472212
2H-6	ER	80	10.6	1.510473	4H-4	ER	10	25.9	0.472212
2H-7	ER	10	10.9	0.444969	4H-4	ER	30	26.1	0.496428
3H-1	ER	20	12	0.248214	4H-4	ER	30	26.1	0.496428
3H-1	ER	20	12	0.481293	4H-4	ER	50	26.3	0.532752
3H-1	ER	30	12.1	0.463131	4H-4	ER	50	26.3	0.532752
3H-1	ER	50	12.3	0.57513	4H-4	ER	70	26.5	0.505509
3H-1	ER	70	12.5	0.51459	4H-4	ER	70	26.5	0.505509
3H-2	ER	40	13.7	2.333817	4H-5	ER	10	27.4	0.732534
3H-2	ER	60	13.9	2.54268	4H-5	ER	30	27.6	0.517617
3H-2	ER	80	14.1	2.034144	4H-5	ER	50	27.8	0.51459
3H-2	ER	100	14.3	1.586148	4H-5	ER	50	27.8	0.51459
3H-3	ER	20	15	2.454897	4H-5	ER	70	28	0.538806
3H-3	ER	40	15.2	1.99782	4H-5	ER	70	28	0.538806
3H-3	ER	60	15.4	1.104855	4H-5	ER	90	28.2	0.511563
3H-3	ER	80	15.6	0.502482	4H-5	ER	90	28.2	0.511563
3H-3	ER	100	15.8	0.532752	4H-5	ER	110	28.4	0.529725
3H-4	ER	20	16.5	0.447996	4H-5	ER	110	28.4	0.529725
3H-4	ER	40	16.7	0.432861	4H-5	ER	130	28.6	0.48432

Table 20. Wenner array electrical resistivity results for Hole NGHP-01-05C. (To view the complete table, please see the ASCII files.)—Continued

Core, section	Sample	Top	Depth (mbsf)	Electrical resistivity (Ω.m)	Core, section	Sample	Top	Depth (mbsf)	Electrical resistivity (Ω.m)
NGHP-01-05C—Continued									
4H-5	ER	130	28.6	0.48432	6H-3	ER	90	42.71	0.551
4H-6	ER	10	28.9	3.741372	6H-4	ER	20	43.51	0.706
4H-6	ER	30	29.1	0.581184	6H-4	ER	40	43.71	0.528
4H-6	ER	50	29.3	0.523671	6H-4	ER	63	43.94	0.511
4H-6	ER	70	29.5	0.608427	6H-4	ER	83	44.14	0.549
4H-6	ER	90	29.7	0.54486	6H-4	ER	103	44.34	0.69
4H-7	ER	10	30.4	0.566049	6H-4	ER	120	44.51	0.597
4H-7	ER	30	30.6	0.584211	6H-5	ER	50	45.29	0.603
4H-7	ER	50	30.8	0.572103	6H-5	ER	70	45.49	0.68
5H-1	ER	10	30.9	0.563022	6H-6	ER	45	46.74	0.578
5H-1	ER	30	31.1	0.517617	6H-7	ER	20	47.99	0.555
5H-1	ER	50	31.3	0.541833	6H-7	ER	60	48.39	0.655
5H-1	ER	70	31.5	0.541833	6H-8	ER	40	49.66	1.14
5H-1	ER	90	31.7	0.587238	7H-1	ER	7	49.87	0.814
5H-1	ER	110	31.9	0.535779	7H-1	ER	19	49.99	0.673
5H-2	ER	10	32.25	0.572103	7H-1	ER	42	50.22	0.796
5H-2	ER	30	32.45	0.517617	7H-1	ER	68	50.48	0.702
5H-2	ER	50	32.65	0.965613	7H-1	ER	90	50.7	0.568
5H-2	ER	70	32.85	0.572103	7H-2	ER	43	51.65	0.641
5H-2	ER	90	33.05	0.54486	7H-2	ER	60	51.82	0.65
5H-3	ER	10	33.75	3.468	7H-2	ER	65	51.87	0.61
5H-3	ER	30	33.95	1.285	7H-3	ER	35	53.07	0.653
5H-3	ER	49	34.14	1.947	7H-3	ER	70	53.42	0.827
5H-3	ER	70	34.35	0.911	7H-3	ER	102	53.74	0.729
5H-3	ER	90	34.55	3.798	7H-3	ER	131	54.03	0.971
5H-3	ER	110	34.75	0.844	7H-4	ER	20	54.42	0.7
5H-3	ER	132	34.97	2.983	7H-4	ER	55	54.77	0.647
5H-4	ER	8	35.23	0.86	7H-4	ER	105	55.27	0.719
5H-4	ER	28	35.43	0.844	7H-5	ER	20	55.92	0.644
5H-4	ER	48	35.63	1.873	7H-5	ER	40	56.12	0.614
5H-4	ER	72	35.87	1.504	7H-5	ER	60	56.32	0.669
5H-5	ER	10	36.69	2.078	7H-5	ER	80	56.52	0.705
5H-5	ER	32	36.91	1.132	7H-6	ER	45	57.67	0.66
5H-5	ER	52	37.11	0.681	7H-6	ER	110	58.32	0.782
5H-5	ER	72	37.31	0.871	8H-1	ER	20	59.5	0.486
5H-5	ER	92	37.51	0.585	8H-1	ER	40	59.7	0.522
5H-5	ER	112	37.71	0.624	8H-1	ER	70	60	0.474
5H-5	ER	132	37.91	0.655	8H-1	ER	95	60.25	0.51
5H-6	ER	13	38.22	2.542	8H-1	ER	115	60.45	0.463
5H-6	ER	33	38.42	2.287	8H-2	ER	25	61.05	0.471
5H-6	ER	53	38.62	1.942	8H-2	ER	40	61.2	0.502
5H-6	ER	73	38.82	3.527	8H-2	ER	55	61.35	0.441
5H-6	ER	89	38.98	2.637	8H-3	ER	40	62.7	0.509
5H-7	ER	19	39.76	0.66	8H-3	ER	78	63.08	0.491
5H-7	ER	39	39.96	0.647	8H-3	ER	130	63.6	0.569
5H-7	ER	59	40.16	0.535	8H-4	ER	40	64.2	0.595
6H-1	ER	10	40.4	0.67	8H-4	ER	85	64.65	0.56
6H-1	ER	20	40.5	0.748	8H-4	ER	110	64.9	0.557
6H-2	ER	10	40.74	0.656	8H-5	ER	54	65.84	0.542
6H-2	ER	35	40.99	0.612	8H-5	ER	79	66.09	0.585
6H-2	ER	55	41.19	0.594	8H-6	ER	20	67	0.55
6H-2	ER	75	41.39	0.525	8H-7	ER	27	67.58	0.652
6H-2	ER	95	41.59	0.557	8H-7	ER	27	67.58	0.543
6H-3	ER	10	41.91	0.689	9H-1	ER	12	68.92	4.204
6H-3	ER	30	42.11	0.524	9H-1	ER	25	69.05	4.917
6H-3	ER	50	42.31	0.699	9H-1	ER	35	69.15	2.23
6H-3	ER	70	42.51	0.493	9H-1	ER	44	69.24	2.367

Table 20. Wenner array electrical resistivity results for Hole NGHP-01-05C. (To view the complete table, please see the ASCII files.)—Continued

Core, section	Sample	Top	Depth (mbsf)	Electrical resistivity (Ω.m)	Core, section	Sample	Top	Depth (mbsf)	Electrical resistivity (Ω.m)
NGHP-01-05C—Continued									
9H-2	ER	20	69.6	3.524	15X-2	ER	60	108.3	0.61
9H-2	ER	40	69.8	2.692	15X-2	ER	80	108.5	0.734
9H-3	ER	20	70.68	4.506	15X-2	ER	100	108.7	0.607
9H-3	ER	40	70.88	2.038	15X-2	ER	114	108.84	0.803
9H-3	ER	80	71.28	1.929	15X-3	ER	15	109.35	0.637
9H-3	ER	100	71.48	1.708	15X-3	ER	31	109.51	0.709
9H-3	ER	120	71.68	1.061	15X-3	ER	54	109.74	0.642
9H-4	ER	17	72.08	0.598	15X-3	ER	75	109.95	0.698
9H-4	ER	67	72.58	0.556	15X-3	ER	90	110.1	0.672
9H-4	ER	87	72.78	0.573	15X-4	ER	15	110.85	0.675
9H-4	ER	107	72.98	0.551	15X-4	ER	35	111.05	0.76
9H-5	ER	20	73.61	0.532	15X-4	ER	55	111.25	0.616
9H-5	ER	40	73.81	0.516	15X-4	ER	71	111.41	0.609
9H-5	ER	60	74.01	0.68	16X-1	ER	10	115.9	0.457
9H-5	ER	80	74.21	0.516	16X-1	ER	34	116.14	0.597
9H-5	ER	100	74.41	0.541	16X-1	ER	50	116.3	0.521
9H-6	ER	20	75.11	0.527	16X-1	ER	60	116.4	0.586
9H-6	ER	65	75.56	0.559	17X-1	ER	20	125.7	0.651
9H-6	ER	85	75.76	0.766	17X-1	ER	40	125.9	0.601
9H-6	ER	120	76.11	0.63	17X-1	ER	60	126.1	0.61
9H-7	ER	21	76.62	0.535	17X-1	ER	80	126.3	0.546
9H-7	ER	41	76.82	0.683	17X-1	ER	100	126.5	0.525
9H-8	ER	10	77.08	0.585	17X-1	ER	120	126.7	0.52
9H-8	ER	38	77.36	0.693	17X-1	ER	140	126.9	0.568
9H-8	ER	58	77.56	0.724	17X-2	ER	20	127.2	1.705
9H-8	ER	78	77.76	0.663	17X-2	ER	40	127.4	1.065
11X-1	ER	38	79.68	0.518	17X-2	ER	60	127.6	0.75
13X-1	ER	6	87.06	0.63	17X-2	ER	80	127.8	1.57
13X-1	ER	28	87.28	0.577	17X-3	ER	20	128.7	2.291
13X-1	ER	49	87.49	0.878	17X-3	ER	40	128.9	2.185
13X-2	ER	23	88.53	0.633	17X-3	ER	60	129.1	2.335
13X-2	ER	40	88.7	0.613	17X-3	ER	80	129.3	2.787
13X-3	ER	26	89.16	0.602	17X-3	ER	100	129.5	2.911
13X-3	ER	46	89.36	0.775	17X-3	ER	120	129.7	2.66
13X-3	ER	66	89.56	0.694	17X-3	ER	140	129.9	2.053
13X-3	ER	82	89.72	0.74	17X-4	ER	20	130.2	3.447
13X-4	ER	6	90.46	0.622	17X-4	ER	40	130.4	2.293
13X-4	ER	26	90.66	0.833	17X-4	ER	63	130.63	2.122
13X-4	ER	46	90.86	0.693	17X-4	ER	80	130.8	2.287
13X-4	ER	66	91.06	0.734	17X-4	ER	100	131	2.271
13X-4	ER	86	91.26	0.772	17X-4	ER	115	131.15	1.932
13X-4	ER	105	91.45	0.583	17X-5	ER	10	131.6	0.429
14X-1	ER	4	96.94	0.612	17X-5	ER	35	131.85	0.712
14X-1	ER	26	97.16	0.682	17X-5	ER	50	132	0.607
14X-1	ER	46	97.36	0.702	17X-5	ER	60	132.1	0.574
14X-1	ER	71	97.61	0.83	17X-5	ER	70	132.2	0.587
14X-2	ER	13	98.53	0.617	17X-5	ER	90	132.4	0.453
14X-3	ER	6	98.75	0.631	18X-1	ER	28	135.38	0.711
14X-3	ER	26	98.95	1.061	18X-1	ER	45	135.55	0.859
14X-3	ER	33	99.02	0.63	18X-1	ER	65	135.75	0.774
15X-1	ER	67	106.87	0.737	18X-2	ER	20	136.8	0.614
15X-1	ER	80	107	0.662	18X-2	ER	40	137	0.638
15X-2	ER	20	107.9	0.596	18X-2	ER	60	137.2	0.399
15X-2	ER	40	108.1	0.697	18X-2	ER	80	137.4	0.512

Table 20. Wenner array electrical resistivity results for Hole NGHP-01-05C. (To view the complete table, please see the ASCII files.) —Continued

Core, section	Sample	Top	Depth (mbsf)	Electrical resistivity (Ω.m)	Core, section	Sample	Top	Depth (mbsf)	Electrical resistivity (Ω.m)
NGHP-01-05C—Continued									
18X-2	ER	102	137.62	0.387	21X-1	ER	29	164.19	6.556482
18X-2	ER	120	137.8	0.439	21X-1	ER	55	164.45	4.325583
18X-2	ER	140	138	0.453	21X-1	ER	85	164.75	4.004721
18X-3	ER	20	138.3	0.297	21X-1	ER	115	165.05	5.230656
18X-3	ER	38.5	138.485	0.359	21X-2	ER	40	165.8	6.17508
18X-3	ER	53	138.63	0.287	21X-3	ER	20	167.1	4.080396
18X-3	ER	73	138.83	0.307	21X-3	ER	45	167.35	3.235863
19X-1	ER	25	144.95	0.732534	21X-3	ER	60	167.5	3.916938
19X-1	ER	45	145.15	0.771885	21X-3	ER	80	167.7	3.590022
19X-1	ER	66	145.36	0.69621	21X-3	ER	100	167.9	5.088387
19X-1	ER	85	145.55	0.644751	22X-1	ER	20	173.7	0.451023
19X-1	ER	105	145.75	0.647778	22X-1	ER	40	173.9	0.466158
19X-1	ER	123	145.93	0.723453	22X-1	ER	90	174.4	0.502482
19X-2	ER	20	146.4	0.681075	22X-1	ER	110	174.6	0.438915
19X-2	ER	42	146.62	0.632643	22X-2	ER	20	175.2	0.429834
19X-2	ER	60	146.8	0.556968	22X-2	ER	40	175.4	0.466158
19X-2	ER	80	147	0.638697	22X-2	ER	60	175.6	0.451023
19X-2	ER	100	147.2	0.505509	22X-2	ER	80	175.8	0.460104
19X-2	ER	119	147.39	0.535779	22X-2	ER	100	176	0.441942
19X-3	ER	20	147.9	0.563022	22X-2	ER	130	176.3	0.429834
19X-3	ER	39	148.09	0.584211	22X-3	ER	20	176.7	0.420753
19X-3	ER	63	148.33	0.493401	22X-3	ER	40	176.9	0.42378
19X-3	ER	82	148.52	0.57513	22X-3	ER	60	177.1	0.426807
19X-3	ER	100	148.7	0.499455	22X-4	ER	20	178.2	0.469185
19X-3	ER	120	148.9	0.517617	22X-4	ER	40	178.4	0.432861
19X-3	ER	139	149.09	0.563022	22X-4	ER	60	178.6	0.414699
19X-4	ER	20	149.4	0.523671	23X-1	ER	20	183.3	0.469185
19X-4	ER	40	149.6	0.523671	23X-1	ER	20	183.3	0.408645
19X-4	ER	60	149.8	0.520644	23X-1	ER	40	183.5	0.499455
19X-4	ER	75	149.95	0.596319	23X-1	ER	40	183.5	0.429834
19X-5	ER	20	151	0.578157	23X-1	ER	60	183.7	0.457077
19X-5	ER	40	151.2	0.496428	23X-1	ER	64	183.74	0.523671
19X-5	ER	60	151.4	0.511563	23X-1	ER	80	183.9	0.426807
19X-5	ER	80	151.6	0.511563	23X-1	ER	84	183.94	0.408645
19X-5	ER	100	151.8	0.572103	23X-1	ER	100	184.1	0.463131
19X-5	ER	120	152	0.547887	23X-1	ER	120	184.3	0.481293
19X-6	ER	10	152.3	0.584211	23X-1	ER	140	184.5	0.463131
19X-6	ER	22	152.42	0.502482	23X-3	ER	22	186.32	0.447996
20X-1	ER	20	154.5	0.532752	24X-1	ER	20	192.9	3.14808
20X-1	ER	40	154.7	0.547887	24X-1	ER	40	193.1	1.928199
20X-1	ER	60	154.9	0.529725	24X-1	ER	60	193.3	2.037171
20X-1	ER	80	155.1	0.559995	24X-1	ER	80	193.5	1.93728
20X-1	ER	124	155.54	0.569076	24X-1	ER	100	193.7	1.57404
20X-2	ER	20	156	0.475239	24X-1	ER	120	193.9	1.988739
20X-2	ER	40	156.2	0.441942	24X-2	ER	20	194.4	1.773822
20X-2	ER	60	156.4	0.490374	24X-2	ER	40	194.6	1.63458
20X-2	ER	80	156.6	0.496428	24X-2	ER	60	194.8	1.443879
20X-2	ER	115	156.95	0.469185	24X-3	ER	20	195.9	2.019009
20X-3	ER	20	157.5	0.526698	24X-3	ER	40	196.1	1.265286
20X-3	ER	40	157.7	0.517617	24X-3	ER	60	196.3	1.047342
20X-3	ER	60	157.9	0.499455	24X-3	ER	80	196.5	1.065504
20X-4	ER	20	159	0.493401	24X-3	ER	100	196.7	0.932316
20X-4	ER	40	159.2	0.45405	24X-3	ER	130	197	0.656859
20X-4	ER	60	159.4	0.45405	24X-5	ER	30	198.5	0.747669

Table 21. Contact P-wave velocity results determined on split cores sections from Hole NGHP-01-05C.

Core, section	Sample	Top	Depth (mbsf)	Temp (°C)	VP (km/s)	Comment
			NGHP-01-05C			
1H-1	VP	100	1	22.16	1.501	
1H-2	VP	32	1.82	24.49	1.507	
2H-1	VP	63	2.93	25.28	1.509	
2H-2	VP	77	4.57	26.17	1.498	
2H-3	VP	71	6.01	25.11	1.514	
2H-4	VP	79	7.59	25.27	1.486	
2H-5	VP	75	9.05	25.09	1.527	
2H-6	VP	68	10.5	25.42	1.437	
2H-7	VP	10	10.9	24.51	1.522	
3H-1	VP	66	12.5	24.5	1.509	
3H-2	VP	79	14.1	24.9	1.519	
3H-3	VP	60	15.4	24.51	1.535	
3H-4	VP	40	16.7	25.43	1.540	
3H-5	VP	30	18.1	0	1.540	No temperature correction
3H-7	VP	20	21.0	0	1.558	No temperature correction
4H-1	VP	40	21.7	24.6	1.540	
4H-2	VP	35	23.2	25.6	1.539	

Table 22. Thermal conductivity results for Hole NGHP-01-05C.

Section, core	Sample	Top	Depth (mbsf)	Tcon value
		NGHP-01-05C		
1H-2	TC	75	2.25	0.844
2H-3	TC	75	6.05	0.8855
3H-3	TC	75	15.55	0.9495
4H-3	TC	75	25.05	0.92225
5H-3	TC	75	34.4	0.82325
6H-3	TC	61	42.42	0.9935
7H-3	TC	73	53.45	0.6285
8H-3	TC	70	63	0.88325
9H-3	TC	75	71.23	0.7895
11X-1	TC	40	79.7	0.8805
13X-3	TC	46	89.36	0.8285
14X-3	TC	17	98.86	0.68975
15X-3	TC	50	109.7	0.80825
16X-1	TC	34	116.14	0.8135
16X-1	TC	34	116.14	0.77225
17X-3	TC	75	129.25	0.75975
18X-2	TC	75	137.35	0.69425
19X-3	TC	75	148.45	0.76175
20X-3	TC	35	157.65	0.65425
21X-3	TC	70	167.6	0.64425
22X-3	TC	43	176.93	0.8015
23X-2	TC	75	185.35	0.84925
24X-3	TC	75	196.45	0.9085

in Hole NGHP-01-05D). Figures 27 and 28 show the pressure and temperature history of the cores during deployment, coring, recovery, and chilling (in the ice shuck) of the pressure coring tools. Figures 29, 30, and 31 show the measurements made on the six successful cores at full pressure and during depressurization. Figures 32 and 33 show the gas and fluid released from the successful cores and the character of the pressure decrease during depressurization.

Core NGHP-01-05C-10P, collected in the zone of high electrical resistivity (79.3 mbsf), retrieved a partial core (0.36 m) under pressure (table 24). This core was collected before nondestructive measurements could be made on PCS cores, so no X-ray images or gamma density profiles were collected either before or after depressurization. Core NGHP-01-05C-10P was depressurized and released 0.93 liters of methane, corresponding to 0.6 percent methane hydrate as a percent of pore volume (table 25). No chlorinity measurements were made on this core.

Core NGHP-01-05C-12P, collected in the zone of high electrical resistivity (87.0 mbsf), retrieved a full core (1.00 m) under pressure (table 24). Core NGHP-01-05C-12P was x rayed before depressurization, showing a 1-cm low-density zone (fig. 29). This core released 3.06 liters of methane, corresponding to 0.9 percent methane hydrate as a percent of pore volume or 1.8 mL of gas hydrate, similar in volume to the low density zone (table 25). Core NGHP-01-05C-12P had no nondestructive measurements made on it after depressurization. No chlorinity measurements were made on this core.

Core NGHP-01-05D-06P, collected in the zone of high electrical resistivity (76.9 mbsf), retrieved a full core (0.98 m) under full *in situ* pressure (table 24). This core showed an increase in pressure as it warmed during handling on deck, indicating minor gas-hydrate dissociation, before being placed in the ice shuck, and it spent longer outside the gas-hydrate stability zone than most cores did as the ice shuck had not been filled recently. Core NGHP-01-05D-06P was x rayed before depressurization and showed wispy, low-density structures that were interpreted as gas-hydrate veins (fig. 29B). The core was depressurized, releasing 14.98 liters of methane, corresponding to 78.8 mL of methane hydrate or methane hydrate occupation of 9.4 percent of pore volume (table 25). Core NGHP-01-05D-06P showed pressure rebounds and a pressure-volume plateau near 30 bar pressure (figs. 32 and 33), indicating gas-hydrate disassociation at 2 °C (laboratory temperature). A final X-ray image was collected at atmospheric pressure with the outer barrel removed (fig. 29B). One chlorinity measurement was made on this core (16–26 cm, 535 mM), which was fresher than measurements made in Hole NHGP-01-05C at comparable depths (566 & 557 mM; see “Inorganic Geochemistry”).

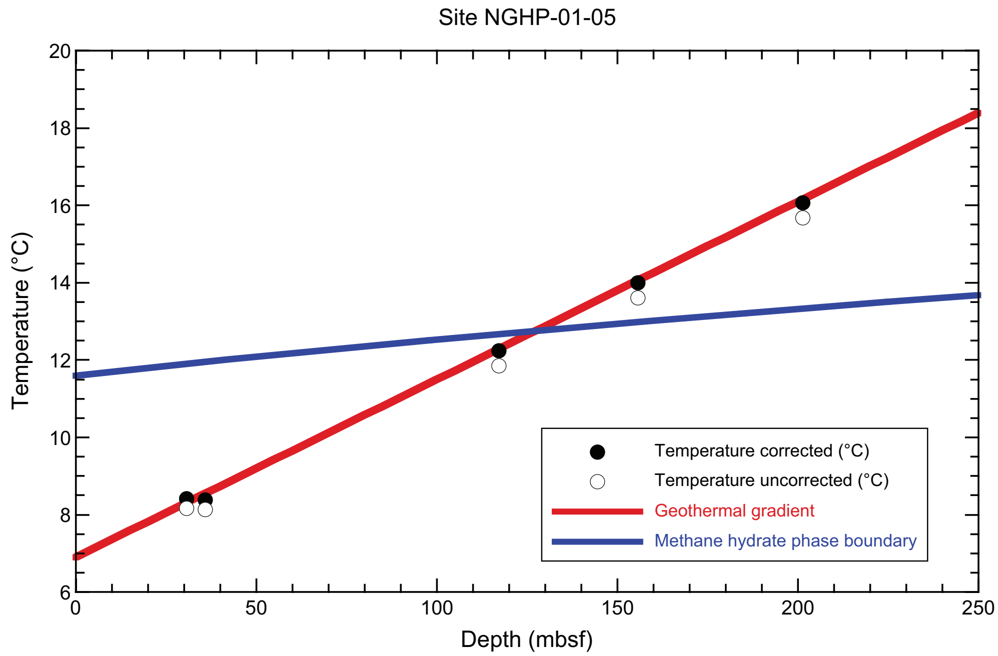

Figure 26. Geothermal gradient and estimated depth to the BSR from *in situ* temperature measurements. [BSR, bottom-simulating reflector]

Table 23. *In situ* temperature estimates from Site NGHP-01-05.

Depth (mbsf)	Core	Assumed thermal conductivity (W/[m×K])	Tool	Ad-hoc calibration correction	Temperature (°C)	Corrected temperature (°C)	Estimated uncertainty	Data quality
21.3	C03	0.95	APCT-3	0	NA	NA	NA	poor
30.8	C04	0.95	APCT16	0.45	8.16	8.61	0.05	excellent
35.9	D04	0.95	APCT16	0.45	8.13	8.58	0.05	excellent
117.2	C16X	0.95	DVTP	0.5	11.85	12.35	0.1	good
155.7	C20X	0.95	DVTP	0.5	13.61	14.11	0.1	good
201.4	C24X	0.95	DVTP	0.5	15.68	16.18	0.1	good

Table 24. Summary of pressure coring operations at Site NGHP-01-05.

Core ID	Top of core (mbsf)	Length recovered (cm)*	Length curated (cm)*	Pressure at core depth (bar)	Pressure recovered (bar)		Comments
					logged**	gauge***	
				NGHP-01-05C			
10P	79.3	--	36	104	67	29	normal operation
12P	87.0	100	85	105	78	48	normal operation
				NGHP-01-05D			
05P	44.9	--	0	101	0	--	failed to actuate
06P	76.9	98	100	104	100	41	normal operation
07Y	84.9	86	89	105	110	110	normal operation
08E	88.9	--	24	105	0	--	stuck in BHA; no pressure
09P	92.9	--	0	105	0	--	failed to actuate
10E	114.9	42	55	108	104	104	normal operation
11Y	124.9	90	89	109	96	96	stuck in transfer system & depressurized without logging
12P	200.0	100	100	116	14	7	did not seal until nearly at rig floor

Notes:

Water depth at Site NGHP-01-05 is 957 m. P = PCS, Y = FPC, E = HRC.

*Length measured from X-ray and gamma density analysis, which may not match curated core length.

**Last pressure recorded before data logger disconnected from corer autoclave. Temperature 2–4 °C unless otherwise noted.

***Pressure measured when autoclave pressure transducer connected to external gauge. Pressure measured at 7 °C unless otherwise noted.

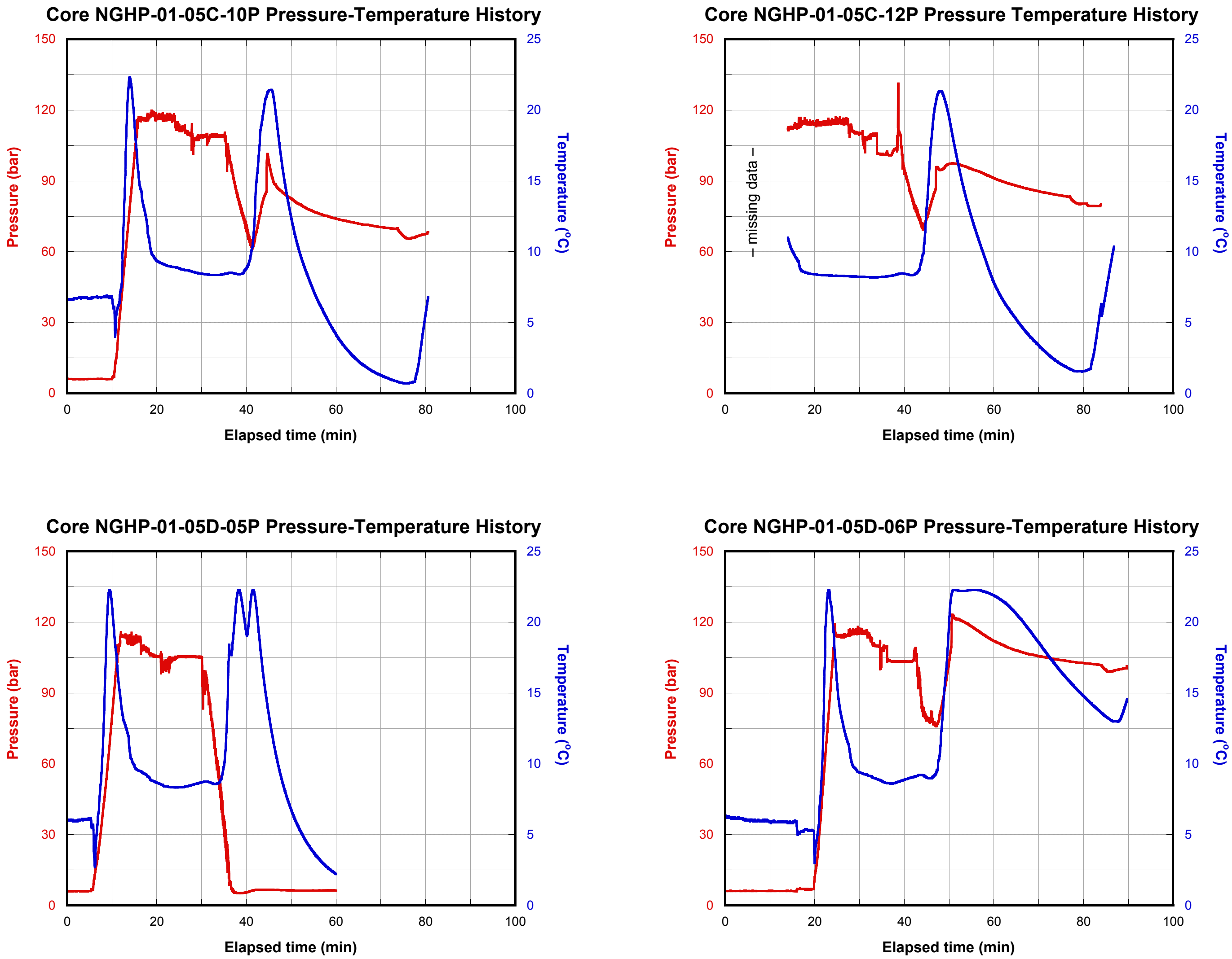

Figure 27. Temperature and pressure versus elapsed time for each pressure corer deployment as recorded by the corer's internal data logger. There are no data for Core NGHP-01-05D-10E. Core NGHP-01-05C-12P is missing data at the beginning of the deployment.

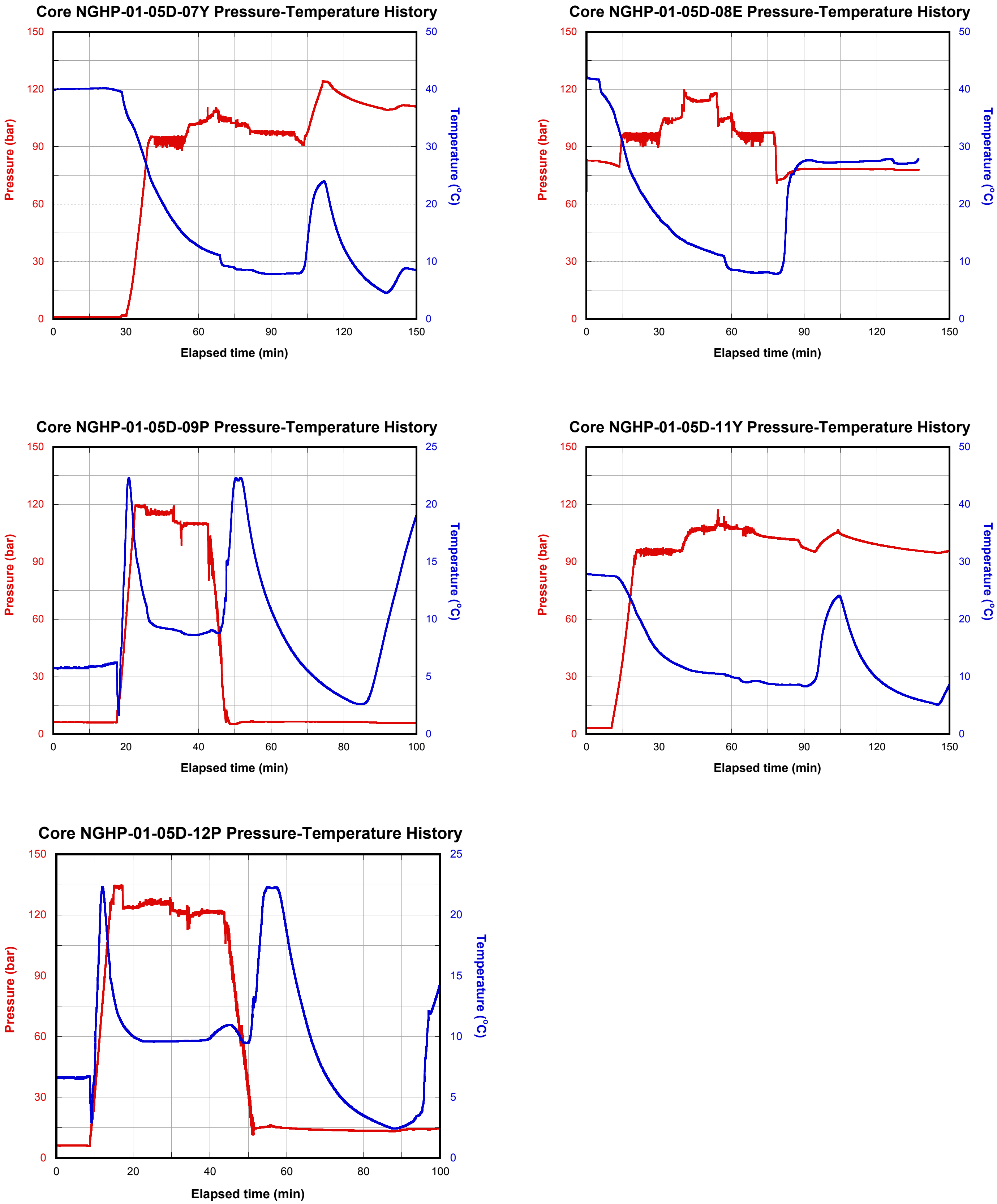

Figure 27. Temperature and pressure versus elapsed time for each pressure corer deployment as recorded by the corer's internal data logger. There are no data for Core NGHP-01-05D-10E. Core NGHP-01-05C-12P is missing data at the beginning of the deployment.—Continued

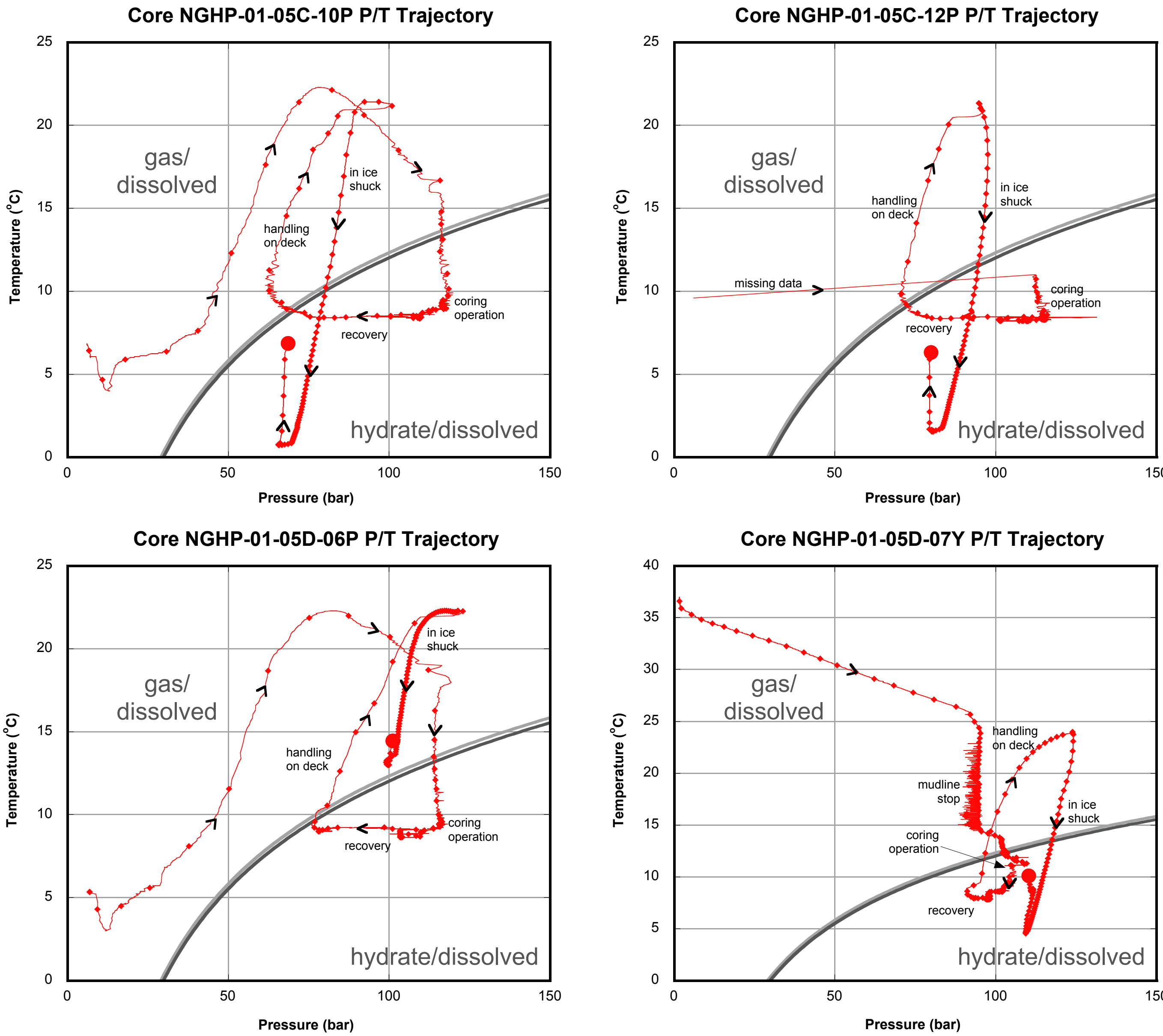

Figure 28. Temperature versus pressure for each successful pressure corer deployment, showing trajectories relative to gas hydrate stability at 35 ppt and 30 ppt salinity, calculated from Xu (2002, 2004). Small dots are every half-minute. Large dot is final temperature and pressure of autoclave prior to data logger removal. There is no data for Core NGHP-01-05D-10E. Core NGHP-01-05C-12P is missing data at the beginning of the deployment. Core NGHP-01-05D-12P is also shown, though it was not considered a successful pressure core. [ppt, parts per thousand]

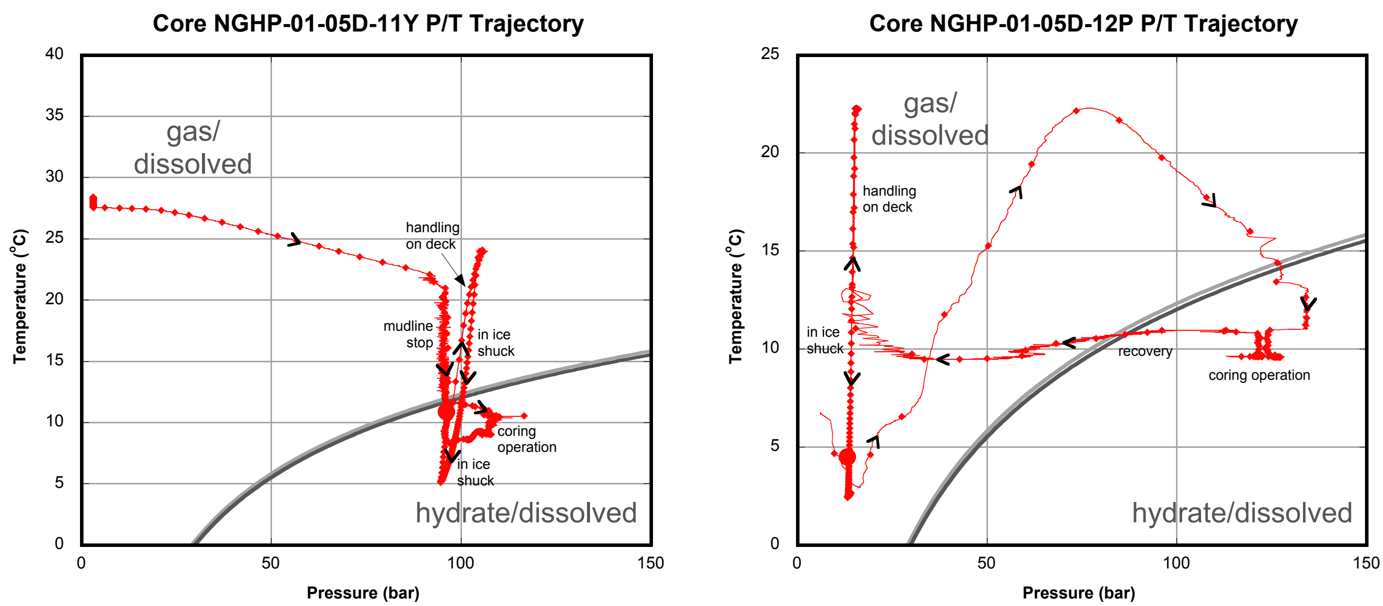

Figure 28. Temperature versus pressure for each successful pressure corer deployment, showing trajectories relative to gas hydrate stability at 35 ppt and 30 ppt salinity, calculated from Xu (2002, 2004). Small dots are every half-minute. Large dot is final temperature and pressure of autoclave prior to data logger removal. There is no data for Core NGHP-01-05D-10E. Core NGHP-01-05C-12P is missing data at the beginning of the deployment. Core NGHP-01-05D-12P is also shown, though it was not considered a successful pressure core. [ppt, parts per thousand]—Continued

Core NGHP-01-05D-07Y, collected in the zone of high electrical resistivity (84.9 mbsf), retrieved a full core (0.90m) under full *in situ* pressure (table 24). This core showed an increase in pressure as it warmed during handling on deck, indicating minor gas-hydrate dissociation, before being placed in the ice shuck. Core NGHP-01-05D-07Y was transferred to the MSCL–P and X-ray images, gamma density and P-wave velocity measurements were collected, showing a highly stratified core with a single high-velocity, low-density layer of presumed gas hydrate, 5 mm thick (fig. 30A). The core was depressurized in the MSCL–P, releasing 14.39 liters of methane, and showed pressure rebounds and a pressure-volume plateau near 60 bar pressure (figs. 32B and 33), indicating gas-hydrate disassociation at 7 °C (laboratory temperature). Pressure was inadvertently lost between 40 bar and 20 bar; about five liters of gas were estimated as uncollected, using the relationship between previously-released fluid and gas remaining within the system (see “Pressure coring” in the “Methods” chapter). Twenty liters of released methane would correspond to 8.0 percent methane hydrate as a percent of pore volume, or 102.8 mL of methane hydrate (table 25). One intermediate MSCL–P scan was made at 38 bar and a final scan MSCL-P scan was collected at atmospheric pressure (fig. 31A). The structure of the core was well-preserved upon splitting. No chlorinity measurements were made on this core.

Core NGHP-01-05D-10E, collected below the zone of high electrical resistivity but above the BSR (114.9 mbsf), retrieved a partial core (0.42 m) under full *in situ* pressure (table 24). No data were collected during the coring operation for Core NGHP-01-05D-10E. This core was transferred to the MSCL–P and X-ray images, gamma density and P-wave velocity measurements were collected, showing no evidence of gas-hydrate structures (fig. 30B). Core NGHP-01-05D-10E was depressurized and released 1.73 liters of methane, corresponding to 1.0 percent methane hydrate as a percent of pore volume (table 25). A final MSCL–P scan was collected at atmospheric pressure (fig. 31B). No chlorinity measurements were made on this core.

Core NGHP-01-05D-11Y, which targeted the BSR (124.9 mbsf), retrieved a full core (0.90 m) under full *in situ* pressure (table 24). This core could not be transferred to the MSCL–P, as the pawls became stuck in the transfer system, and the core had to be depressurized in the transfer system without any measurements at full pressure. Core NGHP-01-05D-11Y was depressurized and released 4.25 liters of methane, corresponding to 0.6 percent methane hydrate as a percent of pore volume (table 25). One chlorinity measurement was made on this core (70–80 cm, 565 mM), which was higher than measurements made in Hole NHGP-01-05C at comparable depths (527 and 519 mM; see “Inorganic Geochemistry”).

Core NGHP-01-05D-12P was targeted at potential free gas below the BSR (200.0 mbsf) and some data were collected on this core (for example, depressurization data, x rays). However, later analysis of the data logger showed that the corer had not sealed until it was retrieved to the deck, and therefore the depressurization data are not suitable for mass balance calculations of methane concentration.

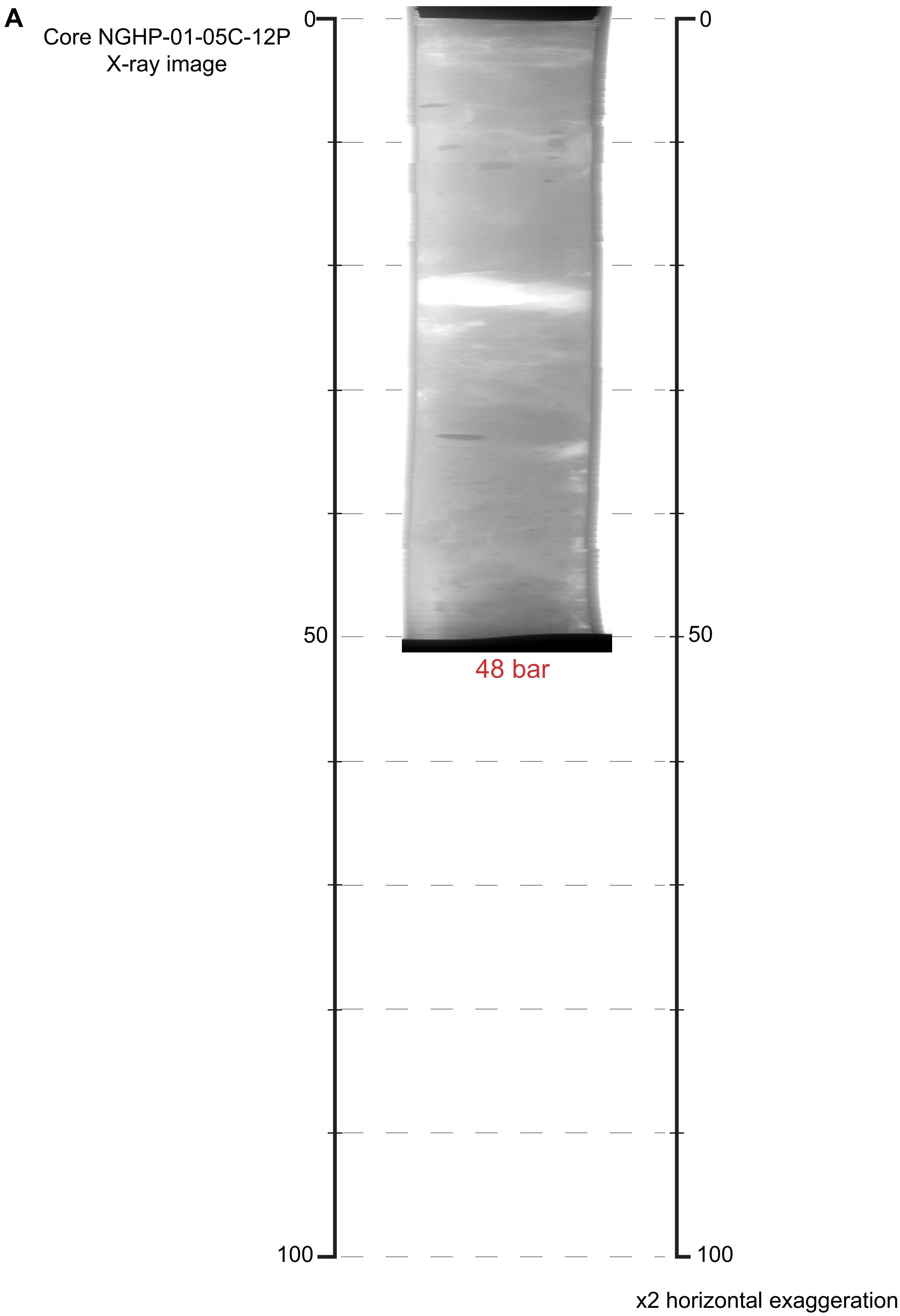

Figure 29. X-ray images of Cores NGHP-01-05C-12P, NGHP-01-05D-06P, and NGHP-01-05D-12P at full corer pressure and at atmospheric pressure. X-ray images have been stretched 200 percent in the cross-core direction to show detail. There is no image at atmospheric pressure for Core NGHP-01-05C-12P.

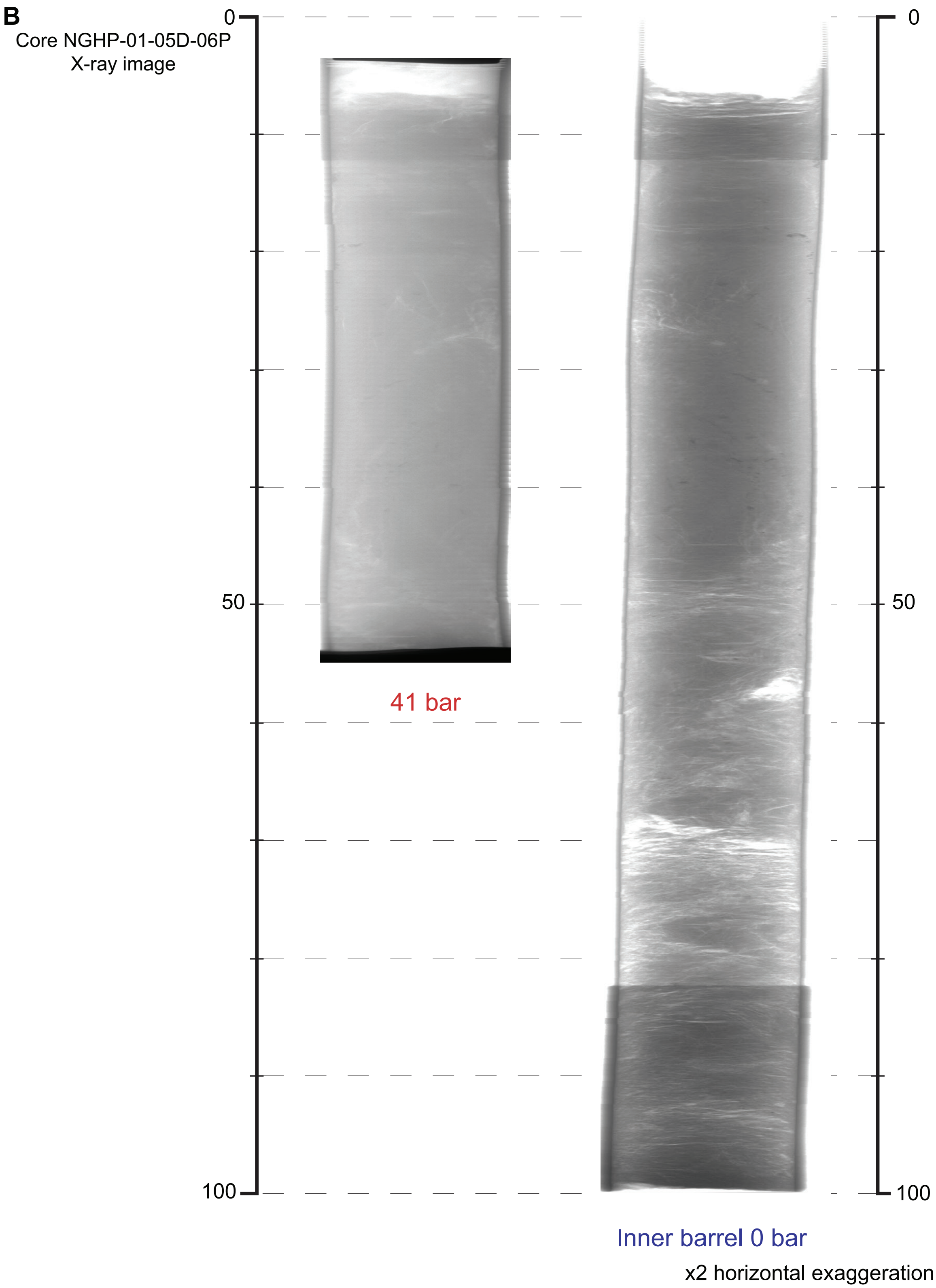

Figure 29. X-ray images of Cores NGHP-01-05C-12P, NGHP-01-05D-06P, and NGHP-01-05D-12P at full corer pressure and at atmospheric pressure. X-ray images have been stretched 200 percent in the cross-core direction to show detail. There is no image at atmospheric pressure for Core NGHP-01-05C-12P.—Continued

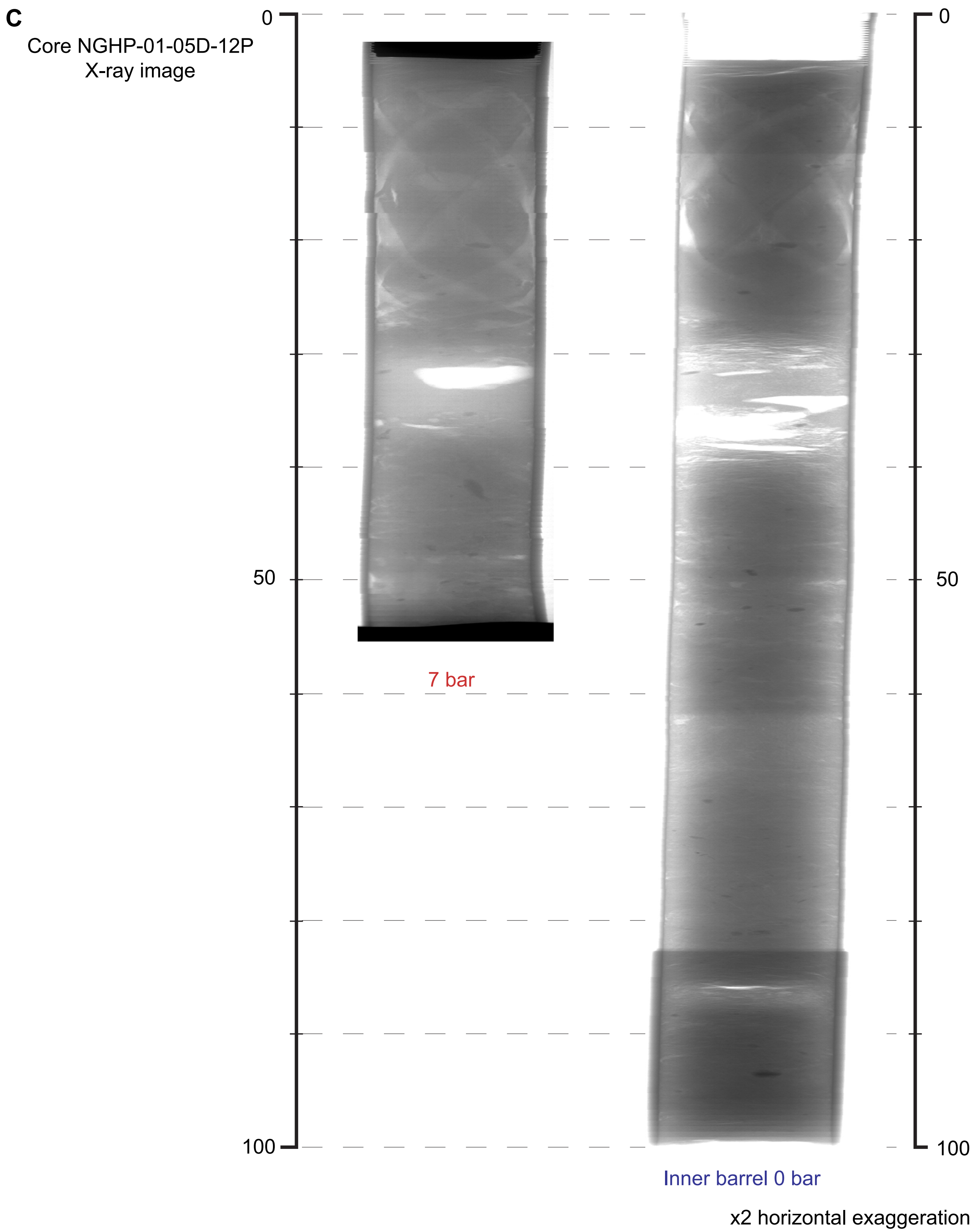

Figure 29. X-ray images of Cores NGHP-01-05C-12P, NGHP-01-05D-06P, and NGHP-01-05D-12P at full corer pressure and at atmospheric pressure. X-ray images have been stretched 200 percent in the cross-core direction to show detail. There is no image at atmospheric pressure for Core NGHP-01-05C-12P.—Continued

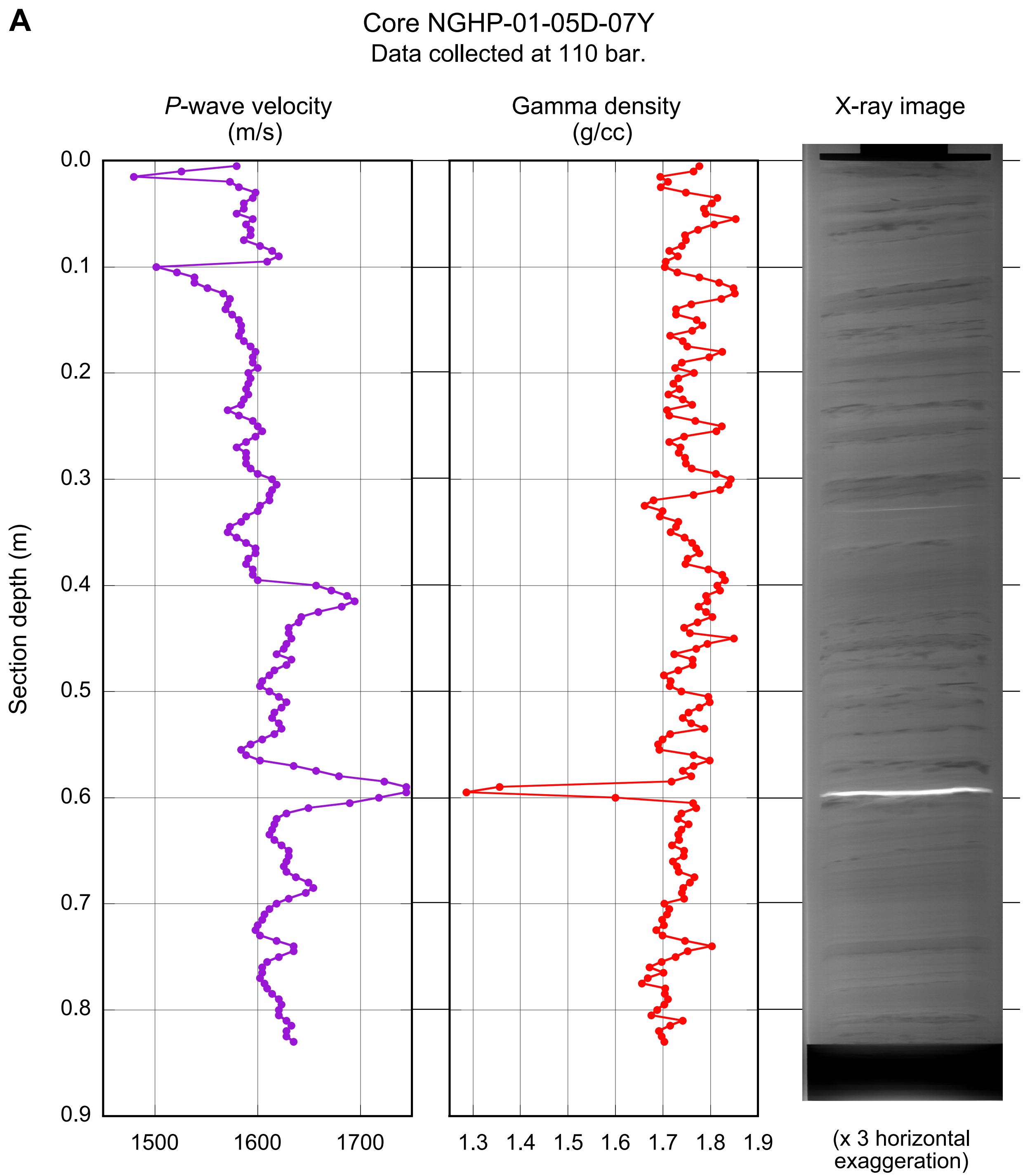

Figure 30. Data collected at near *in situ* pressure and 7 °C for Cores NGHP-01-05D-07Y and NGHP-01-05D-10E, including X-ray images, gamma density, and *P*-wave velocity. X-ray images have been stretched 300 percent in the cross-core direction to show detail.

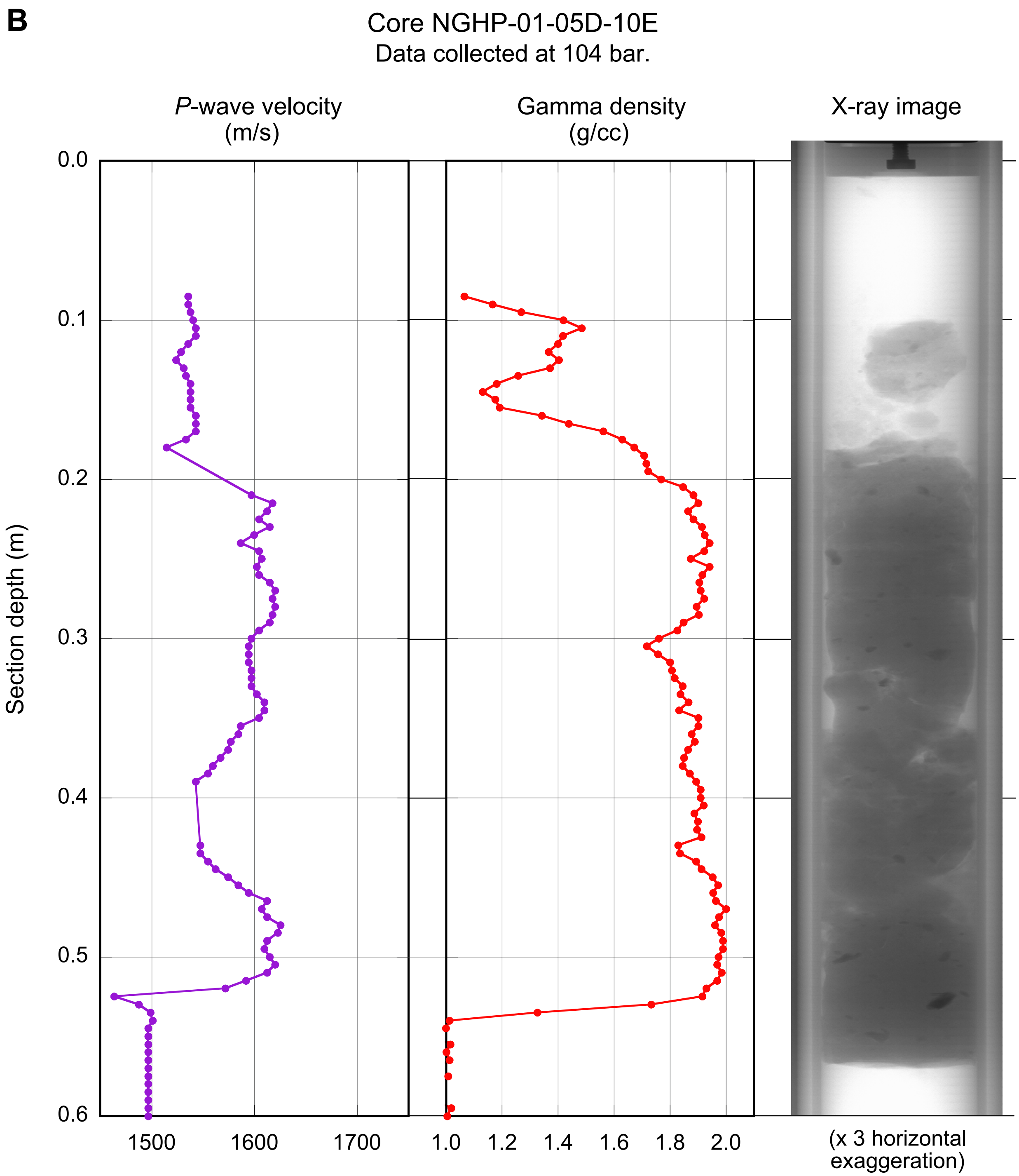

Figure 30. Data collected at near *in situ* pressure and 7 °C for Cores NGHP-01-05D-07Y and NGHP-01-05D-10E, including X-ray images, gamma density, and *P*-wave velocity. X-ray images have been stretched 300 percent in the cross-core direction to show detail.—Continued

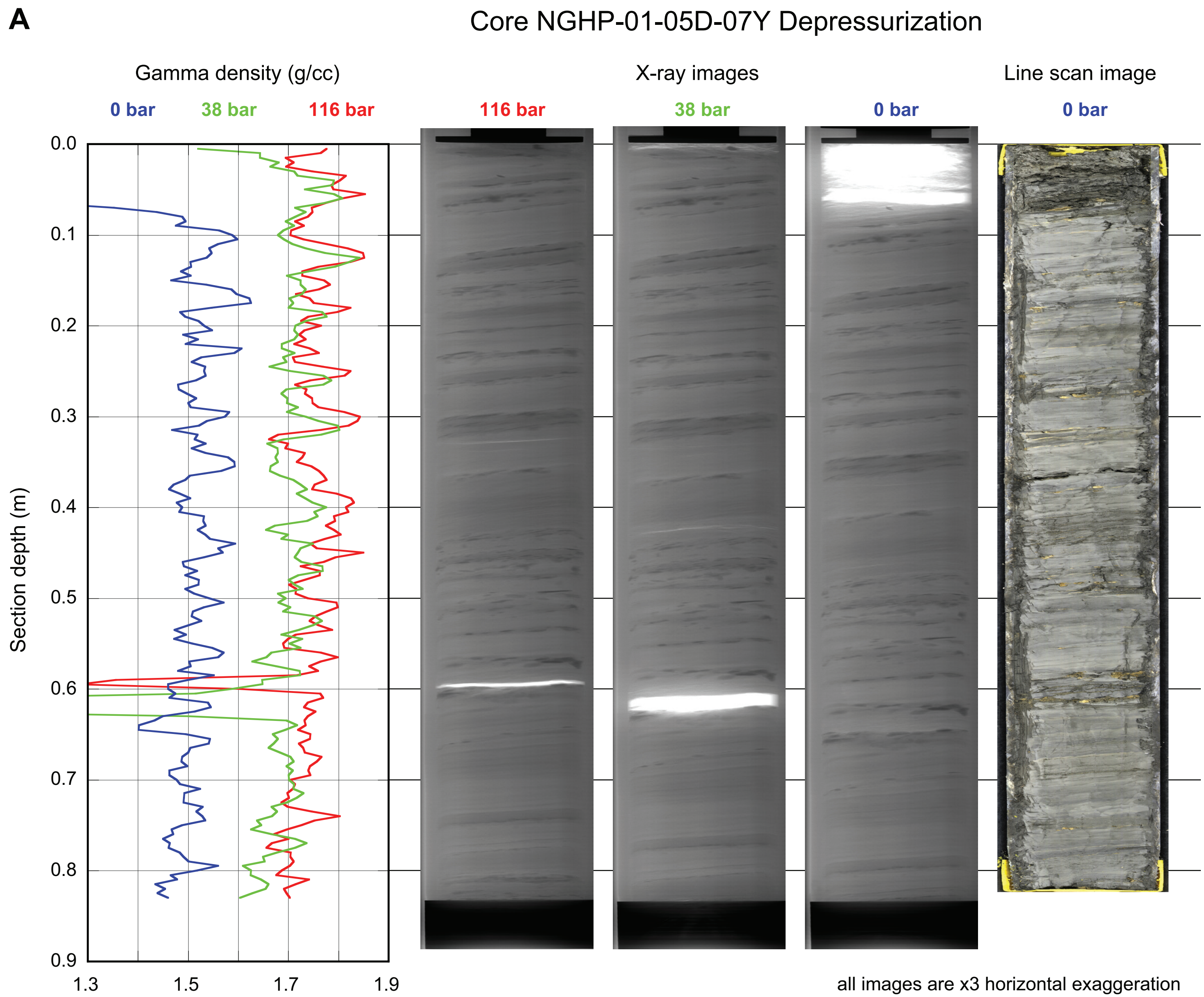

Figure 31. Summary of data taken from Cores NGHP-01-05D-07Y and NGHP-01-05D-10E before, during, and after depressurization, including gamma density profiles collected before and after depressurization, X-ray images collected before and after depressurization, and line scan images collected after depressurization (Core NGHP-01-05D-07Y only).

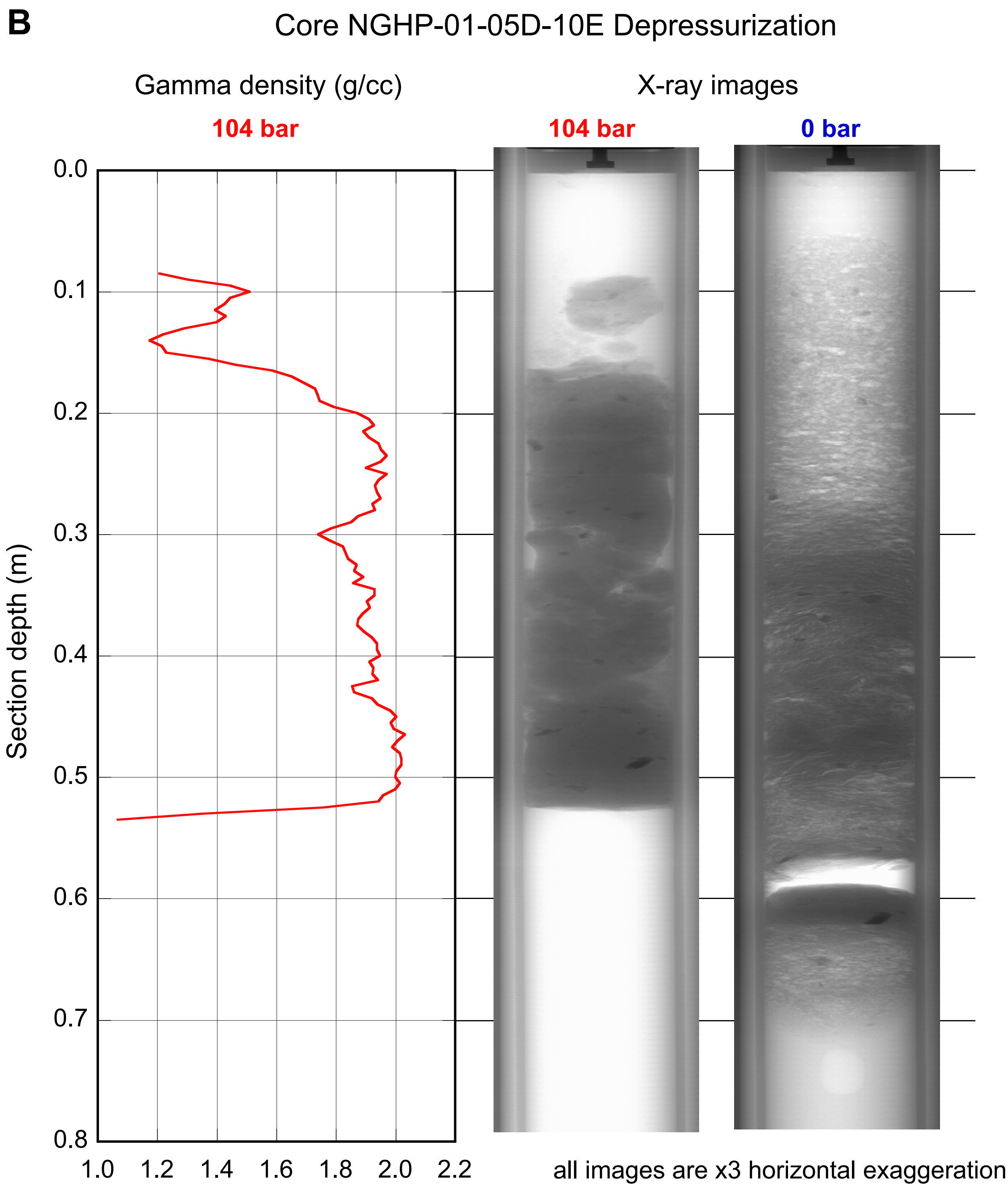

Figure 31. Summary of data taken from Cores NGHP-01-05D-07Y and NGHP-01-05D-10E before, during, and after depressurization, including gamma density profiles collected before and after depressurization, X-ray images collected before and after depressurization, and line scan images collected after depressurization (Core NGHP-01-05D-07Y only).—Continued

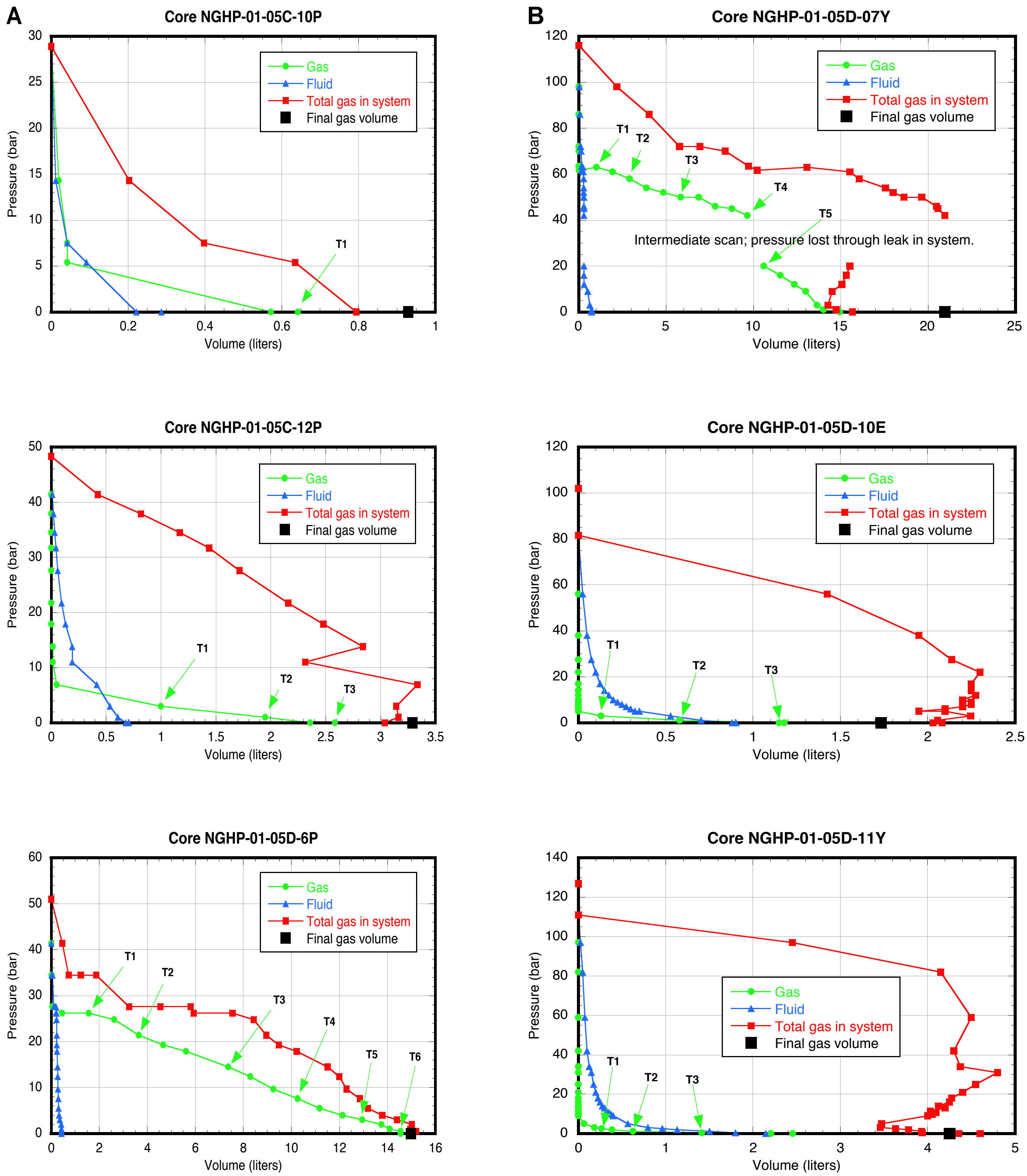

Figure 32. Pressure versus volume for Cores NGHP-01-05C-10P, NGHP-01-05C-12P, NGHP-01-05D-06P, NGHP-01-05D-07Y, NGHP-01-05D-10E, and NGHP-01-05D-11Y, also showing placement of intermediate X-ray or gamma density scans and gas samples (see "Organic Geochemistry"). [Green circles, collected gas; blue triangles, collected fluid; red squares, total gas in system (calculated as described in the "Methods" section); large black square, final calculated gas from cores; and T(number), gas samples]

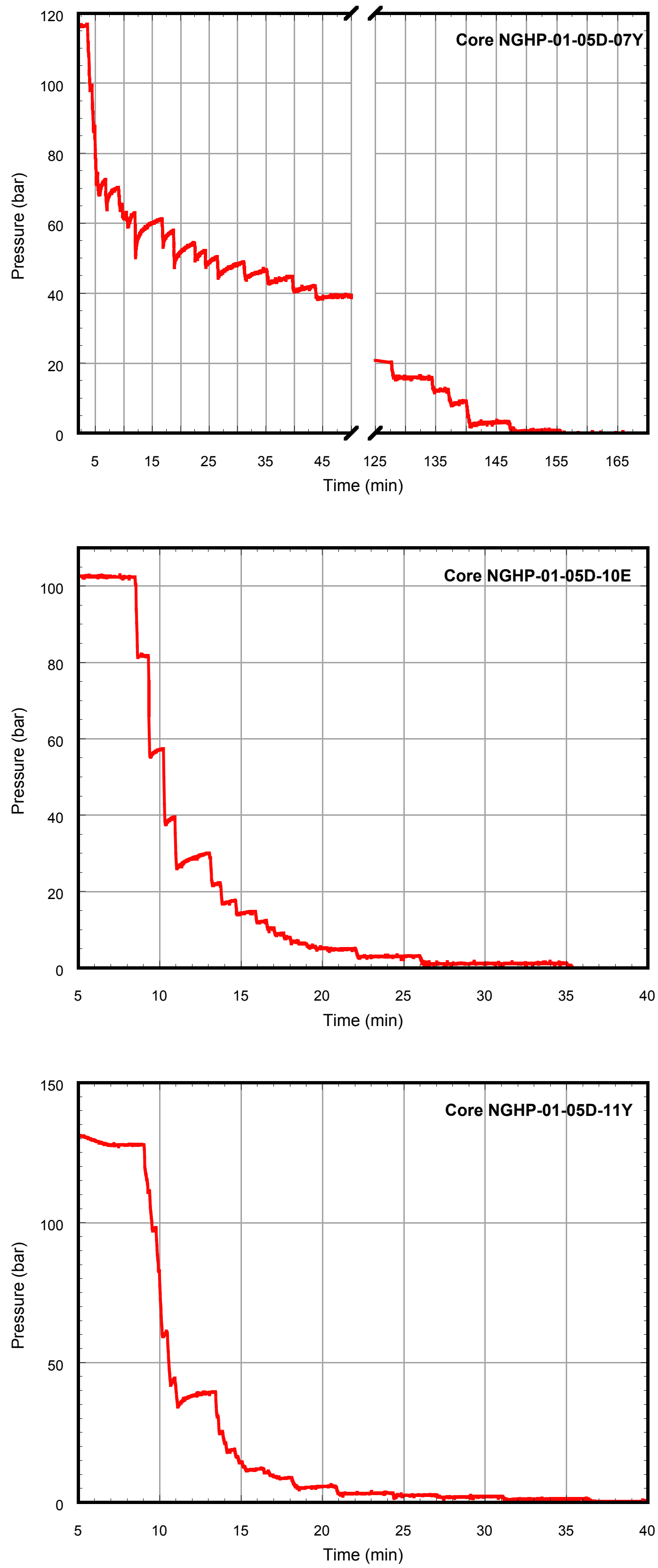

Figure 33. Pressure versus time for Cores NGHP-01-05D-07Y, NGHP-01-05D-10E, and NGHP-01-05D-11Y. Note the pressure rebounds during depressurization of Core NGHP-01-05D-07Y, which are not present during depressurization of Cores NGHP-01-05D-10E and NGHP-01-05D-11Y.

Table 25. Methane hydrate volume and concentration in pore space for successful pressure cores at Site NGHP-01-05. Values required for calculation of methane hydrate concentration are also included.

Parameter	Units	NGHP-01-05C-10P	NGHP-01-05C-12P	NGHP-01-05D-06P	NGHP-01-05D-07Y, minimum*	NGHP-01-05D-07Y, estimated*	NGHP-01-05D-10E	NGHP-01-05D-11Y
Core diameter	mm	43.2	43.2	43.2	57	57	51	57
Sediment length	cm	36	100	98	86	86	42	90
Sediment porosity	%	58	58	58	58	58	51	51
Pore volume	*liters*	*0.309*	*0.857*	*0.840*	*1.283*	*1.283*	*0.435*	*1.165*
Volume methane collected	liters	0.93	3.06	14.98	14.39	20.00	1.73	4.25
Methane concentration in pore fluids**	mM	0	0	0	0	0	0	0
Total methane in core	*mmol*	*40.4*	*133.0*	*651.3*	*625.7*	*869.6*	*75.2*	*184.8*
In situ salinity	ppt	32.0	31.0	32.0	31.0	31.0	30.0	30.0
Methane saturation***	mM	87.9	91.2	86.7	90	90	105.3	112.8
Methane in pore fluids, assuming saturation	*mmol*	*75.3*	*78.2*	*72.8*	*115.5*	*115.5*	*45.8*	*131.4*
Excess methane	*mmol*	*13.3*	*54.9*	*578.5*	*510.2*	*754.1*	*29.4*	*53.4*
Volume of methane hydrate	*ml*	*1.8*	*7.5*	*78.8*	*69.5*	*102.8*	*4.0*	*7.3*
*Methane hydrate, % of pore volume*** **	*%*	*0.6*	*0.9*	*9.4*	*5.4*	*8.0*	*0.9*	*0.6*

Notes:

Rows in *italics* are calculated parameters.

*Core NGHP-01-05D-7Y contained at least 14.39 liters of methane; the actual content was estimated at 20 liters.

**Methane concentration (via headspace) was not measured on these cores. Zero concentration generates a conservative (minimum) estimate of gas hydate volume.

***Methane saturation calculated from Xu (2002, 2004) using a water depth of 957 mbsl, a thermal gradient of 46 °C/km, a seafloor temperature of 6.89 °C, and the above salinities.

****Assuming all gas hydrate evenly distributed throughout the pore space.

Gas-Hydrate Concentration, Nature, and Distribution from Pressure Coring

Six of the 10 pressure cores at Site NGHP-01-05 were recovered at sufficient pressures to accurately assess the total concentration of methane and hence the predicted amount of gas hydrate. The calculated methane concentration for these cores is shown in figure 34 in relation to the phase boundaries for Structure I methane hydrate. (All pressure cores released nearly pure methane with less than 50 ppm ethane, confirming Structure I methane hydrate; see “Organic Geochemistry”). All of these cores were above the base of gas-hydrate stability and hence there is no information from pressure coring on the possible existence of free gas below this zone. The one core that was retrieved below the BSR (Core NGHP-01-05D-12P) was not recovered at high pressure and, although depressurized, cannot be considered accurate. Calculated concentrations of gas hydrate as high as 9.4 percent and 8.0 percent of pore volume were found in two of the cores, NGHP-01-05D-06P and NGHP-01-05D-07Y, respectively, which were both recovered from within the zone of high electrical resistivity seen in the LWD logs (see “Downhole Logging”). Other pressure cores (NGHP-01-05C-10P and NGHP-01-05C-12P; NGHP-01-05D-10E and NGHP-01-05D-11Y) show small amounts of gas hydrate (1 percent or less by pore volume).

The two pressure cores with the highest calculated concentrations of gas hydrate (NGHP-01-05D-06P and NGHP-01-05D-07Y) provide interesting evidence for the nature and distribution of hydrate in the sediments at Site NGHP-01-05. The X-ray image for the top part of Core NGHP-01-05D-06P (fig. 29B) shows vertical/sub-vertical thin low density vein structures, interpreted as gas-hydrate veins, within a homogenous fine-grained matrix. These veins could be seen to be twisted inside the matrix when the core was rotated in the X-ray beam. Whether this twisting structure is representative of the *in situ* structure or whether it is a coring artifact (this core is a rotary PCS) is unclear. It is estimated that the observed submillimeter-thick veins can only account for approximately 20 mL of solid gas hydrate within Core NGHP-01-05D-06P, whereas the total volume of gas hydrate in the core was calculated to be 78 mL (table 25). The remaining gas hydrate may have been disseminated throughout the pore spaces, or distributed in very fine veins in a similar fashion to the cores analyzed is Singapore (see “Singapore Pressure Core Studies” in “Appendix 3”).

Core NGHP-01-05D-07Y shows a thin, but very distinctive, horizontal gas-hydrate vein at 59 cm core depth. Not only does the X-ray show this vein clearly, but it is also very distinctively revealed in both the gamma density profile and, most importantly, in the P-wave velocity profile where it shows up with an anomalously high velocity (fig. 30A). During depressurization, this vein rapidly turned to gas (see intermediate X-ray and gamma density profile taken at 38 bar; fig. 31A). The gas in

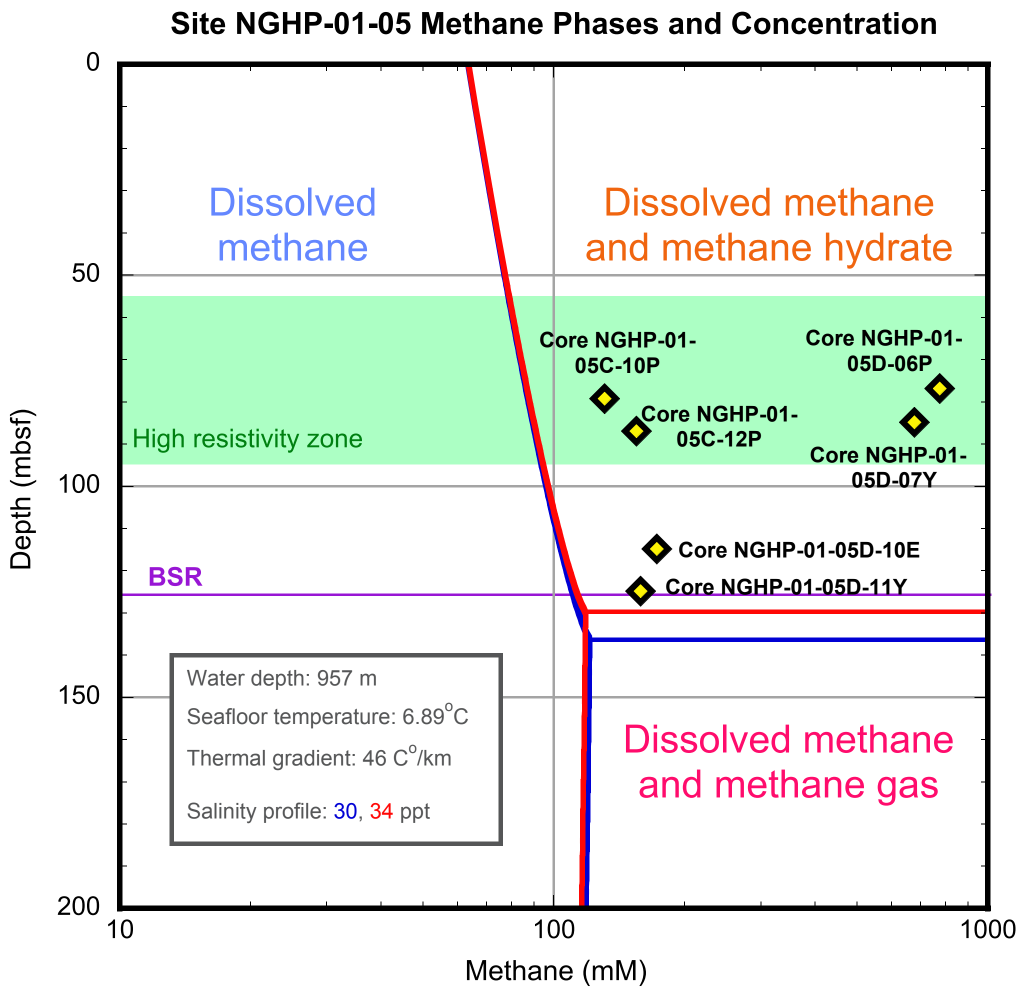

Figure 34. Methane phase diagram for Site NGHP-01-05, with total methane concentration measured from the six successful pressure cores at Site NGHP-01-05. The shipboard-calculated seafloor temperature (6.89 °C) and thermal gradient (46 °C) were taken from "Downhole Temperature Measurements" in "Physical Properties," the salinities were the minimum and maximum salinities around the depths of the pressure cores (30–34 ppt; table 5), and methane saturation was calculated according to Xu (2002, 2004). [ppt, parts per thousand]

the void was expelled and the void disappeared altogether when depressurization was complete (fig. 31A). The original vein at 59 cm was estimated to be 0.5 cm thick, or approximately 13 mL of gas hydrate, only a fraction of the total gas hydrate calculated to exist in the core (103 mL; table 25). The remaining gas hydrate may have been disseminated throughout the pore spaces, or distributed in very fine veins in a similar fashion to the cores analyzed is Singapore (see "Singapore Pressure Core Studies" in "Appendix 3").

It is interesting to note that the thin vertical/subvertical veins that have been observed in Core NGHP-01-05D-06P and elsewhere (Tréhu and others, 2003; Expedition 311 Scientists, 2005) seem to occur only when fine-grained sediments are relatively homogenous, whereas where there are lithological structures such as thin silt bands or carbonate layers (for example, Core NGHP-01-05D-07Y; also see "Lithostratigraphy"), pore-filling gas hydrate occurs as horizontal layers or lenses.

Downhole Logging

Logging While Drilling

Operations

LWD operations at Site NGHP-01-05 included two holes. When the first hole was drilled (NGHP-01-05A) the ProVISION NMR tool was not functioning, and the second hole (NGHP-01-05B) was drilled to run the NMR tool in an interval that was known to contain gas hydrate.

After tagging the seafloor at 963 mbrf (driller's depth), Hole NGHP-01-05A was spudded at 2200 hr on 24 May 24. LWD tools in the BHA included the GeoVISION, the EcoScope, the SonicVISION, and the TeleScope MWD. For details on each LWD tool and the measurements it makes, see the "Downhole Logging" section in the "Methods" chapter.

To acquire real-time data from the seafloor, Hole NGHP-01-05A was spudded with a high flow rate of 370 gpm, which is the flow rate needed to power up the MWD TeleScope tool and the EcoScope tool. It was recognized that such a high flow rate would likely lead to an enlarged hole, and the purpose of this experiment was to determine if useful LWD data could be collected near the seafloor when pumping at a high flow rate. The first 10 m were drilled with a rotation rate of 20 rpm and a rate of penetration (ROP) of 25 m/h. Below 10 mbsf, the rotation rate was increased to 30 rpm; over the range of 30–35 mbsf, the rotation rate was increased to 60 rpm, continuing to drill with a ROP of 25 m/h. The target depth of 200 mbsf (1,163 mbrf) was reached at 1145 hr on May 25, 2006. Data download and rig down were completed at 1710 hr on May 25.

Hole NGHP-01-05B was located 11 m N of the location of Hole NGHP-01-05A, and spudded at 1915 hr on June 4, 2006, after tagging the seafloor at 952 mbrf (driller's depth). LWD tools in the BHA included the GeoVISION, the EcoScope, the SonicVISION, the TeleScope MWD, and the ProVISION NMR tools.

To avoid washing out the hole near the seafloor, Hole NGHP-01-05B was spudded at a relatively low flow rate. The first 10 m were drilled at 100 gpm with a rotation rate of 20 rpm and a ROP of 25 m/h. Below 10 mbsf, the rotation rate was increased to 30 rpm; at 30 mbsf, it was increased to 60 rpm and the flow rate was increased until the LWD tools turned on (~370 gpm), continuing to drill with a ROP of 30 m/h. The target depth of 202 mbsf (1154 mbrf) was reached at 0447 hr on June 5, 2006. Data download and rig down were completed at 1145 hr on June 5. (The depths in mbsf mentioned above for Hole NGHP-01-05B are referenced to the seafloor depth tagged by the driller.)

Gas Monitoring with Real Time LWD/MWD Data

The LWD logs were acquired in the first holes drilled at Site NGHP-01-05 to plan coring and pressure-coring operations in subsequent holes. As Holes NGHP-01-05A and NGHP-01-05B were drilled without coring, the LWD data had to be monitored for safety to detect gas entering the wellbore. As explained in the "Downhole Logging" section of the "Methods" chapter, the primary measurement used in the gas monitoring was the "annular pressure while drilling" (APWD) measured by the EcoScope tool in the borehole annulus. We looked for sudden decreases of more than 100 psi in the annular pressure, which could be due to low-density gas entering the wellbore. We also monitored pressure increases of the same magnitude, which could be due to fluid acceleration caused by a gas kick (Aldred and others, 1998).

Figure 35 shows the measured borehole fluid pressure profiles in Holes NGHP-01-05A and NGHP-01-05B after the subtraction of the hydrostatic pressure trend. This residual pressure curve is essentially the same in both holes and shows only minor fluctuations that are well below the 100 psi level that would have required preventive action. We also monitored the coherence of the sonic waveforms acquired by the SonicVISION tool, focusing on the sound velocity in the borehole fluid. Gas indicators would be loss of coherence in the waveforms and a slower sound velocity for the drilling fluid. We found no significant decrease of sonic waveform coherence throughout the interval drilled.

LWD Log Quality

Figure 35 also shows the quality control logs for Holes NGHP-01-05A and NGHP-01-05B. The two curves for rate of penetration are an instantaneous rate of penetration (ROP_RM) and a rate of penetration averaged over the last 5 feet (ROP5_RM). The occasional large peaks in the instantaneous rate of penetration are artifacts due to depth fluctuations during pipe connections. The average ROP is about 20 m/h in Hole NGHP-01-05A and 30 m/h in Hole NGHP-01-05B, which is sufficient to record high resolution GeoVISION resistivity images and ProVISION NMR data (for details, see "Downhole Logging" in the "Methods" chapter).

The density (DCAV) and ultrasonic caliper logs (UCAV) in Hole NGHP-01-05A show a very enlarged hole near the seafloor, probably due to the high pumping rates used while drilling this hole. Above 22 mbsf, the hole was apparently too large for the ultrasonic caliper to return a measurement and the density caliper shows a hole diameter >14 in. Below 22 mbsf, the ultrasonic caliper consistently shows a bigger hole than the density; the two calipers agree again below 100 mbsf. The bit size (gray line in fig. 35) is 9 7/8 in, and except for a washout at 127–146 mbsf most of the borehole below 107 mbsf is in gauge. The borehole is less enlarged near the seafloor in Hole NGHP-01-05B, probably because of the lower pumping rate, and the hole is nearly in gauge below 100 mbsf. It is also interesting to note that the deep part of Hole NGHP-01-05B looks clearly smoother than the corresponding portion of Hole NGHP-01-05A; the higher ROP in Hole NGHP-01-05B (about 30 m/h versus 20 m/h in Hole NGHP-01-05A) may have helped to avoid hole washouts.

The density correction, calculated from the difference between the short-and long-spaced density measurements, is everywhere within the interval 0–0.2 g/cm^3 in both Holes NGHP-01-05A and NGHP-01-05B (fig. 35), suggesting that the density measurements should be of good quality (see below, however).

Figure 36 is a summary of the LWD gamma ray, density, neutron porosity, and resistivity logs measured in Holes NGHP-01-05A and NGHP-01-05B. (SonicVISION and ProVISION results are not shown because they need processing on shore.) The gamma ray and resistivity logs measured by the GeoVISION (red and orange curves) and EcoScope LWD tools (green and blue curves) generally agree. The GeoVISION and EcoScope gamma ray curves have the same shape, but are offset by about 20–30 gAPI; this difference is most likely due to tool calibration.

Figure 37 shows a comparison of the ring resistivity measured by the GeoVISION with the attenuation and phase resistivity curves obtained by the EcoScope tool at different frequencies and transmitter-receiver spacings. For a given transmitter-receiver spacing, the phase-shift EcoScope resistivities have higher vertical resolution than the attenuation resistivities and thus show more detail.

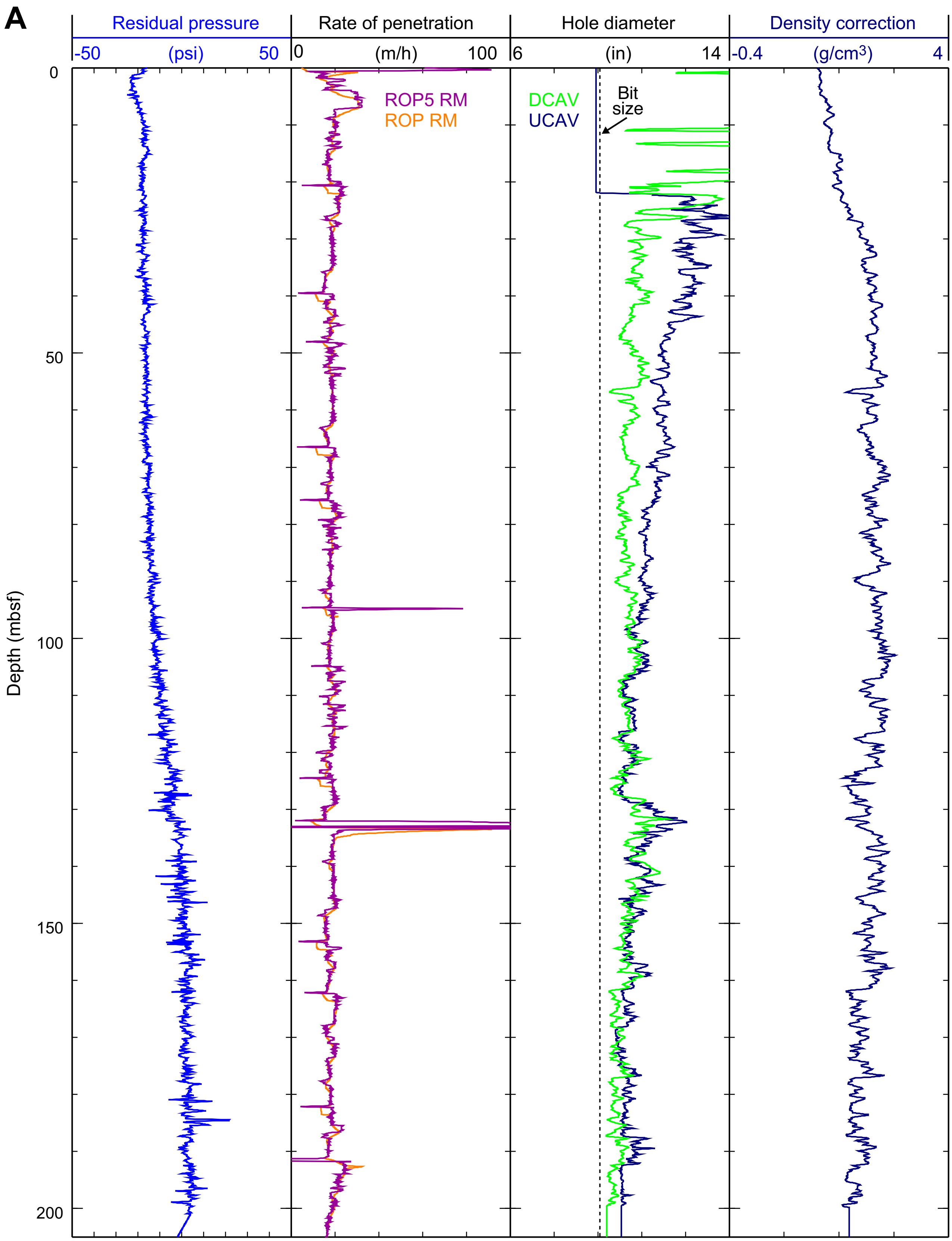

Figure 35. Monitoring and quality control LWD/MWD logs from Holes A, NGHP-01-05A and B, NGHP-01-05B. [LWD/MWD: logging-while-drilling/measurement/while/drilling; ROP, Rate of penetration; ROP_RM, Instantaneous rate of penetration; ROP5_RM, Rate of penetration averaged over a 5-ft interval; UCAV, Ultrasonic caliper; DCAV, Density caliper]

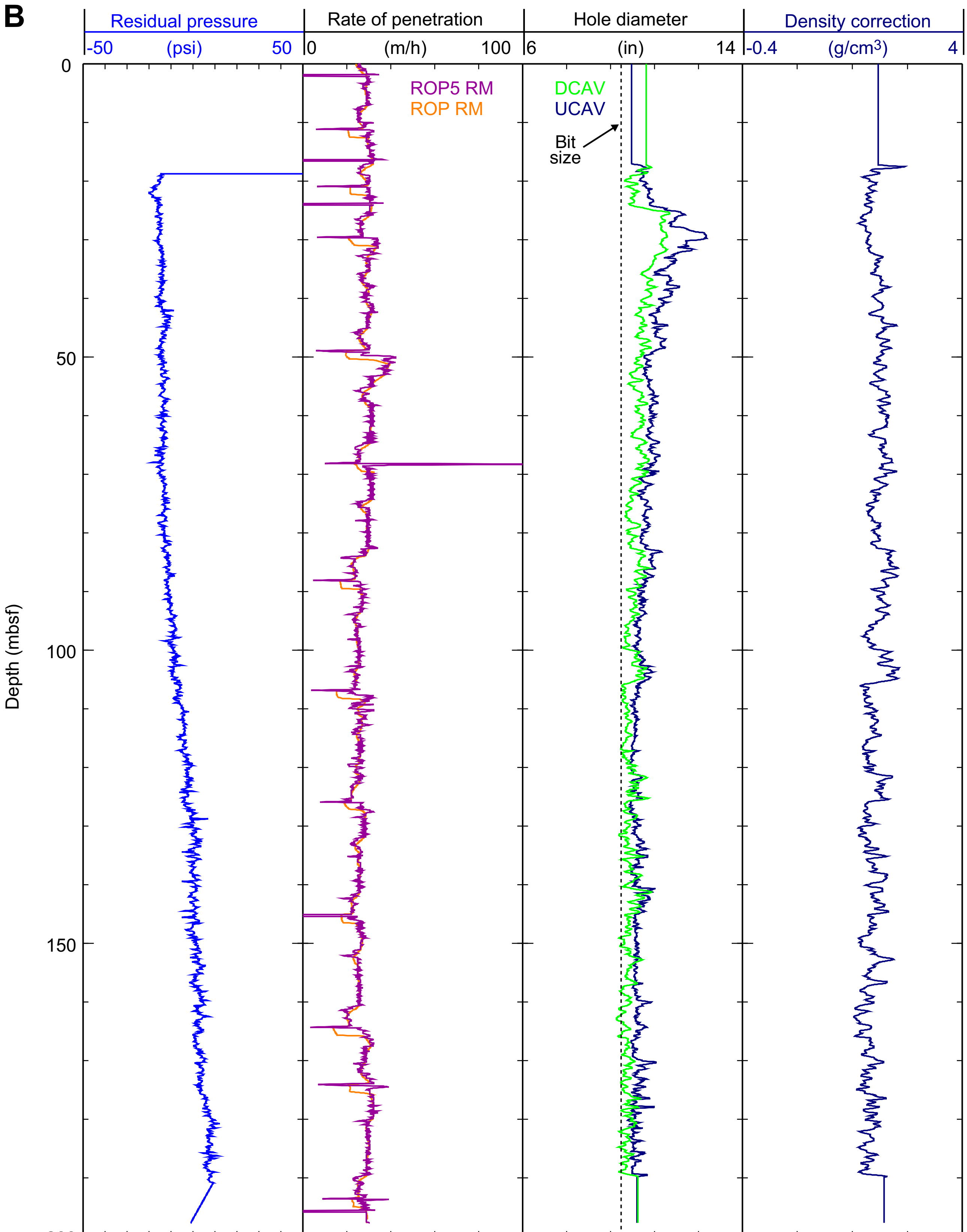

Figure 35. Monitoring and quality control LWD/MWD logs from Holes A, NGHP-01-05A and B, NGHP-01-05B. [LWD/MWD: logging-while-drilling/measurement/while/drilling; ROP, Rate of penetration; ROP_RM, Instantaneous rate of penetration; ROP5_RM, Rate of penetration averaged over a 5-ft interval; UCAV, Ultrasonic caliper; DCAV, Density caliper]—Continued

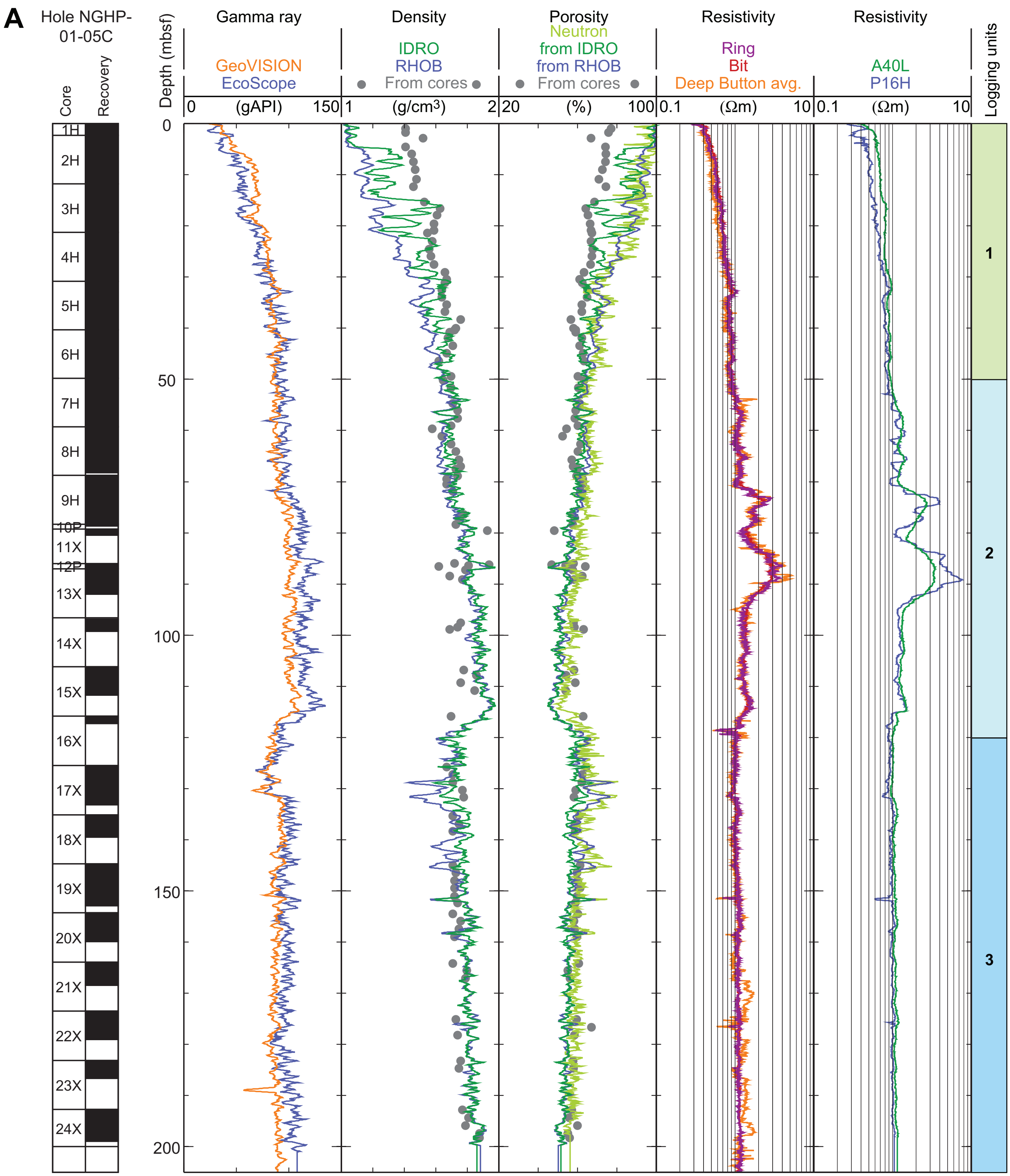

Figure 36. Summary of LWD log data from Holes A, NGHP-01-05A and B, NGHP-01-05B. [LWD; logging while drilling; gAPI, American Petroleum Institute gamma ray units; IDRO, Image-derived density (EcoScope); RHOB, Bulk density (EcoScope); neutron, Thermal neutron porosity (EcoScope); RING, Ring resistivity (GeoVISION); BIT, Bit resistivity (GeoVISION); Deep Button avg., Button deep resistivity (GeoVISION); A40L, Attenuation resistivity measured at 400 kHz and a transmitter-receiver spacing of 40 in (EcoScope); and P16H, Phase-shift resistivity at 2 MHZ and a transmitter-receiver spacing of 16 in (EcoScope)]

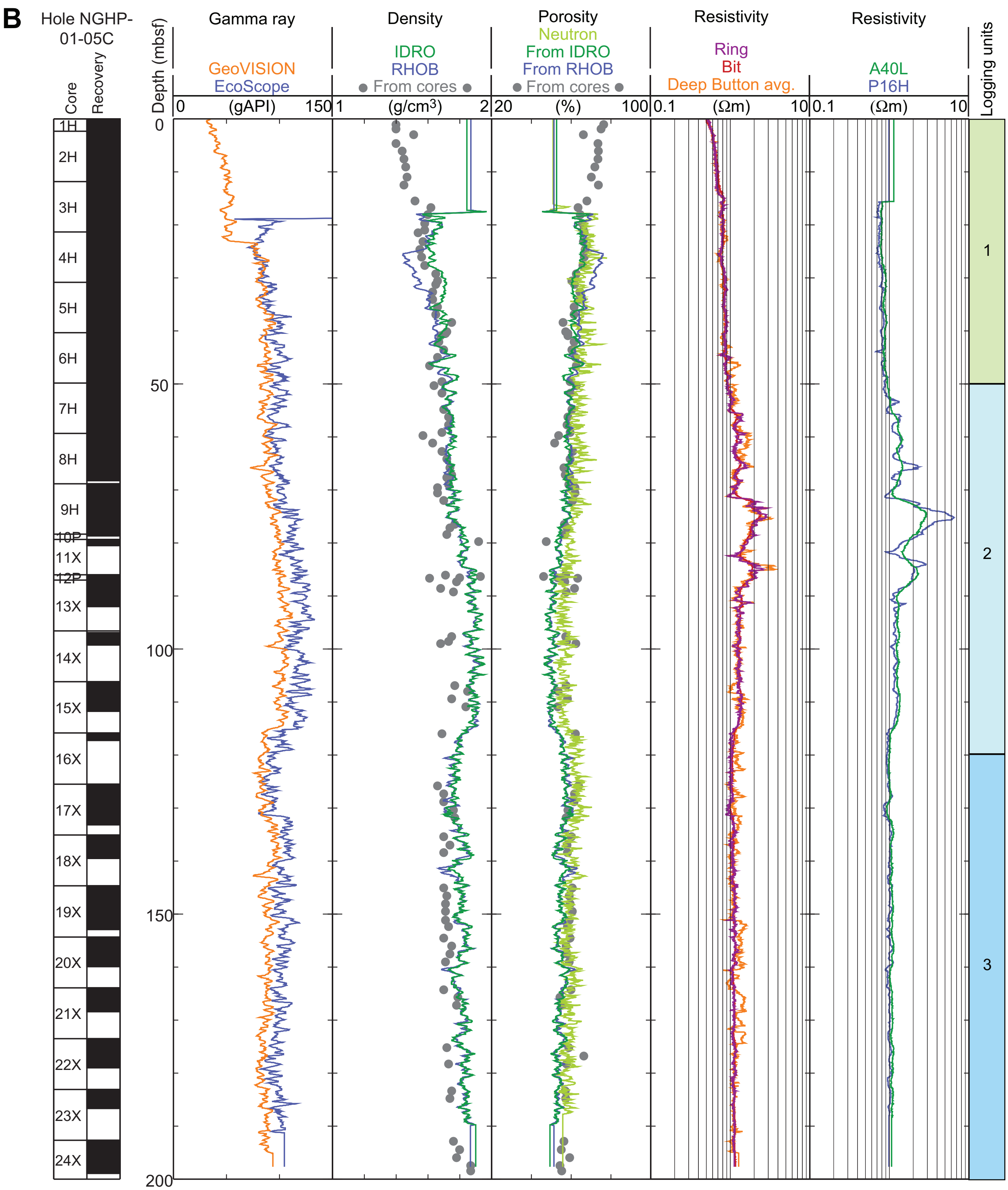

Figure 36. Summary of LWD log data from Holes A, NGHP-01-05A and B, NGHP-01-05B. [LWD; logging while drilling; gAPI, American Petroleum Institute gamma ray units; IDRO, Image-derived density (EcoScope); RHOB, Bulk density (EcoScope); neutron, Thermal neutron porosity (EcoScope); RING, Ring resistivity (GeoVISION); BIT, Bit resistivity (GeoVISION); Deep Button avg., Button deep resistivity (GeoVISION); A40L, Attenuation resistivity measured at 400 kHz and a transmitter-receiver spacing of 40 in (EcoScope); and P16H, Phase-shift resistivity at 2 MHZ and a transmitter-receiver spacing of 16 in (EcoScope)]—Continued

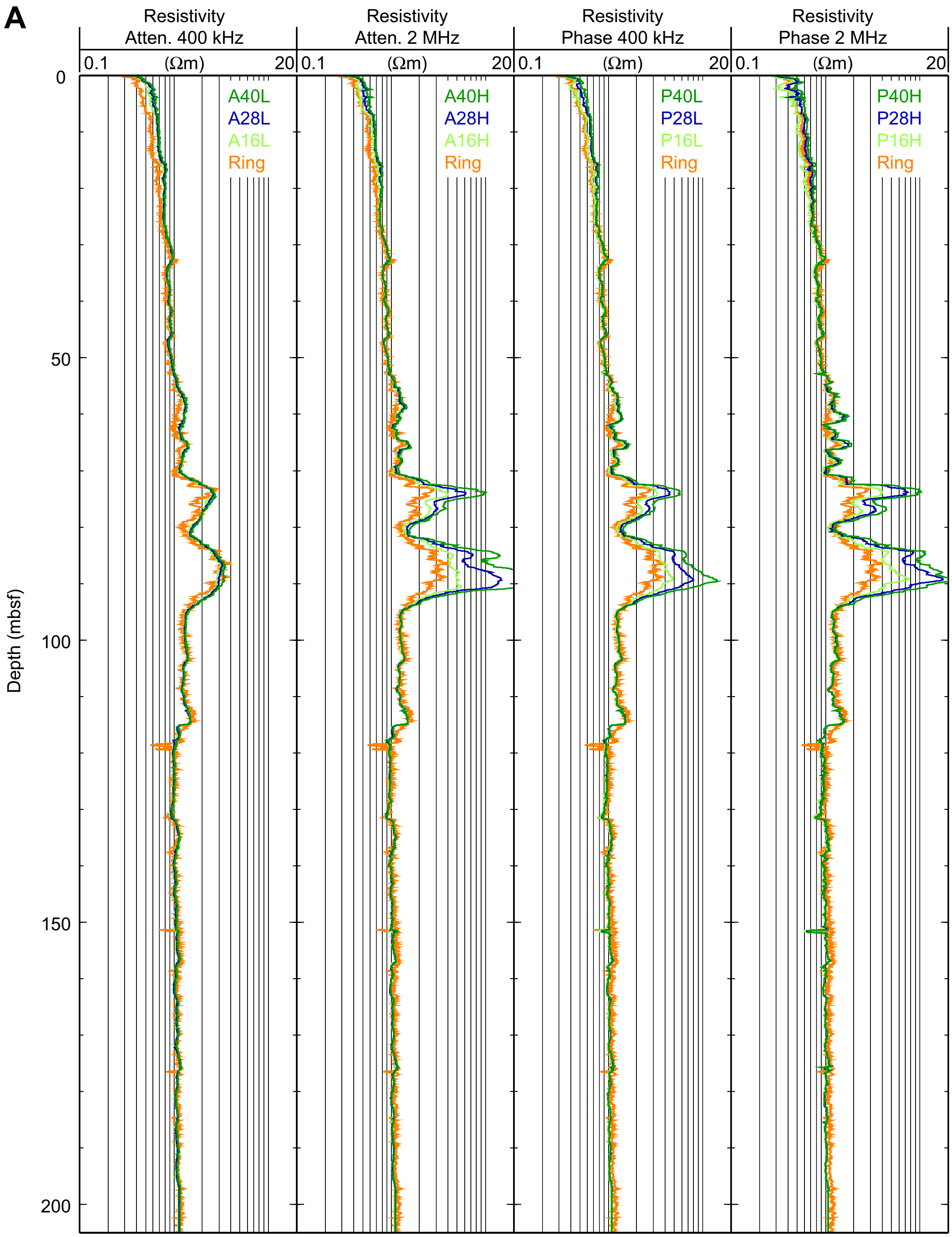

Figure 37. Comparison of LWD resistivity curves from Holes A, NGHP-01-05A and B, NGHP-01-05B. [LWD, logging-while-drilling; RES_RING, Ring resistivity (GeoVISION); AXXL, Attenuation resistivity measured at a frequency of 400 kHz, where XX is the transmitter-receiver spacing in inches (EcoScope); AXXH, Attenuation resistivity measured at a frequency of 2 MHz, where XX is the transmitter-receiver spacing in inches (EcoScope); PXXL, Phase-shift resistivity measured at a frequency of 400 kHz, where XX is the transmitter-receiver spacing in inches (EcoScope); PXXH, Phase-shift resistivity measured at a frequency of 2 MHz, where XX is the transmitter-receiver spacing in inches (EcoScope)]

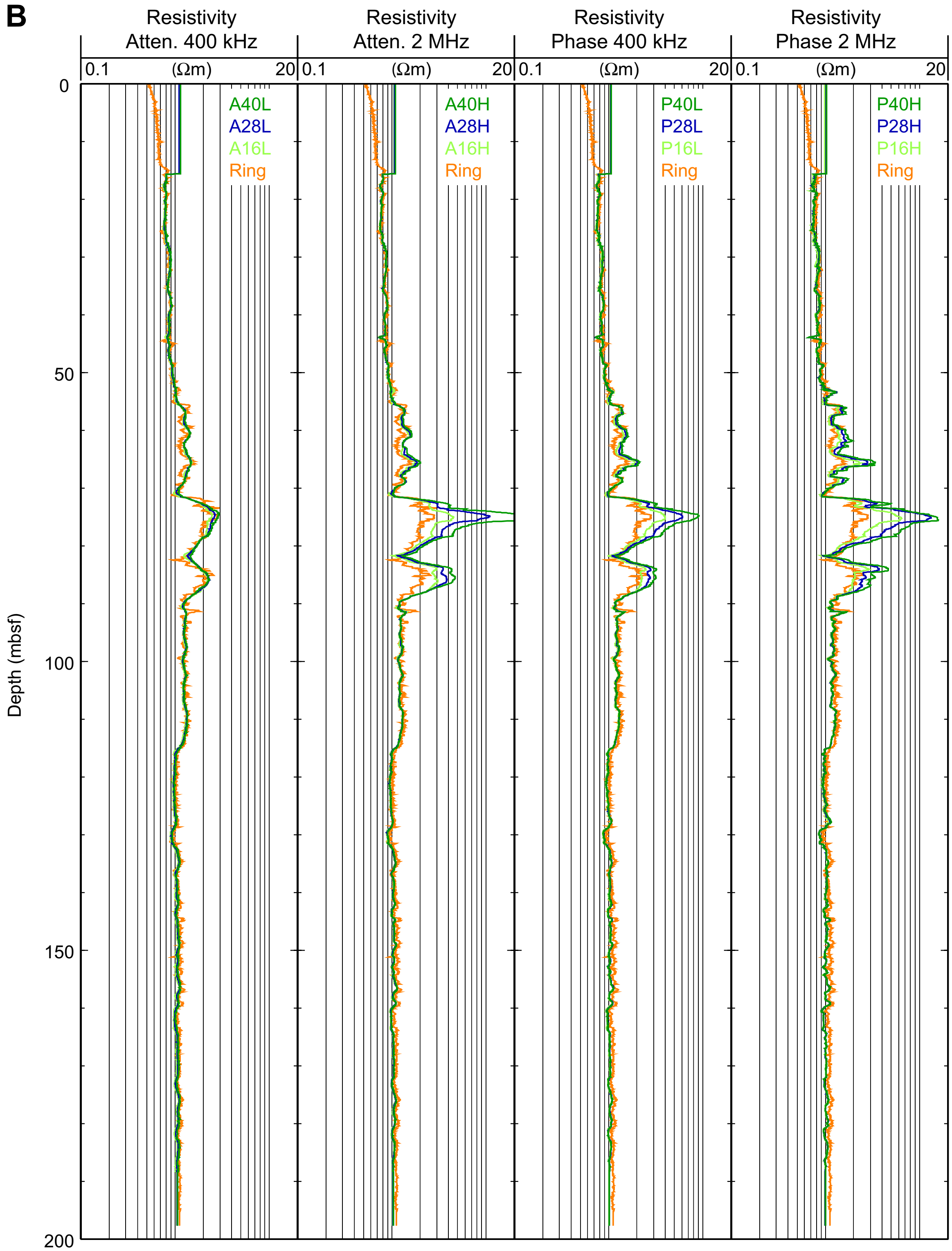

Figure 37. Comparison of LWD resistivity curves from Holes A, NGHP-01-05A and B, NGHP-01-05B. [LWD, logging-while-drilling; RES_RING, Ring resistivity (GeoVISION); AXXL, Attenuation resistivity measured at a frequency of 400 kHz, where XX is the transmitter-receiver spacing in inches (EcoScope); AXXH, Attenuation resistivity measured at a frequency of 2 MHz, where XX is the transmitter-receiver spacing in inches (EcoScope); PXXL, Phase-shift resistivity measured at a frequency of 400 kHz, where XX is the transmitter-receiver spacing in inches (EcoScope); PXXH, Phase-shift resistivity measured at a frequency of 2 MHz, where XX is the transmitter-receiver spacing in inches (EcoScope)]—Continued

A feature of interest in these resistivity curves is the pattern of high and low resistivities in the interval 71–94 mbsf of Hole NGHP-01-05A and 75–90 mbsf of Hole NGHP-01-05B. With the exception of the 400 kHz attenuation resistivities, as the transmitter-receiver spacing increases the resistivity high also increases (see especially the phase-shift resistivity curves). Larger transmitter-receiver spacings correspond to greater depths of investigation, and the pattern observed in figure 37 is characteristic of a conductive drilling fluid (in our case, seawater) invading high-resistivity layers that may contain gas hydrates. On the other hand, it is not clear why the 400 kHz attenuation resistivities do not show this pattern. See “Downhole Logging” in “Sites NGHP-01-10, 12, and 13” chapter for an alternative explanation involving resistivity anisotropy.

Figure 36 shows two bulk density curves: RHOB is the average density obtained by the EcoScope tool while rotating, while IDRO (image-derived density) is the value of density measured when the sensors were in closest contact with the formation. The two density curves are generally close, except for the intervals 0–68 mbsf and 125–146 mbsf in Hole NGHP-01-05A and 20–47 mbsf in Hole NGHP-01-05B, where the image-derived density is lower. The measured densities near the seafloor may be affected by the hole enlargements shown on the caliper logs (fig. 35).

The bottom-simulating reflector (BSR) that is observed on seismic reflection data and that should mark the bottom of the gas hydrate stability zone was estimated to be at a depth of 125 mbsf in Holes NGHP-01-05A and NGHP-01-05B. Near this depth, at 115 mbsf, both holes show a clear step change in density (from about 1.9 g/cm^3 above 115 mbsf to about 1.7 g/cm^3 below) and in resistivity (from about 1.3 Ω.m above 115 mbsf to about 1 Ω.m below). There is also, however, a corresponding change in natural gamma ray radioactivity (from 100–120 gAPI above 115 mbsf to 70–80 gAPI below), which suggests that this step change is not related to a change from gas hydrate to gas in the pore space as expected at the bottom of the gas-hydrate stability zone, but rather to a lithological change from clay-rich to sand-rich sediment (fig. 36).

The depths relative to seafloor were fixed for all of the LWD logs by identifying the step change in the GeoVISION gamma ray log at the seafloor. For Hole NGHP-01-05A, the gamma ray logging pick for the seafloor was at a depth of 956 mbrf, 7 m shallower than the initial depth estimated by the drillers (963 mbrf). For Hole NGHP-01-05B, the gamma ray logging pick for the seafloor was at a depth of 954.7 mbrf, 2.7 m deeper than the initial depth estimated by the drillers (952 mbrf). These differences in seafloor depth between Holes NGHP-01-05A and NGHP-01-05B are likely to reflect the finite accuracy of an absolute depth measurement based on the length of the drillpipe. The rig floor logging datum was located 10.5 m above sea level.

LWD Porosities

Sediment porosities can be determined from analyses of recovered cores and from downhole measurements (see “Physical Properties” and “Downhole Logging” in the “Methods” chapter). Sediment porosities were calculated from the LWD density and neutron logs in Holes NGHP-01-05A and NGHP-01-05B. Core-derived physical property data, including porosities (see “Physical Properties”), can be used to calibrate and evaluate the log-derived sediment porosities.

The LWD log-derived density measurements from Holes NGHP-01-05A and NGHP-01-05B were used to calculate sediment porosities (φ) with the standard density-porosity relation

$$\varphi = (r_g - r_b) / (r_g - r_w)$$

We used a constant water density (r_w) equal to 1.03 g/cm^3 and a grain/matrix density (r_g) equal to 2.75 g/cm^3. The density log-derived porosities from Hole NGHP-01-05A range from almost 100 percent near the seafloor (which could be due to the enlarged hole) to a minimum of about 45 percent at 115 mbsf (fig. 36). In Hole NGHP-01-05B, which was not so enlarged near the top, the density porosity is about 65 percent at 20 mbsf. The density porosities in figure 36 have been calculated from both the bulk density and from the image-derived density curve.

The LWD neutron porosity log from Hole NGHP-01-05A (fig. 36) yielded sediment porosities ranging from almost 100 percent near the seafloor (which could be due to the enlarged hole) to a minimum of about 50 percent at 115 mbsf. In Hole NGHP-01-05B, which was not so enlarged near the top, the neutron porosity is about 70 percent at 20 mbsf. Porosities measured by the neutron log are expected to be higher than those computed from the density log in clay-rich sediments, because the neutron log essentially quantifies hydrogen abundance, and counts hydrogen in clay minerals as porosity. The neutron porosity measured by the EcoScope tool shown in figure 36 is the “best thermal neutron porosity” (BPHI); it has been corrected so that the effect of clay is reduced (Adolph and others, 2005), and it is only marginally higher than the density porosity.

The comparison with measurements made on core samples (fig. 36) shows that the LWD derived porosities are in good agreement with the laboratory data, except for the upper section of the hole where the enlarged hole (fig. 35A) is responsible for erroneously low density and high porosity values.

LWD Borehole Images

The GeoVISION and EcoScope LWD tools generate high-resolution images of borehole log data. The EcoScope tool produces images of density and hole radius (computed on the basis of the density correction, which depends on the borehole standoff). The GeoVISION produces a gamma ray image and resistivity images with shallow, medium and deep depth of investigation.

Figure 38 shows some of the LWD images collected by the EcoScope and GeoVISION tools in Holes NGHP-01-05A and NGHP-01-05B. It should be noted that the display in figure 38 is highly compressed in the vertical direction. The unwrapped images are about 80 cm wide (for a 10 in diameter borehole) and the vertical scale is compressed relative to the horizontal by a factor of about 55:1. These high-resolution

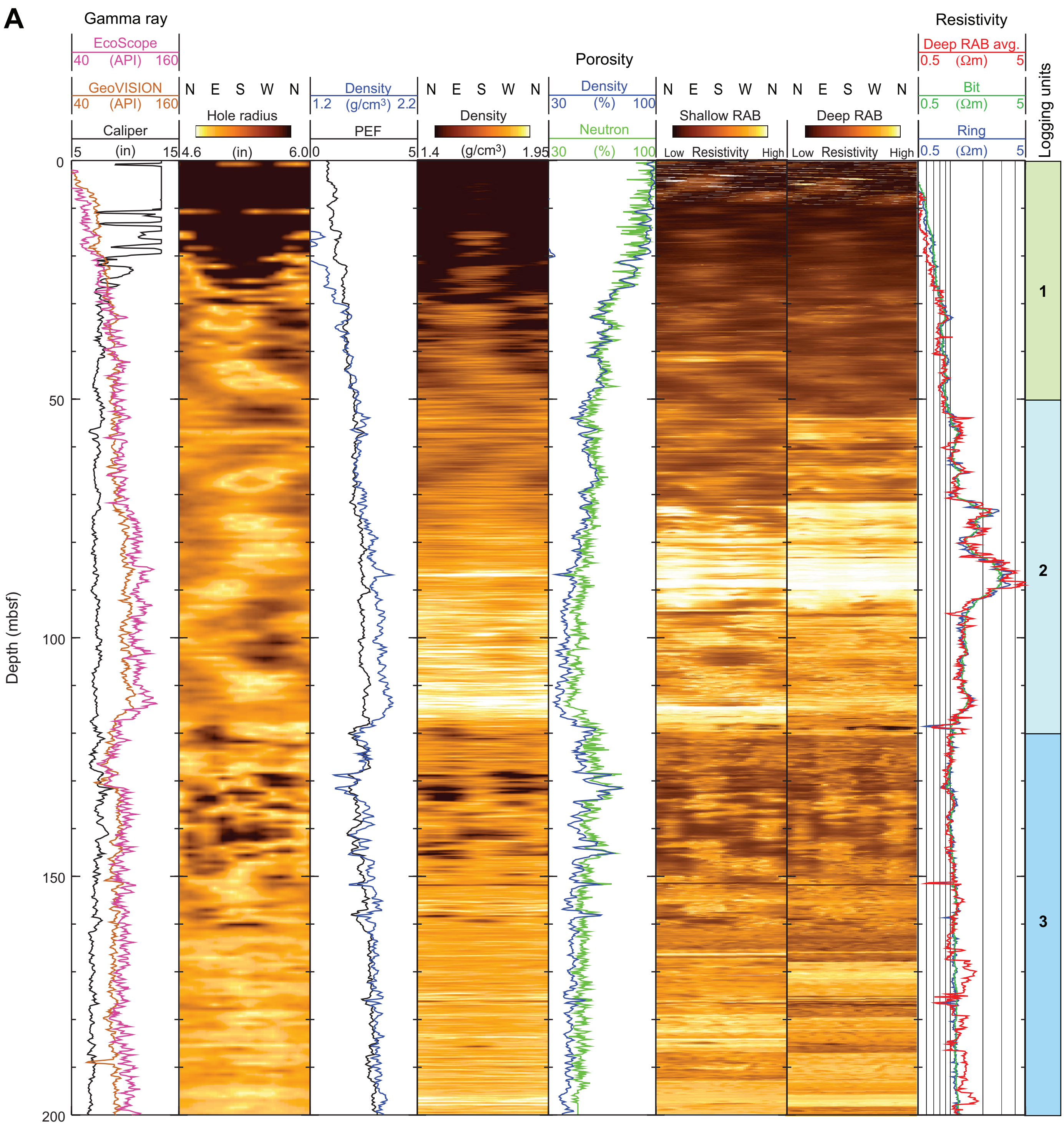

Figure 38. LWD image data from Holes A, NGHP-01-05A and B, NGHP-01-05B. [LWD, logging-while-drilling, gAPI, American Petroleum Institute gamma ray units, RAB, Resistivity-At-Bit image obtained by the GeoVISION tool]

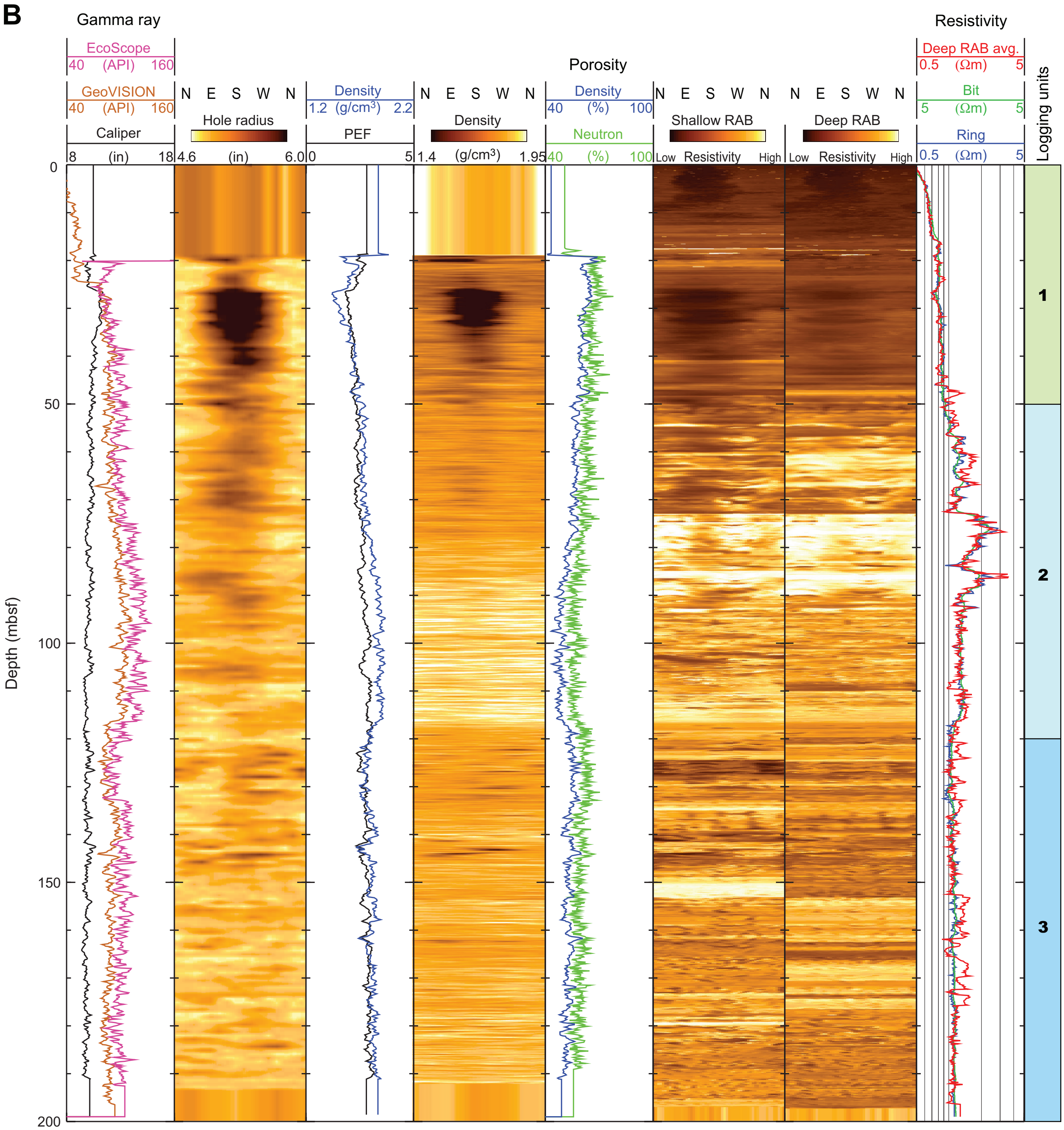

Figure 38. LWD image data from Holes A, NGHP-01-05A and B, NGHP-01-05B. [LWD, logging-while-drilling, gAPI, American Petroleum Institute gamma ray units, RAB, Resistivity-At-Bit image obtained by the GeoVISION tool]—Continued

images can be used for detailed sedimentological and structural interpretations and to image gas-hydrate distribution in sediments (for example, in layers, nodules, fractures). Gas-hydrate-bearing sediments exhibit high resistivities within intervals of uniform or low bulk density. Layers with high resistivities and high densities are likely to be low porosity, compacted, or carbonate-rich sediments. The two resistivity images in figure 38 correspond to two depths of investigation (for details, see “Downhole Logging” in the “Methods” chapter).

The most striking features in the borehole images are the high-resistivity layers in the interval 71–94 mbsf in Hole NGHP-01-05A and 72–95 mbsf in Hole NGHP-01-05B. These high resistivities do not correspond to high densities in the density image and thus are likely to be local gas-hydrate accumulations.

Wire-Line Logging

Operations

After completion of pressure-coring operations in Hole NHGHP-01-05D, the hole was conditioned for logging. Two wiper trips were necessary, indicating that 15 m of fill had accumulated at the bottom. The hole was then displaced with 80 bbl of barite, and preparation of the rig floor for logging started at 1745 hr, on June 13, 2006. The assembly of the triple combo tool string started at 1950 hr and the tool string was lowered into the hole at 2050 hr. It could not pass below an obstruction at 1,111 mbrf, or 156 mbsf. The hole kept deteriorating as we were trying to go deeper, and at 2320 hr we decided to log up from 1,083 mbrf and to drill a new hole dedicated to logging. The tool was back on the rig floor at 0045 hr on June 14, 2006.

The new hole (NGHP-01-05E) was completed to TD 200 mbsf (1,155 mbrf) by 1300 hr on June 14, and a wiper trip found some tight spots but no fill. Because the most important piece of data still missing at this site was a sonic log, and for fear of a rapidly deteriorating hole, it was decided to run first a string made of the DSI (sonic) and SGT (gamma ray), followed by a Triple combo that would provide a caliper for hole quality assessment, and finish with a VSP. If time and hole conditions permitted we would run a FMS before the VSP.

Rig up of the DSI/SGT started at 1900 hr. The tool was lowered at 1950 hr and back on the rig floor at 2355 hr, after three successful passes from the bottom of the hole (1,155 mbrf), including various combinations the monopole, dipole, and cross-dipole modes.

The triple combo string was then assembled, starting at 0025 hr on 5 June. It was then rigged-into-hole at 0125 and also reached the bottom of the hole without any obstruction. The up-log started at 0250 hr and indicated surprisingly good hole conditions, encouraging for both a FMS and a VSP. The tool was back on deck at 0420 hr and rigged down by 0520 hr.

A string made of the FMS and the HNGS (gamma ray) was completed and RIH by 0545 hr, and recorded two successful passes without any obstacle. Some trouble with the FMS caliper required additional caution at the end of the run, but the tool appeared undamaged and was disassembled by 0830 hr.

The final run was a vertical seismic profile (VSP) with the VSI tool, targeting stations every 5 m. The rig up was complete at 0845 hr. After completing the required watch for marine mammal activity, the tool reached a maximum depth of 1,152 mbrf. Out of 30 stations attempted, with a total of 281 shots fired, 20 provided good waveforms, after stacking allowing us to define a reliable time-to-depth conversion for hole-seismic correlations. Because of the proximity of the pipe, none of the attempts above 1,045 mbrf were successful. The tool was back on deck at 1550 hr, rigged down at 1610 hr, and the rig floor was clear by 1630 hr.

Wire-Line Log Quality

Figure 39 shows a summary of the wire-line data recorded in Hole NGHP-01-05E. The caliper logs recorded with the two arms of the FMS caliper indicate very good hole conditions, with an almost uniform hole size. As a result, the data are generally of very good quality. Despite the good hole conditions, the automatic pick of the compressional arrival in the sonic logging waveforms was not successful in this very slow formation. Additional processing was required postcruise to derive the reliable velocity logs shown in figure 40.

The depths relative to seafloor for all of the wire-line logs were fixed by identifying the step change in the gamma ray log associated with the seafloor. The gamma ray pick for the seafloor was at 956 mbrf in Hole NGHP-01-05E.

Logging While Drilling and Wire-Line Logging Comparison

Figure 41 shows a comparison of the logs that were recorded in all the holes logged at Site NGHP-01-05. Since LWD data are recorded almost immediately after the initial penetration, the caliper logs in Holes NGHP-01-05A and NGHP-01-05B indicate narrower holes than the wire-line logs. The only hole showing clearly poor conditions is Hole NGHP-01-05D, where the tool could not go deeper than 130 mbsf. The large diameter suggests that the obstruction was mostly due to material falling from the shallower portion of the hole. While the gamma ray log in Hole NGHP-01-05D shows lower values that the large caliper cannot account for, the three other holes show very similar trends, indicating little local variability in the lithology. The density and porosity logs are also in good agreement, except above ~120 m, where the holes are slightly enlarged and the wire-line logs display significantly higher neutron porosity. The resistivity logs show remarkably similar trends in Holes NGHP-01-05A, NGHP-01-05B, and NGHP-01-05E, indicating in particular, and despite local variations, an interval with high resistivity between ~75 and ~95 mbsf. This interval is also present in the logs recorded in Hole NGHP-01-05D, but extends to ~115 m, suggesting local heterogeneity in the gas hydrate distribution (see “Gas-Hydrate and Free Gas Occurrence”).

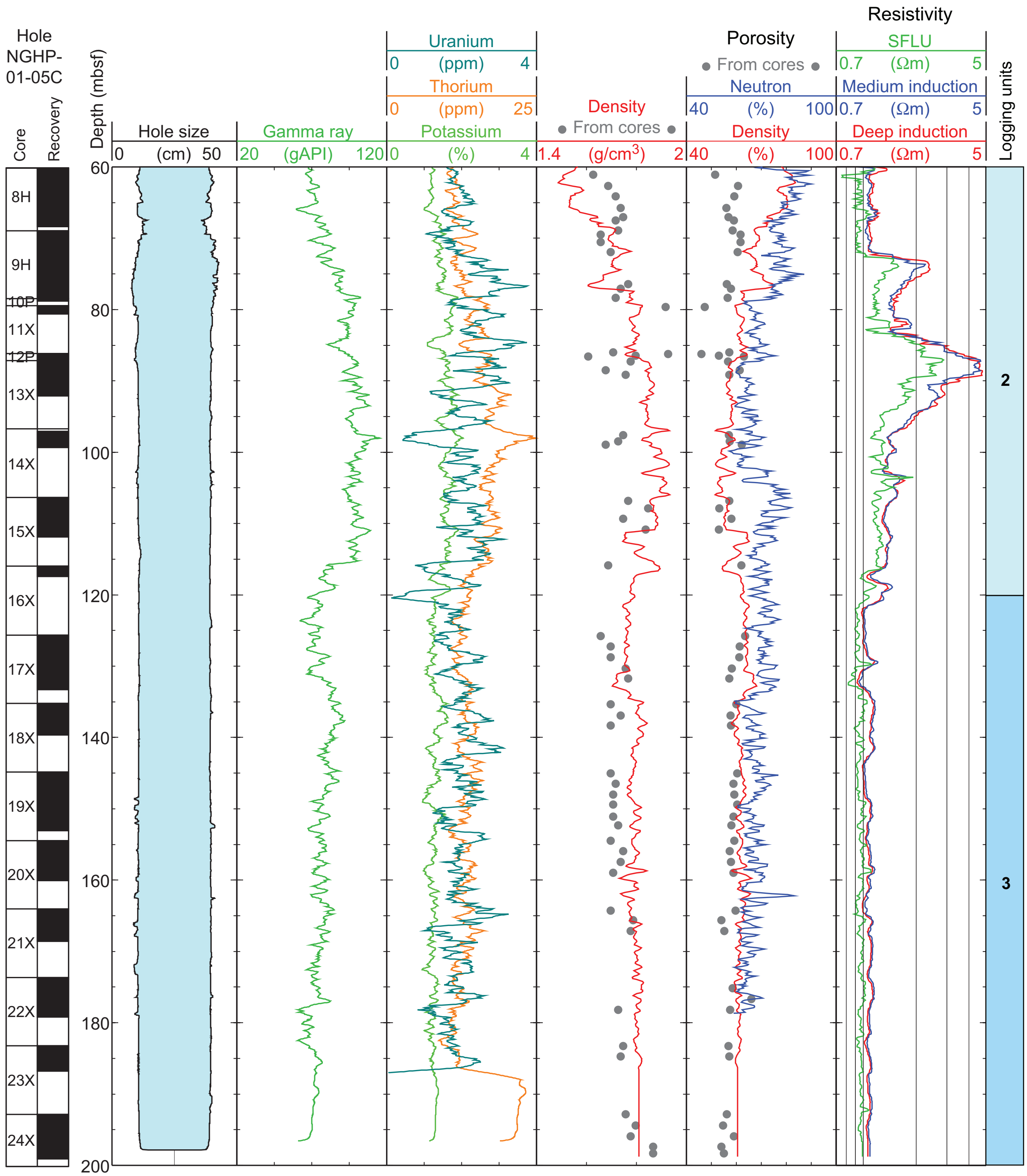

Figure 39. Summary of the wire-line logs recorded in Hole NGHP-01-05E.

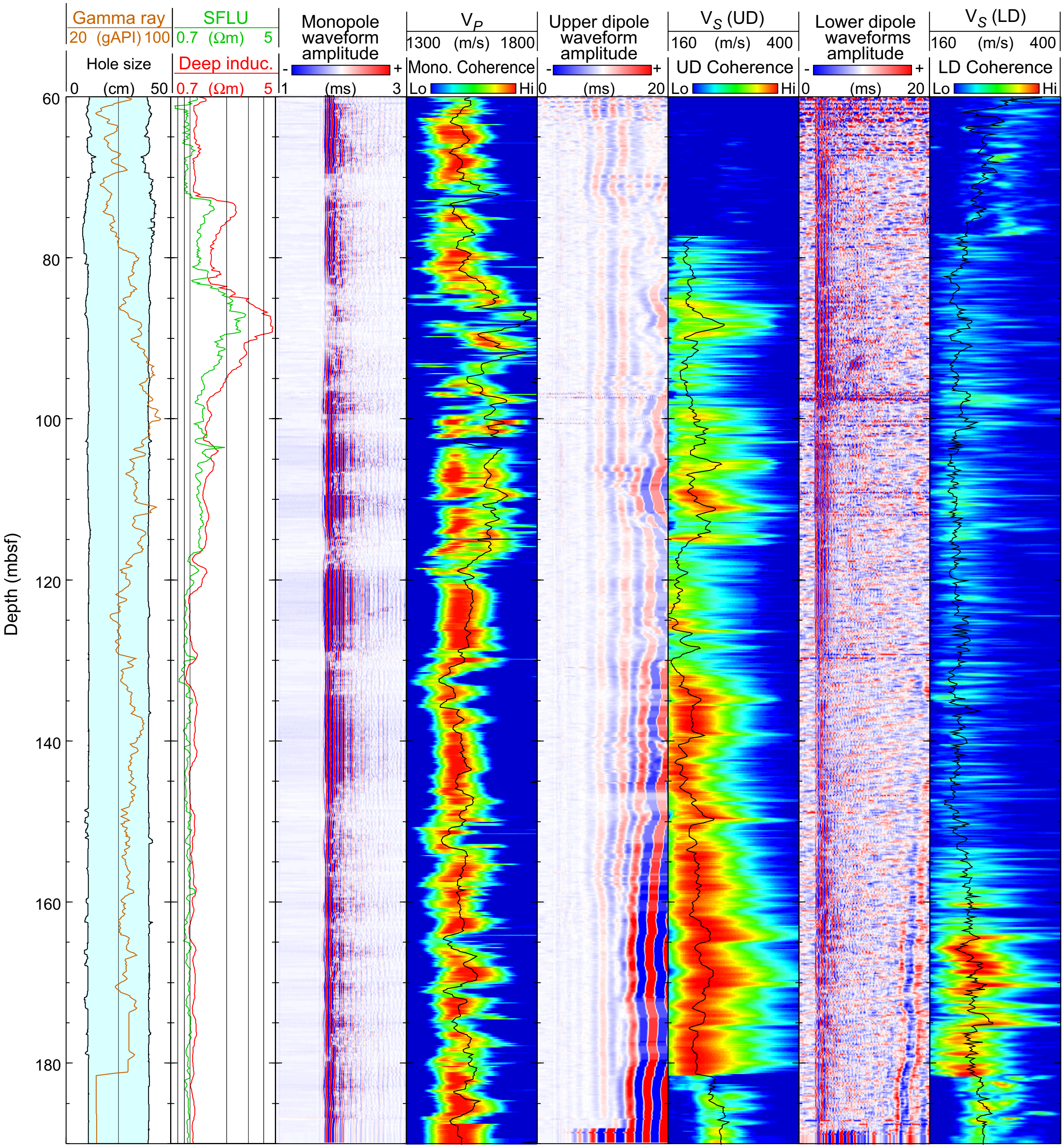

Figure 40. Sonic waveform data, *P*-wave and *S*-wave velocities measured by the DSI wire-line log in Hole NGHP-01-05E. [DSI, Dipole Sonic Imager; V_P, *P*-wave velocity; V_S, *S*-wave velocity; LD, Lower dipole; UD, Upper dipole]

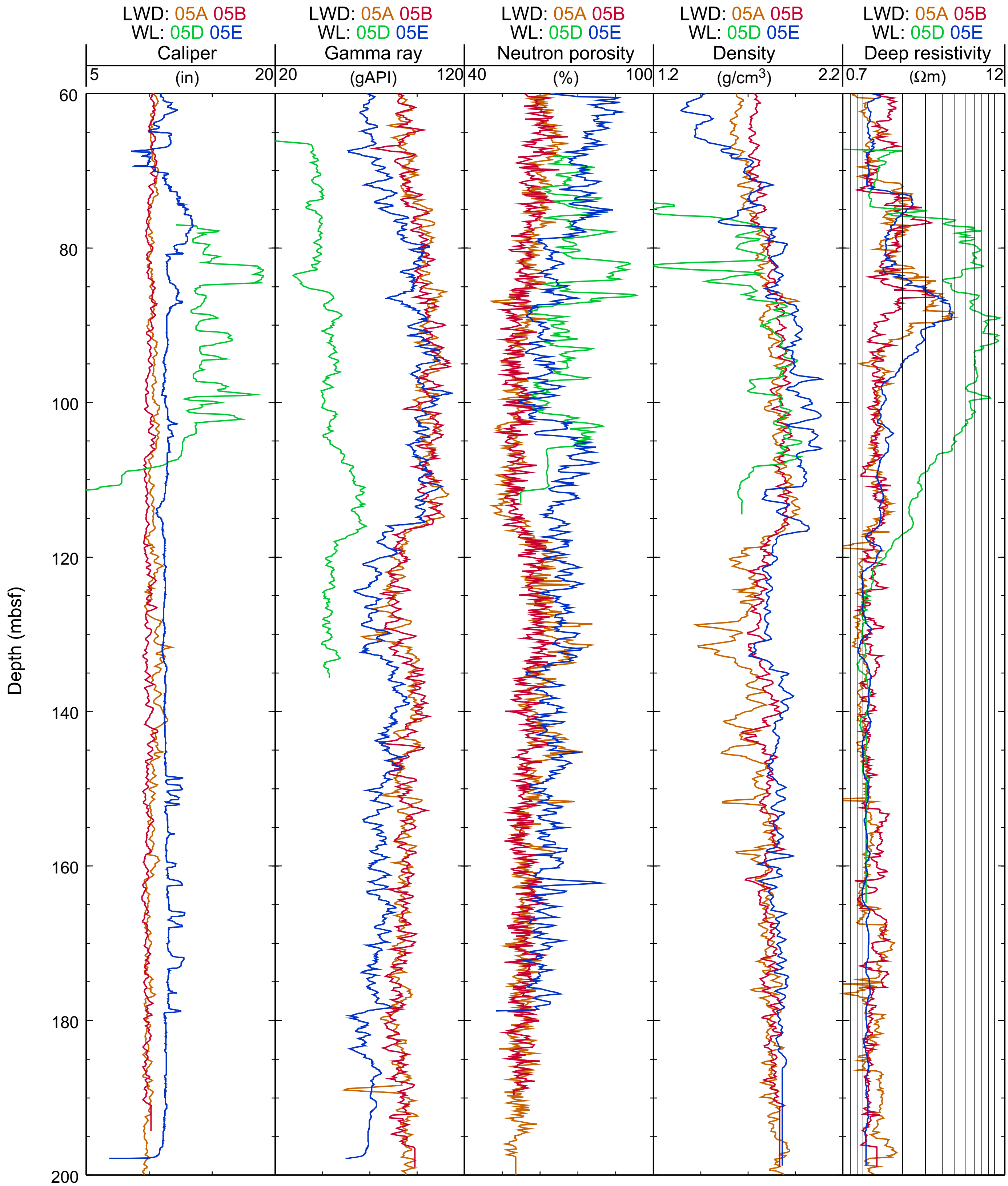

Figure 41. Comparison of LWD (Hole NGHP-01-05A and NGHP-01-05B) and wire-line log data (Holes NGHP-01-05D and NGHP-01-05E). [LWD, logging-while-drilling; WL, wire-line]

Logging Units

The combined evaluation of the LWD and wire-line logs at Site NGHP-01-05 (figs. 36, 38, and 39) suggests that the formation could be divided into three Logging Units, with distinct characters in particular in the gamma ray, density, or resistivity logs.

Logging unit 1 (0–50 mbsf), which was not measured by the wire-line logs, displays a steady increase with depth in density, resistivity, and gamma ray logs, indicating mostly unconsolidated sediments that required a careful restraint in drilling parameters in order to be captured in Hole NGHP-01-05B.

Logging unit 2 (50–120 mbsf) is characterized in all the holes by significant variability in resistivity, including intervals with values up to 12 Ω/m. Density and gamma ray steadily increase with depth through this unit. The high resistivity values were interpreted as indications of the presence of gas hydrate (see "Gas Hydrate and Free Gas Occurrence"). However, the higher density in the lower part of this unit, most apparent in the density image in figure 38, shows that the higher resistivity is also partially related to a more consolidated formation.

The top of Logging unit 3 (120–200 mbsf) is a sharp drop in density, gamma ray, and resistivity. The coincidence of the density and gamma ray changes, the latter apparently associated with a decrease in Thorium (fig. 39), suggests that the seismic reflector that was predicted at this depth to be the BSR might be mostly generated by a lithological change. The preliminary results of the VSP (fig. 42) suggest that the BSR, at a two-way travel time of 1.45 s, or 725 m/s one-way travel time, is at 122 mbsf.

Gas-Hydrate and Free Gas Occurrence

As previously discussed (see "Downhole Logging" in the "Methods" chapter), the presence of gas hydrate is generally characterized by increases in electrical resistivity and acoustic velocity that are not accompanied by a corresponding porosity decrease. A decrease in porosity alone in water-saturated sediments can result in an increase in resistivity and acoustic velocity. Resistivities logged in Holes NGHP-01-05A and NGHP-01-05B show a general negative correlation with porosity (fig. 36) except in the interval 55–94 mbsf (Hole NGHP-01-05A) and 53–90 mbsf (NGHP-01-05B), where high resistivities suggest that gas hydrate is present.

To make a quantitative estimate of the amount of gas hydrate at Hole NGHP-01-05A, we followed the procedure described in "Downhole Logging", in the "Methods" chapter, to apply the Archie relationship to the resistivity and porosity logs recorded in Holes NGHP-01-05A and NGHP-01-05B. The procedure and the results are shown in figure 43. The pore fluid resistivity (R_w) was estimated from Fofonoff (1985) using a linear temperature profile derived from *in situ* temperature measurements (6 °C at the seafloor and a gradient of 30 °C/km) and water salinity profile constrained from core sample measurement. The estimated m curve is derived from R_w, the porosity (φ) and resistivity (R_t) logs ($m_{est} = -\log F / \log\varphi$, where $F = R_t / R_w$). The value of $m = 2.2$ is given by the baseline of this curve in the

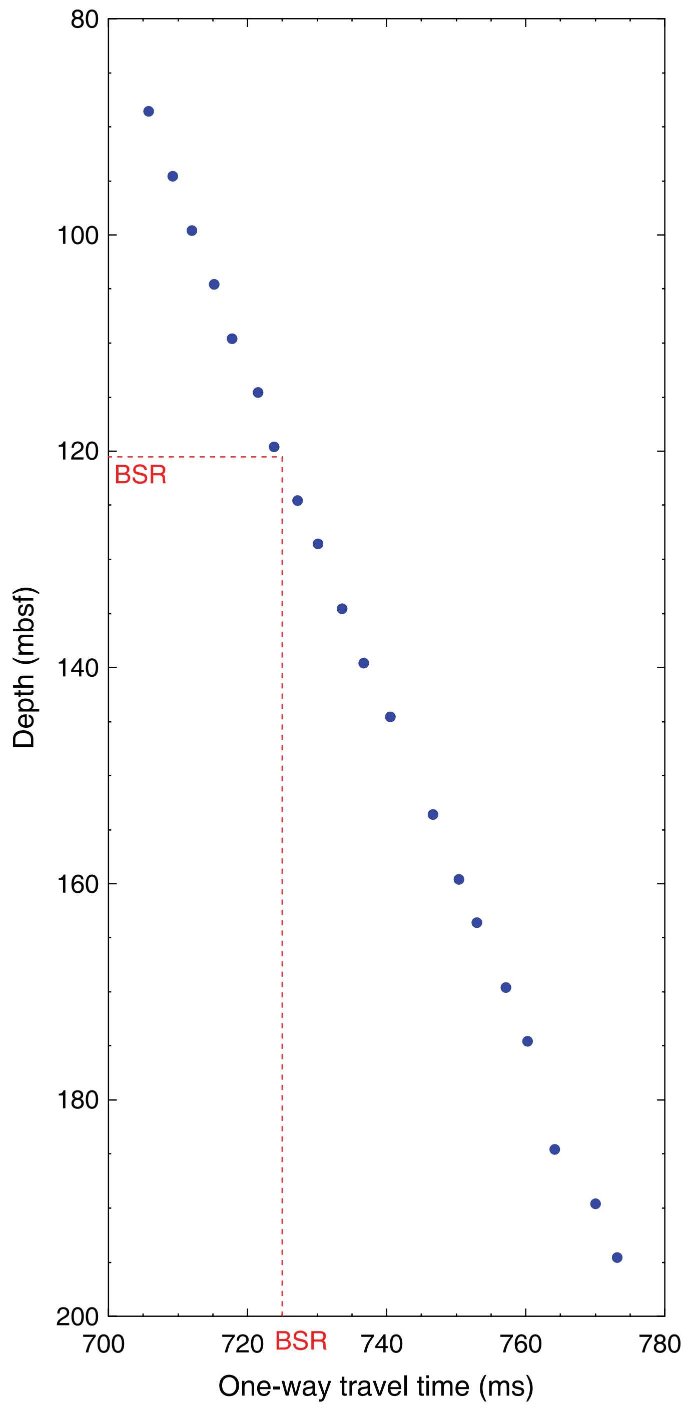

Figure 42. Time-depth plot of first break times in the Hole NGHP-01-05E VSP. [VSP, vertical seismic profile]

low-resistivity water-saturated formation. Using the porosity log and Archie's equation ($R_0 = (a\,R_w) / f^{m}$), we derive the predicted resistivity of the water-saturated formation R_o. A qualitative influence of gas hydrate on the resistivity log is indicated by the difference between the R_0 and the measured resistivity R_t. The actual water saturation, assumed to be the numerical complement of the hydrate saturation, is $S_w = (R_o/R_t)^{1/n}$, with n = 2 (Pearson and others, 1983). We used the density porosity computed from the image-derived density (IDRO) and the resistivity from the

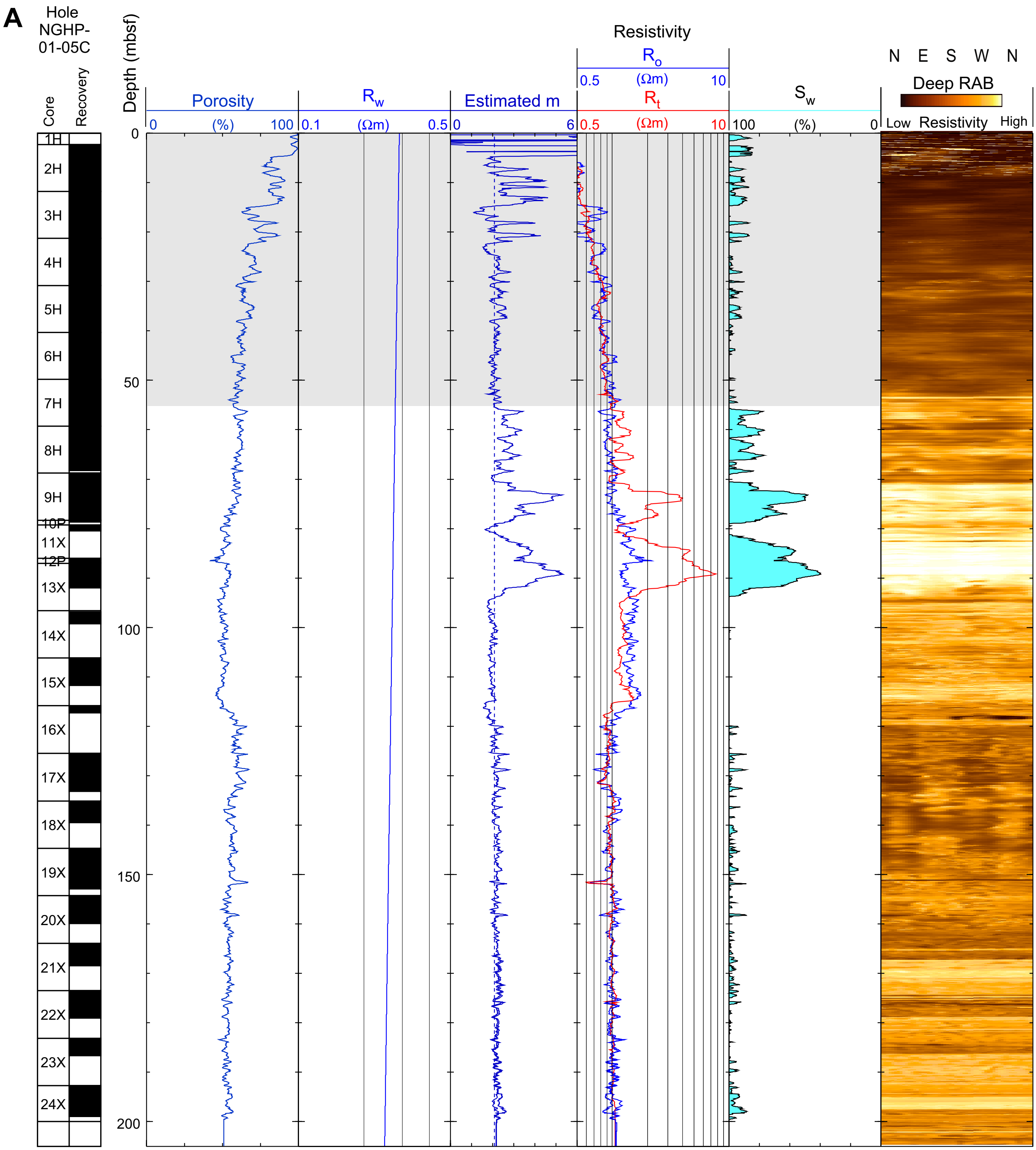

Figure 43. Water saturations from Archie's equation and LWD porosity and resistivity logs in Holes A, NGHP-01-05A and B, NGHP-01-05B. The gray area indicates degraded data quality. [R_w, Formation water resistivity; R_0, Computed formation resistivity for 100 percent water saturation; R_t, Measured resistivity; S_w, water saturation]

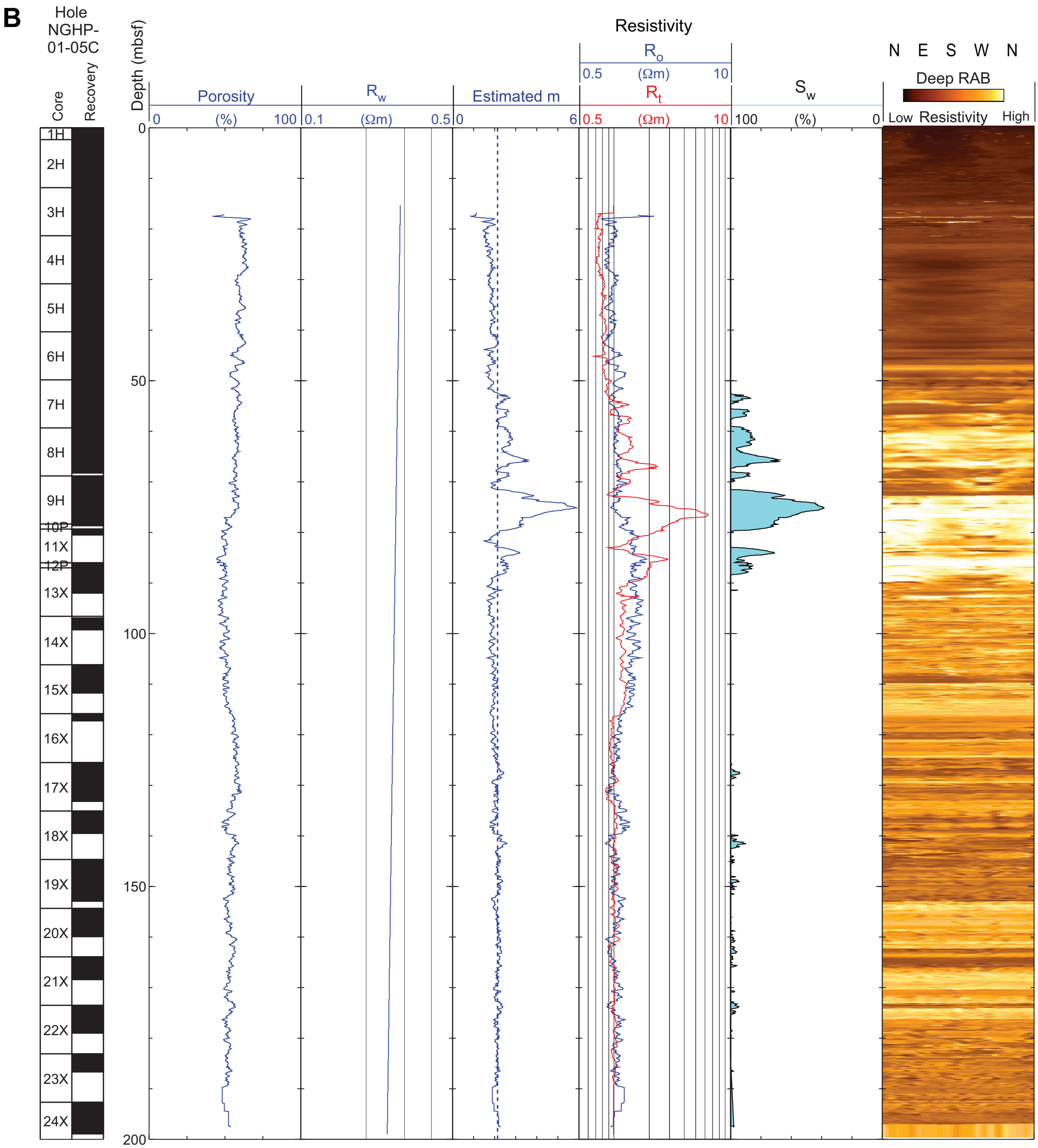

Figure 43. Water saturations from Archie's equation and LWD porosity and resistivity logs in Holes A, NGHP-01-05A and B, NGHP-01-05B. The gray area indicates degraded data quality. [R_w, Formation water resistivity; R_0, Computed formation resistivity for 100 percent water saturation; R_t, Measured resistivity; S_w, water saturation]—Continued

16 in, phase-shift, high-frequency propagation resistivity (P16H) measured by the EcoScope tool. We use the P16H curve because it is the resistivity with the highest vertical resolution measured by the EcoScope.

The strongest evidence for gas hydrate is in the intervals 55–94 mbsf (Hole NGHP-01-05A) and 53–90 mbsf (NGHP-01-05B), where the computed gas-hydrate saturations reach a maximum of about 60 percent (fig. 43). These intervals are where the borehole images show prominent high-resistivity layers. On the other hand, the computed water saturations <100 percent at the top of Hole NGHP-01-05A (0–55 mbsf) are probably due to an underestimation of density in an enlarged borehole.

Although these two holes are only 11 m apart, the details of the resistivity curves and of the computed gas-hydrate saturations are significantly different. For example, the maximum computed gas-hydrate saturation is at 90 mbsf in Hole NGHP-01-05A, whereas in Hole NGHP-01-05B the maximum is found at 77 mbsf. These differences suggest that these gas-hydrate accumulations may have significant lateral heterogeneity. The additional comparison with the wire-line logs recorded in Holes NGHP-01-05D and NGHP-01-05E (fig. 41) confirms this observation. The resistivity logs in Hole NGHP-01-05D display similar high resistivity values over a ~20 m interval between ~75 and ~95 mbsf, almost identical to the data in NGHP-01-05A, but this high-resistivity interval extends to ~120 mbsf in Hole NGHP-01-05D, with significantly higher resistivity values. Since this is the only one of these holes to be cored, one can only speculate that these differences are due to variability in gas-hydrate distribution. The strong similarity between the gamma ray and other logs between these hole rules out any significant lithological variability and supports the interpretation that these differences are likely related to gas-hydrate distribution.

It should be noted that the saturations computed in these holes depend on the curve chosen for the true formation resistivity R_t. As in the analysis done for the other NGHP Expedition 01 holes, we have used for R_t the 2 MHz phase-shift resistivity at 16 in transmitter-receiver spacing (P16H). If the ring resistivity (RES_RING) had been used, however, the computed gas hydrate saturations would have been lower because in Holes NGHP-01-05A and NGHP-01- 05B the ring resistivity is less than P16H in the resistive layers (fig. 37). On the other hand, we could have chosen as R_t the 2 MHz phase-shift resistivity at 40 in (P40H) on the grounds that it should be closer to the formation resistivity because it has a deeper depth of investigation than P16H. In this case, the computed gas-hydrate saturations would have been higher, because in Holes NGHP-01-05A and NGHP-01-05B the deep-reading phase-shift resistivities are always higher than the shallow-reading resistivities (fig. 37).

References Cited

Adolph, B., Archer, M., Codazzi, D., el-Halawani, T., Perciot, P., Weller, G., Evans, M., Grant, J., Griffiths, R., Hartman, D., Sirkin, G., Ichikawa, M., Scott, G., Tribe, I., and White, D., 2005, No more waiting—Formation evaluation while drilling: *Oilfield Review*, Autumn 2005, p. 4–21.

Aldred, W., Cook, J., Bern, P., Carpenter, B., Hutchinson, M., Lovell, J., Rezmer-Cooper, I., and Leder, P.C., 1998, Using downhole annular pressure measurements to improve drilling performance: *Oilfield Review*, Winter 1998, p. 40–55.

Berger, W.H., and Jansen, E., 1994. Mid-Pleistocene climate shift—The Nansen connection, *in* Johannessen, O.M., Muensch, R.D., and Overland, J.E. eds., The role of the polar oceans in shaping the global environment: Geophysical Monograph, American Geophysical Union, v. 85, p. 295–311.

Bjerrum, L., 1972, Embankments on soft ground, *in* ASCE Specialty Conference on Performance of Earth and Earth-Supported Structures, Lafayette, Ind., June 11–14, 1972, Proceedings: New York, American Society of Civil Engineers, v. 2, p. 1–54. [Held at Purdue University]

Collett, T.S., and Ladd, J., 2000, Detection of gas hydrate with downhole logs and assessment of gas hydrate concentrations (saturations) and gas volumes on the Blake Ridge with electrical resistivity log data, *in* Paull, C.K., Matsumoto, R., Wallace, P.J., and Dillon, W.P., eds., Proceedings of the Ocean Drilling Program, Scientific Results, v. 164: College Station, Tex., Ocean Drilling Program, p. 179–191, accessed October 9, 2005 at *http://www.odp.tamu.edu/publications/164_SR/VOLUME/CHAPTERS/SR164_19.PDF*. [CD-ROM; available from: Ocean Drilling Program, Texas A&M University, College Station, Tex. 77845-9547, U.S.A.]

Davis, E.E., Hyndman, R.D., and Villinger, H., 1990, Rates of fluid expulsion across the northern Cascadia accretionary prism—Constraints from new heat flow and multichannel seismic reflection data: Journal of Geophysical Research, v. 95, p. 8869–8889.

Duan, Z., Møller, N., Greenberg, J., and Weare, J.H., 1992, The prediction of methane solubility in natural waters to high ionic strengths from 0° to 250 °C and from 0 to 1600 bar: Geochimica et Cosmochimica Acta, v. 56, p. 1451–1460.

Erickson, S.N., and Jarrard, R.D., 1998, Velocity-porosity relationships for water-saturated siliciclastic sediments: Journal of Geophysical Research, v. 103, p. 30,385–30,406.

Expedition 311 Scientists, 2005, Cascadia margin gas hydrates—Integrated Ocean Drilling Program Preliminary Report, v. 311: College Station, Tex., Ocean Drilling Program, doi:10.2204/iodp.pr.311.2005.

Fofonoff, N.P., 1985, Physical properties of seawater: Journal of Geophysical Research, v. 90, no. C2, p. 3332–3342.

Giosan, L., Flood, R.D., Grützner, J., and Mudie, P., 2002, Paleoceanographic significance of sediment color on western North Atlantic Drifts—I. Origin of color: *Marine Geo*logy, v. 189 p. 25–41.

Holtz, R.D., and Kovacs, W.D., 1981, An introduction to geotechnical engineering: Englewood Cliffs, N.J., Prentice-Hall, Inc., 733 p.

Hunt, R.E., 1984, Geotechnical engineering investigation manual: New York, McGraw-Hill Book Company, 983 p.

Kvenvolden, K.A., and Lorenson, T.D., 2000, Methane and other hydrocarbon gases in sediment from the southeastern North American continental margin, *in* Paull, C.K., Matsumoto, R., Wallace, P.J., Black, N.R., Borowski,W.S.,Collett, T.S., Damuth, J.E., Dickens, G.R., Egeberg, P.K., Goodman,K., Hesse, R.F., Hiroki, Y., Holbrook, W.S., Hoskins, H., Ladd, J. ,Lodolo, E., Lorenson, T.D.,Musgrave, R.J., Naehr, T.H., Okada, H., Pierre, C., Ruppel, C.D., Satoh, M., Thiery, R., Watanabe, Y., Wehner, H., Winters, W.J.,and Wood, W.T., Gas hydrate sampling on the Blake ridge and Carolina rise; covering leg 164 of the cruises of the drilling vessel *JOIDES Resolution*, Halifax, Nova Scotia, to Miami, Florida, sites 991–997, 31 October–19 December 1995: Proceedings of the Ocean Drilling Program, Scientific Results, v. 164, p. 29–36.

Ladd, C.C., Foote, R., Ishihara, K., Schlosser, F., and Poulos, H.G., 1977, Stress-deformation and strength characteristics—State-of-the-art report: Proceedings of the Ninth International Conference on Soil Mechanics and Foundation Engineering, Tokyo, v. 2, p. 421–494.

Lambe, T. W. and Whitman, R.V., 1969, Soil mechanics: New York, John Wiley and Sons, 553 p.

Musgrave, R.J., Bangs, N.L., Larrasoana, J.C., Gracia, E., Hollamby, J., and Vega, M.E., 2006, Rise of the base of the gas hydrate zone since the last glacial recorded by rock magnetism: Geology, v. 34, no. 2, p. 117–120.

Novosel, I., Winters, W.J., Boldina, O.M., Labails, C., and Geli, L., 2007, Thermal conductivity of sediment recovered from the IMAGES VIII/PAGE 127 Gas Hydrate and Paleoclimate Cruise on the *R/V Marion Dufresne* in the Gulf of Mexico, 2–18 July 2002, *in* Winters, W.J., Lorenson, T.D., and Paull, C.K., eds., Initial report of the IMAGES VIII/PAGE 127 gas hydrate and paleoclimate cruise on the RV Marion Dufresne in the Gulf of Mexico, 2–18 July 2002: U.S. Geological Survey Open-File Report 2004–1358.

Pearson, C.F., Halleck, P.M., McGuire, P.L., Hermes, R., and Mathews, M., 1983, Natural gas hydrate deposits—A review of *in situ* properties: Journal of Physical Chemistry, v. 87 p. 4180–4185.

Reeburgh, W.S., 1976, Methane consumption in Cariaco Trench waters and sediments: Earth and Planetary Science Letters., v. 28, p. 337–344.

Sloan, E.D., 1998, Clathrate Hydrates of Natural Gases (2d ed.): New York (Marcel Dekker), 705 p.

Tréhu, A.M., Bohrmann, G., Rack, F.R., Torres, M.E., Delwiche, M.E., Dickens, G.R., Goldberg, D.S., Gracia, E., Guerin, G., Holland, M., Johnson, J.E., Lee, Y.J., Liu, C.S., Long, P.S., Milkov, A.V., Riedel, M., Schultheiss, P., Su, X., Teichert, B., Tomaru, H., Vanneste, M., Watanabe, M., and Weinberger, J.L., 2003, Proceedings of the Ocean Drilling Program, Initial Reports, v. 204: College Station, Tex., Ocean Drilling Program, 81 p. [CD-ROM; available from: Ocean Drilling Program, Texas A&M University, College Station, Tex. 77845-9547, USA.]

Waxman, M.H., and Smits, L.J.M., 1968, Electrical conductivity in oil-bearing shaly sands: Society of Petroleum Engineers Journal, v. 8, no. 2, p. 107–122.

Xu, W., 2002, Phase balance and dynamic equilibrium during formation and dissociation of methane gas hydrate, *in* International Conference on Gas Hydrates, 4th, Yokohama, Japan, May 2002, Proceedings: Yokohama, Japan, International Conference on Gas Hydrates, p. 195–200.

Xu, W., 2004, Modeling dynamic marine gas hydrate systems: American Mineralogist, v. 89, p. 1271–1279.